Experimental study of the boundary layer separation and transition processes under turbine-like conditions by means of advanced post-processing techniques

Matteo Dellacasagrande

Supervisor: Prof. Daniele Simoni
Ing. Davide Lengani

Department of Mechanical Engineering, Energy, Management and Transports
University of Genova

This dissertation is submitted for the degree of
Doctor of Philosophy

Faculty of Mechanical Engineering April 2019

Declaration

I hereby declare that except where specific reference is made to the work of others, the contents of this dissertation are original and have not been submitted in whole or in part for consideration for any other degree or qualification in this, or any other university. This dissertation is my own work and contains nothing which is the outcome of work done in collaboration with others, except as specified in the text and Acknowledgements.

Matteo Dellacasagrande
April 2019

Abstract

In this work the transition process of the boundary layer (BL) evolving under turbine-like conditions has been experimentally investigated in details. The effects of the Reynolds number (Re), the free-stream turbulence intensity (Tu) and the adverse pressure gradient (APG) imposed to the flow have been studied for a large variation of these parameters, since they are known to strongly influence the separation and transition processes of the boundary layer. Emphasis has been put on both the statistical and the dynamic behaviour of the flows at hand, that have been experimentally characterized by means of advanced and ad-hoc developed post processing techniques.

The study of the effects of the Reynolds number and the Tu level on the development of laminar separation bubbles (LSB) under fixed APG is presented in the first part of this work. The mechanisms by which the variations of Re and Tu act on the bubble size were found to be substantially different and the coexistence of different amplification mechanisms has been observed in the LSBs for high Tu levels.

In case of by-pass transition, the effects of the APG has been investigated with respect to the zero pressure gradient condition. The transition process has been found to be more rapid due to the APG imposed to the flow with respect to the zero pressure gradient case. The profiles of the mean streamwise velocity and velocity fluctuation rms obtained by means of Hot-Wire instrumentation showed a self-similar behavior in the laminar part of the boundary layer. For what concern the effects of the Tu level on the velocity and rms of velocity fluctuation profiles, the high free-stream turbulence has been found to reduce the effects of the pressure gradient on the curvature of the mean velocity profiles and shifting the maximum of the turbulence peak towards the wall.

In order to shed light on the effects of the APG variation on the statistical and dynamic behaviour of LSB, as well as to provide a complete experimental database containing information about the effects of Re, Tu and APG in case of both attached and separated flows, a new test section has been designed in the second part of this work allowing the continuous variation of the pressure gradient imposed to the flow. In case of separated flows, the separation position was found to move downstream when the APG is reduced and the bubble becomes longer. However, the bubble thickness is reduced with respect to the higher

APGs conditions.

Proper Orthogonal Decomposition (POD) has been adopted to reduce the large amount of experimental data collected, obtaining a statistical treatment of the main dynamics at hand in terms of their energy content. Moreover, with the aim of characterizing the coexistence of structures with different energy within the flow (e.g., boundary layer streaks, Kelvin-Helmholtz and free-stream vortices) a variant of the classical POD procedure has been proposed. The application of this technique in case of both attached and separated flows highlighted the presence of free-stream structures near the edge of the boundary layer where the transition process has been found to occur, suggesting that free-stream structures can actually play a crucial role in the evolution and breakdown of structures growing into the boundary layer, thus leading transition.

Finally, the analysis of the statistical quantities of the flows at hand (i.e. BL integral parameters) has been carried out for all the acquired conditions with the aim of developing new empirical correlations for the prediction of the transition onset and length in case of separated flows. Data collected during both the measuring campaigns allowed the tuning of the proper coefficients in order to take into account for the variation of all the parameters considered in this work. The proposed correlations have been found to fit both the collected data as well as other experimental data available in literature.

Table of contents

List of figures

List of tables

Nomenclature

Roman Symbols

C_f	Skin friction coefficient
H_{12}	Shape factor
K	Acceleration parameter
U	Mean streamwise velocity
u	Instantaneous streamwise velocity
V	Mean normal to the wall velocity
v	Instantaneous normal to the wall velocity
x	Streanmwise coordinate
y	Normal to the wall coordinate

Greek Symbols

α	Opening angle of the adjustable endwalls of the test section
β	Grid geometry parameter
δ	Boundary layer thickness
δ^x	Displacement thickness
γ	Intermittency function
λ_θ	Momentum thickness acceleration parameter
μ	Dynamic viscosity

ν	Kinematic viscosity
σ	Emmons dimensionless spot production
τ_w	Wall shear stress
θ	Momentum thickness

Superscripts

’	Fluctuating component

Subscripts

0	Quantity referred to the inlet of the test section
∞	Free-stream quantity
e	Quantity referred to the edge of the boundary layer
s	Quantity referred to the separation position position
t	Quantity referred to the transition onset position
$turb$	Turbulent quantity

Acronyms / Abbreviations

K-H	Kelvin-Helmholtz
Re_θ	Momentum thickness Reynolds number
Re_x	Reynolds number based on the streamwise coordinate
APG	Adverse Pressure Gradient
BL	Boundary layer
LSB	Laminar Separation Bubble
LDV	Laser Doppler Velocimetry
N-S	Navier-Stokes
PIV	Particla Image Velocimetry
Re	Reynolds number

rms	Root Mean Square
TR	Time Resolved
Tu	Turbulence intensity

Chapter 1

Introduction

The boundary layer concept has been proposed by Ludwig Prandtl in 1904 during the Third International Mathematics Congress in Heidelberg, Germany. Prandtl's presentation was only 10 minutes long and the related paper short, but the concepts he described constitute, to this day, the basic of the modern world of aerodynamics and fluid dynamics [5].

Before Prandtl, other mathematicians and physicists gave significant contributions to the development of modern aerodynamics and fluid mechanics, as Daniel Bernoulli (1700-1782), Rond d'Alembert (1717-1783) and Leonhard Euler (1707-1783). Euler developed the mathematical description of a fluid flow in term of infinitesimally small elements and, applying the mass conservation and the Newton's second law he derived the equations governing the so called *inviscid problem*. More precisely, he derived a couple of non linear partial differential equations (PDE) without taking into account for the effects due to the viscosity of the flows. It was only in the first half of the 19^{th} century that Claude-Louis Navier and George Stokes derived independently the well known Navier-Stockes (N-S) equations, that are a system of coupled non linear PDE accounting for the friction effects within the flows. Nowadays, a general solution of these equations does not exist. The impossibility of solving the N-S equations prevented the engineers of the early 20^{th} century from correctly predict the shear stress on a solid body immersed in a fluid flow. The force acting on an airfoil is indeed known to be the result of both pressure and shear stress distributions. Even though the pressure distribution on an airfoil can be computed referring to the inviscid theory, the shear stress are instead the result of the viscous forces, thus in this case the N-S equations have to be considered. In this context, the boundary layer theory introduced by Prandtl allows a strong simplification of the N-S equations, which inside the boundary layer become a system of parabolic PDE, which can be analytically solved in some basic flow configurations (e.g., Blasius's solution for flat plate) [5].

According to the BL concept proposed in 1904 by Prandtl, viscous effects are confined in a thin flow region near the walls of a solid body, while far from the wall, the equations governing the evolution of potential flows are valid. Here is reported the description of the BL concept as described by Prandtl [93]:

> *"A very satisfactory explanation of the physical process in the boundary layer between a fluid and solid body could be obtained by the hypothesis of an adhesion of the fluid to the walls, that is, by the hypothesis of a zero relative velocity between fluid and wall. If the viscosity was very small and the fluid path along the wall not too long, the fluid velocity ought to resume its normal value at a very short distance from the wall. In the thin transition layer however, the sharp changes of velocity, even with small coefficient of friction, produce marked results"*

Inside the BL velocity gradients are observed in the normal to the wall direction (see figure 1.1). Since the shear stress are originated from the occurrence of velocity gradients, then the BL is the place where the dominant shear stress occur. One of the most important topic related to the BL concept is the characterization of the BL transition, i.e. the transition of the viscous layer from the ordered laminar state to the turbulent one. Figure 1.1 shows that a higher growth rate of the BL thickness, as well as higher velocity gradients at the wall, occurs as a consequence of the transition process. The transition to the turbulent state results in higher shear stress and losses [98]. Depending on the external conditions (pressure gradients imposed to the flow, free-stream turbulence and local Reynolds number among others), the laminar to turbulent transition can occur in three different main ways: the *natural transition*, the *bypass transition* and the *separated flow transition*.

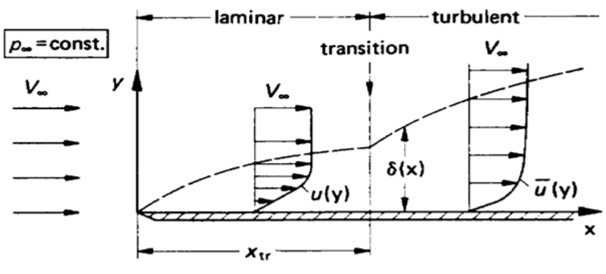

Fig. 1.1 Boundary layer development on a flat plate.

In the *natural transition* case the transition process is driven by exponentially growing eigensolutions to the linearized disturbance equations, referred to as Tollmien–Schlichting (T-S) waves (see Fig. 1.2), whose breakup is responsible for the generation of turbulent spots, thus transition. This kind of transition normally occurs with very low turbulence

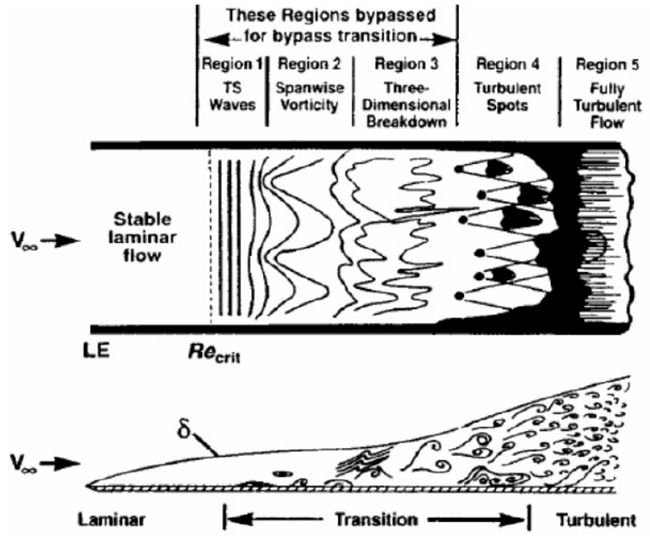

Fig. 1.2 Mechanisms involved in the natural transition and bypass transition processes.

intensity levels ($< 0.5\%$) such as those characterizing the free-stream around a wing of an airplane during cruise. When the turbulence intensity level is sufficiently high, the Tollmien–Schlichting waves are *by-passed* and the (by-pass) transition process is driven by streamwise elongated structures called *streaks*, which constitute low frequency disturbances of the streamwise velocity component (see e.g. Morkovin [85], Matsubara et al [78], Zaki [132]). BL streaks constitute an optimal perturbation to the linear N-S operator that, due to non orthogonality, admits *transient growth* of disturbances (the initial growth is then followed by a viscous decay). If the initial amplitude of the perturbation is sufficiently high, transition can occur at a Reynolds number lower than the critical one predicted by the modal theory and the modal response of the T-S waves is by-passed. Several studies carried out in the past (see e.g. Klebanoff [49], Roach et al. [94] and Westin et al. [126]) showed that the occurrence of high- and low-speed streaks, which act distorting the BL, and the subsequent instability of particular streaks induce the formation of turbulent spots, thus transition [132] (see figure 1.3). In this context, free-stream turbulence may interact with BL streaks promoting their instability (see e.g. Jacob and Durbin [46]).

If strong adverse pressure gradients are imposed to the flow, the BL can separate from the wall before the transition onset, even under elevated Tu levels. In this context, the fluid inside the boundary layer, which lost its kinetic energy due to the viscous effects, turns around giving origin to a laminar separated flow, as described by Prandtl [93]:

In given cases in certain points fully determined by external conditions, the fluid flow ought to separate from the wall. That is, there ought to be a layer fluid which, having been set in rotation by the friction on the wall, insinuates itself into the free fluid [..] On an increase

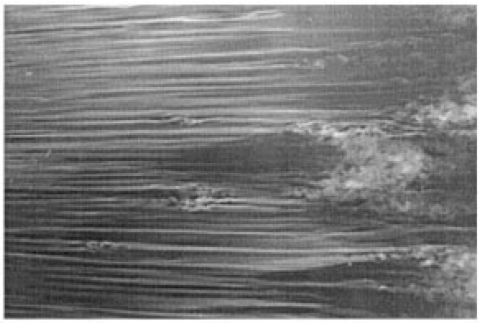

Fig. 1.3 Flow visualization of streaky structures in boundary layers affected by free-stream turbulence [78].

of pressure, while the free fluid transforms part of its kinetic energy into potential energy, the transition layers instead, having lost a part of their kinetic energy (due to friction), have no longer a sufficient quantity to enable them to enter a field of higher pressure, and therefore turn aside from it [5]

When a laminar separation occurs, the boundary layer moves far from the wall toward portion of the fluid flow characterized by higher momentum, as shown in figure 1.4. After the separation a region of dead air occur, i.e. of low pressure, inducing a pressure drag whose strength depends on the size of the separation bubble. As specified by Prandtl, the free fluid normally produces the external conditions affecting the BL development, while the viscous effects are confined in a thin layer close to the walls, whose effects are negligible out of it. However, in case of huge separations the viscous layer can sensibly alter the surrounding potential flow (i.e. viscid-inviscid interaction) due to its detachment from the walls. The occurrence of a BL separation also induces high losses due to the generation of vortices which are responsible for high shear stress. Indeed, in case of separated flows the velocity fluctuations are amplified in the separated shear layer due to the inviscid Kelvin–Helmholtz (K-H) instability process which drives transition (see Pauley et al. [91], Sarkar [96] and Lardeau et al. [56]). The velocity fluctuations amplified in the separated BL grow up until saturation occurs inducing the roll-up of the BL and the consequent formation of large scale vortices (K-H vortices), whose breakup drives the transition to the turbulent state (see e.g. Alam and Sandham [4] and Yang and Voke [128]).

Since Prandtl introduced the BL concept in the 1904, several researchers started to extend the BL theory providing solutions to the BL equations for different flow configurations. In 1908, Heinrich Blasius published his results about the development of the boundary layer over a flat plate and a circular cylinder [10]. Successively, Theodore Von Karman derived a momentum integral equation for the boundary layer (the so called *Von Karman's equation*),

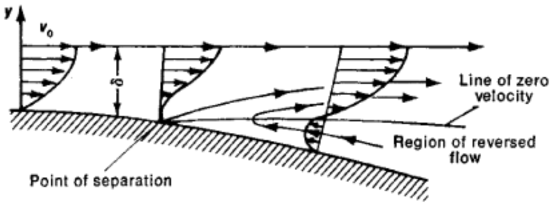

Fig. 1.4 Boundary layer separation.

which is still applied today to a large number of engineering problems [122]. Among all, the most comprehensive work concerning the BL concept and its transition is maybe the Schlichting's *Boundary-Layer Theory* [98], who was a Prandtl's student.

Although analytical solutions of the BL equations can be provided for simple flow conditions, almost all today's engineering problems concern complex geometries and flow configurations that require reliable models for the correct prediction of viscous losses. To this end, many experiments were carried out in the past after the introduction of the BL concept, providing the basis for the successive development of numerical models which are nowadays widely used in the design process of modern aeronautical components. After a brief description of the motivation of this work, the physics of the boundary layer will be discussed in details in the following chapter presenting the different mechanisms leading to transition.

1.1 Motivation

In 2017, more than 4.1 billion passengers were transported by commercial aircrafts around the world, resulting in up to 27000 flights per day only in Europe. The forecasts nearly double the transported passengers up to 7.8 billion aircraft passengers for the year 2036. This extensive amount of current and upcoming flights significantly affects the global environment in terms of air pollution, noise emission and consumption of natural resources. One of the key element of the design of modern aero-engines characterized by lower fuel consumption and polluting emissions is the weight reduction of each component constituting the whole propeller. This is normally achieved by reducing the length of the intermediate turbine diffuser, moving toward aggressive and super aggressive geometries (see e.g., Göttlich [37]), or by reducing the number of blades of the low pressure turbine (LPT), which is at least one of the most heavy components of the engine. For what concerns the intermediate turbine diffuser, aggressive geometries can be characterized by huge separations which alter the flow field at the inlet of the first stage of the LPT. The experimental and numerical studies carried out in the past on such components allowed the design of control system aimed at reducing or even suppressing the BL separations occurring in the aggressive and super aggressive turbine diffusers (see e.g. Lengani et al [63]).

On the LPT side, the reduction of the number of blades results in a higher aerodynamic loading seen by each blade (high-lift profiles), thus the risk of stall is increased. Several experimental analysis revealed that the viscous losses generated on turbine blade surfaces have a critical impact on the efficiency of the whole component. Curtis et al. [23], for example, showed that the losses due to the boundary layer development on the suction side of the turbine blades constitute one of the most relevant source of the overall losses for the whole engine. The correct prediction of the evolution of the boundary layer separation and transition phenomena therefore plays a crucial role in the design of new high-lift high-efficiency profiles. The best known work concerning with the effects of boundary layer separation and transition processes in turbomachinery components is probably *The Role of Laminar-Turbulent Transition in Gas Turbine Engines* written by Mayle in 1991 [80], where empirical correlations for the prediction of the transition process are proposed (see also Hatman and Wang [43] and Gostelow [36] for instance). Even tough the correlations proposed by Gostelow [36] and Mayle [80] were introduced for attached boundary layers, they are frequently adopted in case of separated flows, where the transition is driven by completely different mechanisms, as better highlighted in the following chapters. The need for reliable correlations to be implemented in the modern CFD solvers for industrial applications has led researchers to do several works in the past trying to understand and model the BL transition and the loss production mechanisms observable in turbine blade rows under different flow conditions (see e.g., Butler et al. [19], Sjolander et al. [70], Volino [120, 121] and Michalek [82]).

The present work focuses on the experimental analysis of the development of the boundary layer transition under conditions relevant for the design of blade profiles installed in the low pressure turbines of modern aero-engines. The characterization of the transition mechanisms in case of both separated and attached flows could allow the development of the technologies aimed at the control of these phenomena as well as the introduction of new empirical correlations able to predict the evolution of the transition process under different flow conditions.

Chapter 2

Physics of boundary layer transition

In the following sections, the theoretical and mathematical background of the boundary layer concept will be presented for a better understanding of the results discussed in this work. An overview of the main literature works describing the effects of Tu, Re and the APG imposed to the flow on the boundary layer transition and separation processes is also reported.

2.1 Boundary layer concept

The boundary layer concept allows keeping into account the viscous effects in the motion of fluid flows, that is the property of fluids of transmitting shear stresses between portions of the flow that have different velocities [98]. The velocity gradients occurring in flows over a solid surface are responsible for the generation of wall shear stresses that are defined as:

$$\tau_w = \mu \left(\frac{du}{dy} \right)_{y=0} \tag{2.1}$$

Where μ is the dynamic viscosity, and the normal to the wall derivative of the streamwise velocity component (u) is computed at the wall ($y = 0$). It can be seen that higher gradients or viscosity produce greater stresses. Close to the surface the viscous effects dominate, varying the velocity of the flow particles from zero at the wall (due to electrostatic forces causing the no-slip condition) to the free stream value, while out of the BL edge the effects of viscosity are negligible. The effect of friction is to transmit shear stresses, increasing the velocity of the fluid particles close to the wall and slowing the fluid in the faster region far from the wall. The portion of fluid that includes the 99% of velocity variation compared to the free-stream velocity, defined as *boundary layer thickness* $\delta_{99}(x)$, is monotonically increasing.

In order to better highlight the effects of transition on the BL growth and viscous stresses, the simplified Blasius solution valid for flat plate under zero prssure gradient is briefly reported here. In case of 2D flows evolving on a flat plate, Blasius [6] obtained the self-similar solution shown in figure 2.1. where η and $f'(\eta)$ are similarity functions [6]. In this simplified condition, the values of δ_{99} and the skin friction coefficient C_f can be exactly predicted as a function of the distance x from the leading edge of the plate. C_f, defined as the ratio between the shear stress at the wall τ_w and the dynamic load $1/2\rho_\infty U_\infty^2$ has been found to depend on the local Reynolds number in the form:

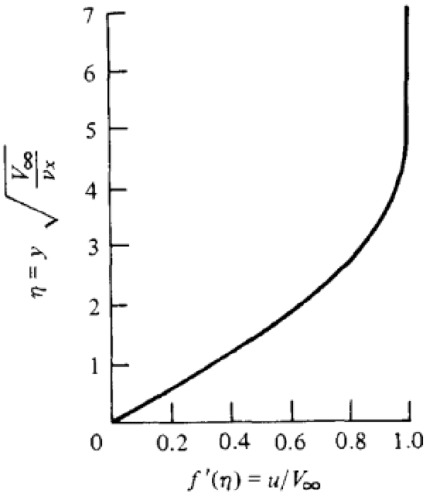

Fig. 2.1 The Blasius self similar velocity profile in a laminar boundary layer developing on a flat plate with zero incidence.

$$C_{f_{lam}} = \frac{0.664}{\sqrt{Re_x}} \tag{2.2}$$

That is, C_f decreases with the square root of the distance from the leading edge of the plate. According to the Blasius solution, the laminar BL thickness is instead defined as:

$$\delta_{lam} = \frac{5.0x}{\sqrt{Re_x}} \tag{2.3}$$

i.e. the laminar boundary layer thickness over a flat plate grows as $x^{\frac{1}{2}}$. Note that the previous solutions are valid only for laminar boundary layers. Moving downstream along the plate, the local Reynolds number becomes sufficiently high to induce transition, thus a turbulent boundary layer occurs. In this context, the Blasius solution decays while other empirical correlations are referred to for the prediction of δ_{99} and C_f in the case of fully developed turbulent boundary layer:

$$\delta_{turb} = \frac{0.37x}{Re_x^{\frac{1}{5}}} \tag{2.4}$$

$$C_{f_{turb}} = \frac{0.074}{Re_x^{\frac{1}{5}}} \tag{2.5}$$

The turbulent boundary layer thickness varies as $x^{\frac{4}{5}}$, growing faster than the laminar one. The faster growth of the turbulent BL is due to a higher mixing effect between adjacent portions of fluid. The friction coefficient is instead proportional to $Re^{-\frac{1}{7}}$ (Prandtl's law), yielding larger friction drag coefficient.

The lack of an exact similarity solution for the turbulent BL is due to the occurrence of a viscous sub-layer near the wall where the viscous effects dominate. More precisely, three different regions with different growth and velocity distribution can be identified in a turbulent boundary layer: the *viscous sub-layer*, the *buffer layer* and the *logarithmic layer*, as shown in the scheme reported in figure 2.2. These three regions are defined as a function of the wall distance expressed in terms of the dimensionless coordinate $y^+ = \frac{y}{\nu}\sqrt{\frac{\tau_w}{\rho}}$. The velocity corresponding to each of these three regions is instead express in terms of the dimensionless velocity $u^+ = u\sqrt{\frac{\rho}{\tau_w}}$, where $\sqrt{\frac{\tau_w}{\rho}}$ is the so called friction velocity u_τ, that is $u^+ = u/u_\tau$. In the viscous sub-layer ($y^+ < 5$) u^+ is directly proportional to y^+. In this region the flow is laminar due to the high influence of viscosity near the wall. For $y^+ > 30$ there is the so called logarithmic zone, in which the flow can be considered turbulent and subjected to strong velocity fluctuations in both intensity and direction. In this region, the *logarithmic low* is valid and u^+ is proportional to the logarithm of y^+, that is $u^+ = \frac{1}{k}ln(y^+) + C^+$, where k and C^+ are the von Kármán constants. The zone between the viscous and the logarithmic layers, called buffer zone, has gradually changing properties from the viscous to the logarithmic regions and neither low holds.

2.2 Differential equations of the boundary layer

To derive the differential equations of the boundary layer the starting point is given by the continuity equation and the Navier-Stokes equations, which for a three-dimensional incompressible viscous flow result in the following system of partial differential equations:

$$\frac{\partial u}{\partial t} + u\frac{\partial u}{\partial x} + v\frac{\partial u}{\partial y} + w\frac{\partial u}{\partial z} = -\frac{1}{\rho}\frac{\partial P}{\partial x} + \nu\left(\frac{\partial^2 u}{\partial x^2} + \frac{\partial^2 u}{\partial y^2} + \frac{\partial^2 u}{\partial z^2}\right) \tag{2.6}$$

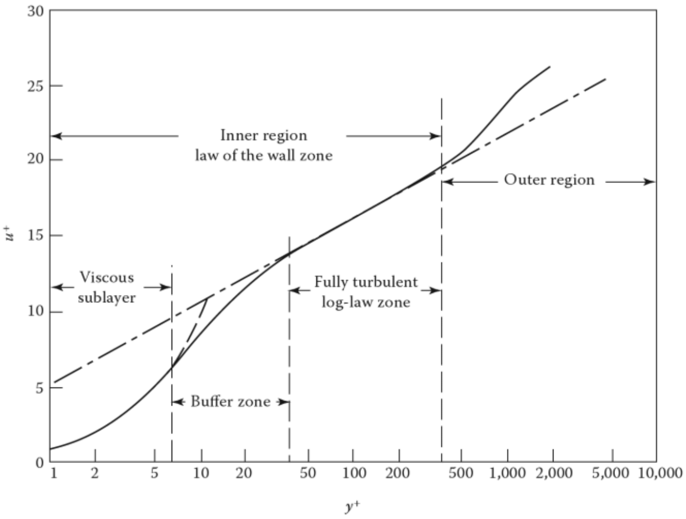

Fig. 2.2 Viscous sublayer ($y^+ < 5$), Buffer layer ($5 < y^+ < 30$) and Fully turbulent or Log-low region ($y^+ > 30$).

$$\frac{\partial v}{\partial t}+u\frac{\partial v}{\partial x}+v\frac{\partial v}{\partial y}+w\frac{\partial v}{\partial z}=-\frac{1}{\rho}\frac{\partial P}{\partial y}+\nu\left(\frac{\partial^2 v}{\partial x^2}+\frac{\partial^2 v}{\partial y^2}+\frac{\partial^2 v}{\partial z^2}\right) \tag{2.7}$$

$$\frac{\partial w}{\partial t}+u\frac{\partial w}{\partial x}+v\frac{\partial w}{\partial y}+w\frac{\partial w}{\partial z}=-\frac{1}{\rho}\frac{\partial P}{\partial z}+\nu\left(\frac{\partial^2 w}{\partial x^2}+\frac{\partial^2 w}{\partial y^2}+\frac{\partial^2 w}{\partial z^2}\right) \tag{2.8}$$

$$\frac{\partial u}{\partial x}+\frac{\partial v}{\partial y}+\frac{\partial w}{\partial z}=0 \tag{2.9}$$

Which further reduces to the following system in case of two dimensional stationary flows:

$$u\frac{\partial u}{\partial x}+v\frac{\partial u}{\partial y}=-\frac{1}{\rho}\frac{\partial P}{\partial x}+\frac{1}{\rho}\frac{\partial}{\partial x}\left(\mu\frac{\partial u}{\partial x}\right)+\frac{1}{\rho}\frac{\partial}{\partial y}\left(\mu\frac{\partial u}{\partial y}\right) \tag{2.10}$$

$$u\frac{\partial v}{\partial x}+v\frac{\partial v}{\partial y}=-\frac{1}{\rho}\frac{\partial P}{\partial y}+\frac{1}{\rho}\frac{\partial}{\partial x}\left(\mu\frac{\partial v}{\partial x}\right)+\frac{1}{\rho}\frac{\partial}{\partial y}\left(\mu\frac{\partial v}{\partial y}\right) \tag{2.11}$$

$$\frac{\partial u}{\partial x}+\frac{\partial v}{\partial y}=0 \tag{2.12}$$

The system above can be further manipulated by introducing some simplifications based on considerations about the orders of magnitude of each elements of the set of equations, as first suggested by Prandtl in his boundary layer theory. More precisely, since inside the BL the normal to the wall derivatives are significantly higher than the streamwise ones as well as

$v << u$ in the BL, the system of equations above can be further simplified obtaining:

$$u\frac{\partial u}{\partial x}+v\frac{\partial u}{\partial y}=-\frac{1}{\rho}\frac{\partial P}{\partial x}+\frac{1}{\rho}\frac{\partial}{\partial y}\left(\mu\frac{\partial u}{\partial y}\right) \tag{2.13}$$

$$\frac{\partial P}{\partial y}=0 \tag{2.14}$$

$$\frac{\partial u}{\partial x}+\frac{\partial v}{\partial y}=0 \tag{2.15}$$

From equation 2.14 it is evident that within the boundary layer pressure does not change in the wall normal direction, that is, the pressure in the BL can be assigned by means of the inviscid theory.

When dealing with turbulent boundary layers, the equations keep a formulation that is similar to the laminar case, with the main difference due to the addition of new terms describing the effects of turbulence in the momentum equations. To derive the equations in case of turbulent flows, the velocity components and pressure appearing in the N-S equations have to be expressed as the sum of a mean value over time and a fluctuating component, according to the well known Reynolds decomposition:

$$u(t)=\overline{\mathrm{u}}+u'(t) \tag{2.16}$$

$$p(t)=\overline{\mathrm{p}}+p'(t) \tag{2.17}$$

Where $\overline{\mathrm{u}}$ is the mean value, constant over time and defined as:

$$\overline{\mathrm{u}}=\lim_{t\to\infty}\frac{1}{t}\int_0^t u(\tau)d\tau \tag{2.18}$$

Substituting the definition of $u(t)$ and $p(t)$ given by equations 2.16 and 2.17 in the two-dimensional Navier-Stokes equations and averaging the whole set of equations the Reynolds Averaged Navier-Stokes (RANS) equations for turbulent flows can be obtained:

$$\overline{\mathrm{u}}\frac{\partial\overline{\mathrm{u}}}{\partial x}+\overline{\mathrm{v}}\frac{\partial\overline{\mathrm{u}}}{\partial y}=-\frac{1}{\rho}\frac{\partial\overline{\mathrm{P}}}{\partial x}+\frac{1}{\rho}\frac{\partial}{\partial x}\left(\mu\frac{\partial\overline{\mathrm{u}}}{\partial x}-\rho\overline{\mathrm{u}'^2}\right)+\frac{1}{\rho}\frac{\partial}{\partial y}\left(\mu\frac{\partial\overline{\mathrm{u}}}{\partial y}-\rho\overline{\mathrm{u}'\mathrm{v}'}\right) \tag{2.19}$$

$$\overline{\mathrm{u}}\frac{\partial\overline{\mathrm{v}}}{\partial x}+\overline{\mathrm{v}}\frac{\partial\overline{\mathrm{v}}}{\partial y}=-\frac{1}{\rho}\frac{\partial\overline{\mathrm{P}}}{\partial y}+\frac{1}{\rho}\frac{\partial}{\partial x}\left(\mu\frac{\partial\overline{\mathrm{v}}}{\partial x}-\rho\overline{\mathrm{u}'\mathrm{v}'}\right)+\frac{1}{\rho}\frac{\partial}{\partial y}\left(\mu\frac{\partial\overline{\mathrm{v}}}{\partial y}-\rho\overline{\mathrm{v}'^2}\right) \tag{2.20}$$

$$\frac{\partial \overline{\mathrm{u}}}{\partial x}+\frac{\partial \overline{\mathrm{v}}}{\partial y}=0 \tag{2.21}$$

where the new terms $\overline{\mathrm{u}'\mathrm{v}'}$, $\overline{\mathrm{v}'^2}$ and $\overline{\mathrm{u}'^2}$ are respectively the tangential and normal components of the Reynolds stress tensor, that are responsible for the time averaged stresses induced in the fluid by turbulent fluctuations. Applying now the same considerations on the orders of magnitude applied in the laminar case valid inside the BL, the system of RANS equations can be simplified, obtaining the equations for the turbulent boundary layer:

$$\overline{\mathrm{u}}\frac{\partial \overline{\mathrm{u}}}{\partial x}+\overline{\mathrm{v}}\frac{\partial \overline{\mathrm{u}}}{\partial y}=-\frac{1}{\rho}\frac{\partial \overline{\mathrm{P}}}{\partial x}+\frac{1}{\rho}\frac{\partial}{\partial y}\left(\mu\frac{\partial \overline{\mathrm{u}}}{\partial y}-\rho\overline{\mathrm{u}'\mathrm{v}'}\right) \tag{2.22}$$

$$\frac{1}{\rho}\frac{\partial \overline{\mathrm{P}}}{\partial y}\approx 0 \tag{2.23}$$

$$\frac{\partial \overline{\mathrm{u}}}{\partial x}+\frac{\partial \overline{\mathrm{v}}}{\partial y}=0 \tag{2.24}$$

Similarly to the laminar boundary layer, the turbulent one shows a negligible pressure gradient in the normal to wall direction. The set of equations shows the presence of the additional term $-\rho\overline{u'v'}$ that in case of two-dimensional flows is the tangential term of the Reynolds stress tensor.

2.3 Boundary layer integral parameters

In the analysis of transitional boundary layers, it is useful to introduce some integral definitions, which refer to the entire section of the boundary layer, being only a function of the streamwise coordinate. These integral parameters provide information about the global behaviour of the boundary layer in case of both attached and separated flows. The definition of the main BL integral parameters are reported here since they are used for the development of empirical correlations for the prediction of BL transition and they will be referred to in the next sections where the experimental results will be presented.

The first fundamental BL integral parameter is the *displacement thickness* of the boundary layer δ^*, which is associated with the loss of mass flow due to the viscosity of the flow and it is defined as follows:

$$\delta^*=\int_0^{\delta}\left(1-\frac{u(y)}{U_e}\right)dy \tag{2.25}$$

where U_e is the free-stream velocity at the edge of the BL. According to equation 2.25, the displacement thickness represents the increase in body thickness necessary to generate a non-viscous dummy flow that has the same flow rate as the actual viscous flow. The distribution of the displacement thickness provides information about the growth of the boundary layer and in case of separated flows, the position of the maximum peak in the distribution of δ^* is associated to the bubble maximum displacement position [106].

Another quantity necessary for the integral analysis of the boundary layer is the *momentum thickness* θ, which is defined as:

$$\theta = \int_0^\delta \frac{u(y)}{U_e}\left(1 - \frac{u(y)}{U_e}\right) dy \tag{2.26}$$

The momentum thickness gives an estimation of the loss of momentum directly related to the losses induced by the occurrence of the boundary layer. It can be shown that in case of 2D flow evolving on flat plate, θ evaluated at a given station $x = x_1$ is proportional to the integrated friction drag coefficient from the leading edge $x = 0$ to the position considered according to

$$\theta_{x_1} \propto \frac{1}{x_1}\int_0^{x_1} c_f dx = C_f \tag{2.27}$$

Here c_f is the local skin friction coefficient and C_f here is the mean friction drag coefficient for the length of the surface spanned between $x = 0$ and $x = x_1$.

In addition to the dimensional quantities described above, a third dimensionless parameter called *shape factor* H_{12} is introduced. It is defined as the ratio between the displacement thickness and the momentum thickness:

$$H_{12} = \frac{\delta^*}{\theta} \tag{2.28}$$

The value of H_{12} is useful to determine when the flow is laminar or turbulent, since this parameter assumes precise values in the two cases. For an incompressible flow over a flat plate subjected to zero pressure gradients the following identities hold:

- H_{12}=2.554 for laminar boundary layer (Blasius solution)
- H_{12}=1.43 for turbulent boundary layer (empirical evidence)

When a BL separation occurs due to the an adverse pressure gradient imposed to the flow, H_{12} rises above 3 and then reduces if transition occurs. Further considerations on the integral parameters can be made referring to the well known *Von Karman* integral equation, which provide the evolution of θ in case of steady, two-dimensional and incompressible flow:

$$\frac{d\theta}{dx} + \frac{\theta}{U_e}\frac{dU_e}{dx}\left[2 + H_{12}\right] = \frac{C_f}{2} \tag{2.29}$$

Equation 2.29 clearly highlights the dependence of the momentum thickness growth rate on the streamwise velocity derivative, i.e. pressure gradients. Moreover, the velocity derivative is weighted by the shape factor H_{12} which is representative of the local condition of the BL.

2.4 Boundary layer stability and receptivity

The stability analysis of the boundary layer is aimed at the characterization of the amplification processes of small perturbations that can grow up until the ordered motion typical of laminar flows breaks into turbulence. The starting point for the BL stability analysis are the N-S equations reported in the system of equations (2.6)-(2.8). Considering the Reynolds decomposition of the velocity and pressure fields (see equation 2.16), the equations for the spatial-temporal evolution of turbulent flows can be derived. With the hypothesis of 2D mean parallel flow (i.e. $\overline{u} = \overline{u}(y)$) and considering initial infinitesimal perturbation, thus neglecting secondary orders terms of the fluctuating velocity components, the following system of linearized equations can be obtained:

$$\frac{\partial u'}{\partial t} + \overline{u}\frac{\partial u'}{\partial x} + v'\frac{\partial \overline{u}}{\partial y} + \frac{1}{\rho}\frac{\partial p'}{\partial x} - \frac{1}{Re}\nabla^2(u') = 0 \tag{2.30}$$

$$\frac{\partial v'}{\partial t} + \overline{u}\frac{\partial v'}{\partial x} + \frac{1}{\rho}\frac{\partial p'}{\partial y} - \frac{1}{Re}\nabla^2(v') = 0 \tag{2.31}$$

$$\frac{\partial w'}{\partial t} + \overline{u}\frac{\partial w'}{\partial x} + \frac{1}{\rho}\frac{\partial p'}{\partial z} - \frac{1}{Re}\nabla^2(w') = 0 \tag{2.32}$$

which has to be solved together with the continuity equation for the fluctuating velocity components:

$$\frac{\partial u'}{\partial x} + \frac{\partial v'}{\partial y} + \frac{\partial w'}{\partial z} = 0 \tag{2.33}$$

In the equations above ∇^2 is the Laplacian operator $\nabla^2 = \frac{\partial^2}{\partial x^2} + \frac{\partial^2}{\partial y^2} + \frac{\partial^2}{\partial z^2}$. Relating now the streamwise and spanwise perturbation velocity components through the normal perturbation vorticity

$$\eta' = \frac{\partial u'}{\partial z} - \frac{\partial w'}{\partial x} \tag{2.34}$$

and eliminating the perturbation pressure the following system of two equations in the normal to the wall perturbation velocity v' and the normal perturbation vorticity η' is derived:

$$\left[\left(\frac{\partial}{\partial t} + \overline{u}\frac{\partial}{\partial x} - \frac{1}{Re}\nabla^2\right)\nabla^2 - \frac{\partial^2 \overline{u}}{\partial^2 y}\frac{\partial}{\partial x}\right] v' = 0 \tag{2.35}$$

$$\left(\frac{\partial}{\partial t}+\overline{u}\frac{\partial}{\partial x}-\frac{1}{Re}\nabla^2\right)\eta' = -\frac{\partial \overline{u}}{\partial y}\frac{\partial}{\partial z}v' \tag{2.36}$$

which has to be solved with reference to the following boundary conditions:

$$(v',\eta') = 0 \quad for \quad y = 0 \tag{2.37}$$

$$(v',\eta') = 0 \quad for \quad y \to \infty \tag{2.38}$$

Assume now a wave form of the generic three dimensional perturbations, with the exception of the normal to the wall dimension y (being not homogeneous):

$$v'(x,y,z,t) = \tilde{v}(y)e^{j(\alpha x+\beta z-\omega t)} \tag{2.39}$$

$$\eta'(x,y,z,t) = \tilde{\eta}(y)e^{j(\alpha x+\beta z-\omega t)} \tag{2.40}$$

where α, β are the streamwise and the spanwise wavenumbers, while ω is the complex frequency. Substituting equations (2.39) and (2.40) into equations (2.35) and (2.36), the latter can be re-formulated as:

$$\left[(-j\omega+j\alpha\overline{u})\left(\frac{\partial^2}{\partial y^2}-k^2\right)-j\alpha\frac{\partial^2\overline{u}}{\partial y^2}-\frac{1}{Re}\left(\frac{\partial^2}{\partial y^2}-k^2\right)^2\right]\tilde{v} = 0 \tag{2.41}$$

$$\left[(-j\omega+j\alpha\overline{u})-\frac{1}{Re}\left(\frac{\partial^2}{\partial y^2}-k^2\right)\right]\tilde{\eta} = 0 \tag{2.42}$$

where $k = \alpha^2+\beta^2$. Equation (2.41) is the well known *Orr-Sommerfeld* equation, which reduces to the *Rayleigh* equation in case of inviscid flows ($Re \to \infty$). Combining $\tilde{v}$ and $\tilde{\eta}$ in a unique vector, equations (2.41) and (2.42) can be written in matrix form as:

$$j\omega \times \begin{pmatrix}\tilde{v}\\ \tilde{\eta}\end{pmatrix} = \begin{pmatrix}\nabla^2 & 0\\ 0 & I\end{pmatrix}^{-1}\begin{pmatrix}\Omega & 0\\ \Psi & \Sigma\end{pmatrix} \times \begin{pmatrix}\tilde{v}\\ \tilde{\eta}\end{pmatrix} = \Lambda\begin{pmatrix}\tilde{v}\\ \tilde{\eta}\end{pmatrix} \tag{2.43}$$

where

$$\Omega = -j\alpha\overline{u}\nabla^2 + j\alpha\frac{\partial^2\overline{u}}{\partial y^2}+\frac{1}{Re}\nabla^4 \tag{2.44}$$

$$\Psi = j\beta\frac{\partial\overline{u}}{\partial y} \tag{2.45}$$

$$\Sigma = j\alpha\overline{u}-\frac{1}{Re}\nabla^2 \tag{2.46}$$

It should be noted that the operator Λ is not self adjoint, i.e. the transient evolution of the system (2.43) is affected by modal interaction and cannot be described by a single eigensolution. This kind of system can therefore exhibit instability, or a so-called *transient growth* of the initial disturbance, on finite time scales while having all stable modes. Due to the transient instability of the system, non-linearities can be activated and transition may occur even if all the eigensolutions decay by them self. Note that in the case of $\beta = 0$, that is the flow is homogeneous in the spanwise direction, the term Ψ is null and the equations for $\tilde{v}$ and $\tilde{\eta}$ can be solved separately.

When studying the temporal stability of a given system, that is $(\alpha, \beta) \in \mathbb{R}$ and $\omega = c\alpha \in \mathbb{C}$ [21], the modal approach is to determine the most unstable eigensolutions associated with the highest growth of disturbance. Note that instead of considering the complex frequency ω as the eigenvalue of the problem, it is often used the complex phase speed c. In this context, the system becomes unstable if the imaginary part of one or more complex eigenvalues c is positive, which produce exponential amplification of the initial disturbance according to equations (2.39) and (2.40). When looking at the transient behaviour, eigenmodal analysis fails to predict the evolution of the system due to instability occurring at finite time scales. In this context, optimization techniques looking at the growth of the disturbance energy at $t << \infty$ have to be considered (see Butler and Farrel [18]). Once defined the energy of the disturbance as $E = (\tilde{v}, \tilde{v})$ (where $(,)$ indicates the inner product), the growth rate of an initially infinitesimal perturbation can be expressed by means of the following function:

$$G(\tau) = \frac{E(\tau)}{E_0} \tag{2.47}$$

which normalizes the energy of the disturbance at a finite time instant $t = \tau$ by its initial energy E_0. The transient analysis is therefore performed by solving an initial value problem to find the *optimal disturbance* maximizing the function $G(\tau)$ for a given set of α, β and Re. Amongst others, Andersson, Berggren and Henningson [7] and Luchini [68] used an optimization technique to determine the optimal disturbance in non-parallel boundary layers. The role of eigenmodal as well as non-modal instability in the BL transition will be further discussed in the following when discussing the different type of transition processes.

2.5 Transition mechanisms of the boundary layer

The transition of the BL from the laminar to the turbulent state is characterized by the breakdown of the ordered motion characterizing the laminar BL, causing the occurrence of turbulent spots. When the turbulent spots merge , the BL reaches the turbulent state as shown in figure 2.3. The statistical and dynamic evolution of the transition process is known to strongly depend on the flow conditions in terms of Reynolds number, free-stream turbulence and pressure gradient. Indeed, depending on the values of all these three parameters different type of transitions can occur, which are characterized by sensibly different amplification mechanisms of the disturbances growing into the boundary layer. With the aim of providing an overview of the main features of the transition mechanisms analyzed in details in this work, a brief description of the different type of laminar to turbulent transitions is provided in the following.

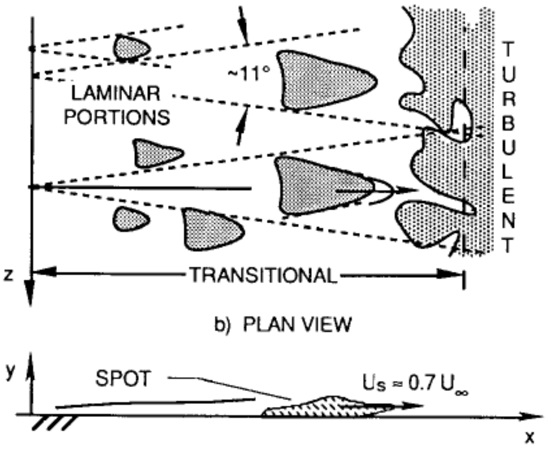

Fig. 2.3 Turbulent spots propagation and growth in a transitional boundary layer.

2.5.1 Natural transition

Natural transition takes place in attached boundary layers under a statistically steady mean flow with low Tu level ($< 0.5\%$). From the theoretical point of view, the natural transition occurs as a consequence of the modal instability of the linearized N-S operator reported in equation (2.43). The first modal solution of the Orr-Sommerfeld equation was obtained by Tollmien and Schlichting in case of 2D parallel flow, that is $\beta = 0$, where β is the spanwise wavenumber introduced in section 2.4. These eigensolutions of the viscous problem described by the Orr-Sommerfeld operator appear as streamwise two dimensional waves growing or decaying exponentially, whose secondary instability is known to promote the (natural) transition of the BL. The existence of such solutions was experimentally verified by Schubauer and Skramstad [101] in a zero-pressure-gradient boundary layer. If an amplified T-S wave grows above an amplitude of about 1% of the free-stream velocity, the flow becomes susceptible to secondary instability and nonlinearities become relevant [14]. This phenomenon is followed by a three-dimensional instability, leading to the formation of spanwise periodic vortices (with a specific rate of production), which then cause the breakdown of the laminar layer with the generation of turbulent spots in a narrow space strip. These spots finally merge resulting in the formation of a turbulent boundary layer. The natural transition is a rather slow process, needing a considerable length in the flow direction: it often happens in external aerodynamics, with a very low free-stream turbulence level. Natural transition is a susceptible process to all sorts of perturbations (see Abu-Ghannam and Shaw [1]). The main consequence of this high sensitivity is that the prediction of transition in external aerodynamics is a very delicate topic.

Note that since this work focuses on the transition process under turbine-like conditions, where Tu is always much higher than 0.5%, the response of the BL to the main flow parameters in case of natural transition was not considered here and no further description of this kind of transition will be presented.

2.5.2 By-pass transition

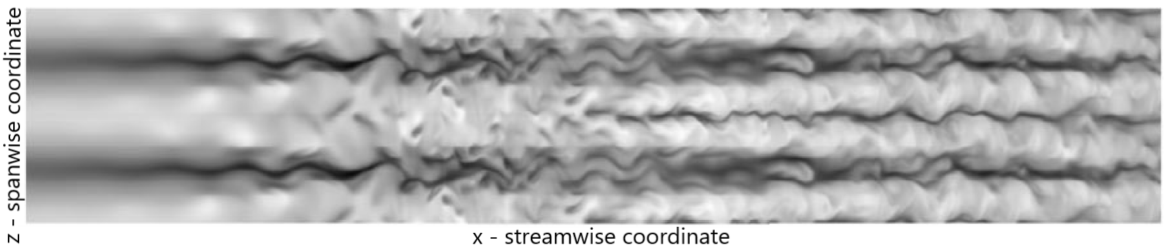

Fig. 2.4 Visualization of streak breakdown using the streamwise velocity component in a wall-parallel (x,z)-plane [14].

By-pass transition takes place under a sufficiently high turbulence intensity level, generally above 0.5%–1%. In this context, streamwise elongated structures (called streaks or Klebanoff modes) are known to drive the transition process, and are characterized by spanwise periodicity with a characteristic wavelength scaling with the boundary layer thickness (see e.g., Dick [26]). In this case the instability mechanism of the T-S waves is by-passed, obtaining a much faster flow breakdown. A visualization of the breakdown of BL streaks is shown in figure 2.4 [14]. Here grey scale from dark to light corresponds to negative to positive values.

From the mathematical point of view, a significant transient growth occurs in the case of by-pass transition (see Butler and Farrell [18], Schmid and Henningson [99]) due to the non self-adjoint N-S operator. Such growth is larger for disturbances mainly periodic in the spanwise direction, i.e.with low streamwise wavenumbers in a temporal formulation or low frequency in a spatial one. Note that the term out of diagonal in the N-S operator reported in equation (2.43), coupling the velocity and vorticity equations, is the only one directly depending on the spanwise wavenumber β. The transient amplification of initial disturbances may provoke the transition from the laminar to the turbulent state for Reynolds number sensibly lower than the one predicted by the linear modal stability. In this context, the eigenmodal stability fails to correctly predict transition, and the stability analysis is focused on solving an initial value problem aimed at finding the optimal disturbance maximizing the normalized disturbance energy at a given time for $t << \infty$ (see section 2.4). Andersson, Berggren and Henningson [7] and Luchini [68] found that a couple of counter-rotating streamwise oriented vortices is the optimal disturbance to promote streaks generation, whose breakdown promotes the BL transition. Indeed, this pair of counter-rotating vortices acts inducing the lifting-up of flow with low momentum toward the edge of the BL, while pushing down fluid characterized by higher velocity. This mechanism produces an alternating pattern of low- and high-speed streaks that is periodic in the spanwise direction. When boundary layers evolve beneath free-stream turbulence, low-frequency oscillations occur in the BL, while higher frequencies are dumped according to the *shear sheltering* phenomenon described by Zaki [134]. Inside the boundary layer, the elongated distortions reach high amplitude, which can be larger than 15% of the mean flow velocity [134]. The final stage is the secondary instability of particular streaks, which precedes breakdown into turbulent spots. The breakdown of BL streaks has received great attention in the past. The details of their amplification under free-stream turbulence have been studied experimentally (see e.g., Mandal et al [71] and Matsubara et al [78]) or using direct numerical simulations. Jacob and Durbin [46] for instance, analyzed the role of free-stream fluctuations in the breakdown of BL streaks. The high frequency disturbances that are filtered by the BL can indeed interact with unstable streaks that are lifted up toward the edge of the BL, promoting their breakdown thus transition.

State of the art on by-pass transition

In real application, such as turbine blades, high Tu levels trigger the formation of turbulent spots within the boundary layer avoiding the generation of the Tollmien-Schlichting waves and a by-pass transition mode typically occurs (Morkovin [85]). Hot-wire results allowed formulating correlations based on boundary layer integral parameters useful for the prediction of transition onset and length, as well as intermittency distributions accounting for the Tu level and the pressure gradient (see the works of Abu-Ghannam and Shaw [2], Narashima [86], Gostelow [36] and Emmons [31] for instance). The analysis of detailed hot-wire results for flat plates (see the classic work of Klebanoff [49] or the more recent papers of Roach et al. [94] and Westin et al. [126]) shows that elevated Tu levels penetrate inside the boundary layer inducing non null streamwise velocity fluctuations and Reynolds shear stress, responsible for the quick transition process.

Recent analysis stated that low frequency disturbances penetrate into the laminar boundary layer at different depth generating high- and low-speed streaky structures. Evidence of boundary layer streaks are provided by the experimental results of Mans et al. [72], as well as inspecting the instantaneous flow fields obtained by DNS (Jacob and Durbin [46], Heningsonn [44]) or PIV measurements (Mandal [71], Nolan [88]). Once generated, transient growth mechanisms increase (linearly) the streak amplitude, thus contributing to raise the velocity oscillations in the flow as well as the instability of the streaks. Moreover, as formulated by Luchini [68], the wall-normal rms profiles preserve the self-similar shape at the different (streamwise) positions once made dimensionless by means of the peak rms and the boundary layer displacement thickness. Several experiments carried out on flat plate prove the validity of the Luchini's model (see e.g., Matsubara [78] and Mandal [71]), as well as the transient growth of peak rms in the pre-transitional part of the boundary layer (see e.g., Westin et al. [126] and Nolan and Zaki [87]).

The breakdown of unstable traveling streaks induces the formation of coherent structures typical of the turbulent condition of the boundary layer, such as hairpin, cane and lambda vortices (see Mandal [71], Lengani et al. [59], [65] and Brandt [14]). Simoni et al. [103] show that the presence of this coherent structures are directly related to the intermittency behavior of the flow. Works describing the effects of the adverse pressure gradient are mainly confined to DNS analysis. Zaki et al. [133] show that the streaks amplification rate rises in the pre-transitional part of the boundary layer as the adverse pressure gradient is increased, thus shortening the transition length. The computational results reported in Nolan and Zaki [87] also show that the loci of maximum turbulent spot production rate (strictly related to the breakdown of streaks) are in the outer part of the boundary layer in the zero pressure gradient case, while they move very close to the wall in a strong adverse pressure gradient condition.

2.5.3 Separated flow transition

If a sufficiently strong adverse pressure gradient is imposed to the flow, the boundary layer evolving on a solid surface can separate giving origin to a region of reverse flow, i.e. the fluid near the wall starts to move in the opposite direction with respect to the main direction of the flow. Note that separation can involve both laminar and turbulent boundary layers, even if turbulent boundary layers are known to separate with stronger adverse pressure gradients. The separation position is identified as the location where the adverse pressure gradient causes the fluid layers at the wall to flow in the opposite direction with respect to the outer flow [22] and the streamline at zero velocity detaches from the wall. Upstream of the separation point, the velocity gradient at the surface is positive, and the shear stress acts

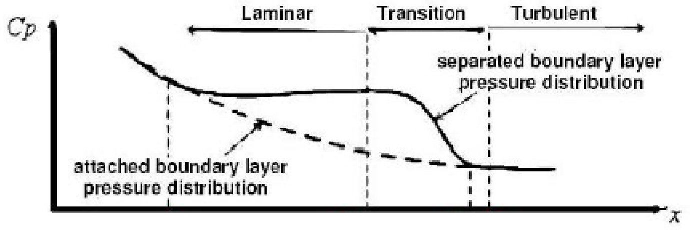

Fig. 2.5 Effect of the separation bubble on the pressure distribution along a solid wall.

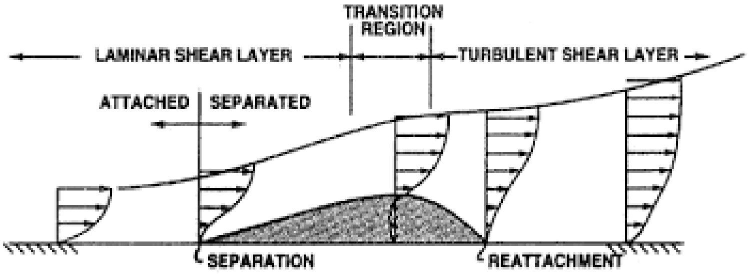

Fig. 2.6 Schematic representation of a laminar separation bubble. Occurrence of reverse flow is highlighted by means of mean velocity profiles.

in a direction opposite to the outer-flow motion. After separation, the velocity gradient at the surface is negative changing both the shear stress sign and direction. From this observation the separation point can be defined as the coordinate on the solid wall where the shear stresses cross the zero line, i.e.:

$$\tau_w = \mu \left(\frac{\partial u}{\partial y} \right)_{y=0} = 0 \tag{2.48}$$

The separated flow transition can occur in turbomachinery on high-lift turbine blades profiles, resulting in a modification of the pressure distribution along the profile, as shown as an example in figure 2.5. Depending on the main flow parameters (Re, Tu and APG), the size of the separation bubble can vary significantly, moving from the so called *short bubble* to the *long bubble* configuration (see Gaster [33]). The difference between the two kind of bubbles is given by their effects on the overall pressure distribution along the surface. Short bubbles have only a local displacement effect, and before and after them the pressure distribution on the solid wall is close to that predicted by the inviscid theory. On the contrary, long bubbles interact with the exterior flow in such a way that the pressure distribution over the surface is significantly modified. Variations in the angle of incidence of the flow over an airfoil or variation of the velocity of the flow (thus Reynolds number) can force a separation bubble to pass from the *short* to the *long* configuration, with a consequent increase of losses and a stronger modification of the loading distribution. This phenomenon is called *bursting*.

When separation occurs, the flow may reattach if laminar to turbulent transition occurs into the separated shear layer. Downstream of the detachment position, the velocity fluctuations are amplified in the separated shear layer due to the inviscid Kelvin-Helmholtz (K-H) instability process (see e.g., Sarkar [96] and Lardeau et al. [56]). Fluctuations grow up to the bubble maximum displacement position, where saturation occurs (Simoni et al. [109]). At this position, the separated shear layer rolls and an intense vortex shedding phenomenon occurs (see Alam and Sandham [4]). The breakdown of these large scale vortical structures promote the transition of the separated shear layer, thus reattachment, as described by Marxen and Henningson [73] and Simoni et al. [106].

The transition of separated BL can be studied referring to the linearized system reported in equation (2.43) in the case of $Re \to \infty$, that is an inviscid problem is considered. Indeed, when the BL detaches from the wall, its behaviour is similar to that of a free shear layer and the equation of *Rayleigh* can be referred to for the analysis of its (in)stability. The separated flow transition is therefore studied starting from the Rayleigh equation where a base flow characterized by high velocity gradients, as those shown in figure 2.7, is subjected to small disturbance in the cross-flow direction. Note that the mean velocity distribution $\overline{u}(y)$ occurring in a laminar separation bubble is well represented by means of the simplified schemes of figure 2.7. Finally, the K-H instability takes place as unstable eigensolutions of the inviscid linearized problem (equation (2.43) for $Re \to \infty$), only in a specified range of wavenumbers (see e.g., Burgmann et al. [16]). More precisely, the eigenvalues of the inviscid eigen-problem can be real (neutral) or complex (growing or dumped) depending on the wavenumbers considered with respect to the thickness of the shear layer ($2h$ in figure 2.7).

State of the art on separated flow transition

Over the past few years LES, DNS and PIV systems gave insight into the main dynamics driving the unsteady behavior of separated flows. The strong three dimensional effects acting through the spanwise instability of the K-H rolls in the surrounding of the bubble maximum displacement have been studied in detail both experimentally (Burgmann and Schröder [17] and Kurelek et al. [51]) and numerically (Marxen et al. [75], Jones et al. [47]). The three dimensional characterization of the vortex breakdown of a laminar separation bubble over an airfoil is provided by means of scanning PIV by Burgmann et al. [15]. Even though the

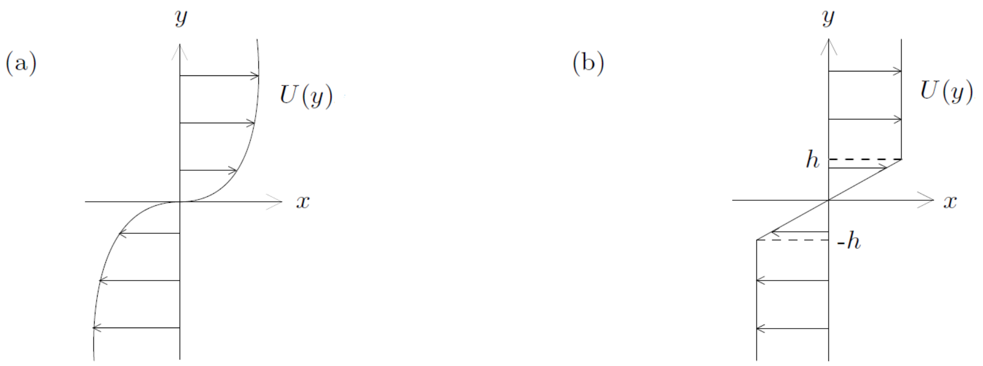

Fig. 2.7 (a) Unbounded smooth shear flow.(b) Piecewise-linear unbounded shear flow.

dynamics at work in laminar separation bubbles are well highlighted in the literature, the effects of the flow parameters on the main mechanisms driving the separated flow transition process are far from being completely understood. In the fore part of the separated flow region, the amplification of the velocity fluctuations is typically well predicted by Linear Stability Theory (LST), that provides remarkable agreement with experiments, as shown for example by Häggmark [38], Marxen et al. [75] and Yarusevych et al. [130]. The stability characteristics of different mean velocity profiles are reported in the work of Dovgal et al. [29]. Diwan and Ramesh [27] provide an experimental and theoretical analysis of the wall distance effects on the most unstable frequency. They clearly show that, once the distance from the wall is sufficiently high, the wall effects vanish and both maximum amplified frequency and growth rate approach the values predicted for a free-mixing layer. Diwan and Ramesh [27] argued that the inviscid instability characterizing the rear part of the bubble is the natural extension of the instability starting in the attached adverse pressure gradient region of the boundary layer.

In the literature, the response of laminar separation bubbles to external disturbances is mainly investigated imposing, either experimentally or numerically, controlled upstream perturbing waves. In this context, the activity carried out at Stuttgart University provides one of the most comprehensive overview of the influences due to different parameters of the perturbing waves. Maucher et al. [79] show the response of a laminar separation bubble to monochromatic waves at the most unstable frequency (as predicted by LST) with different amplitudes. They found the same growth rate and saturation level irrespective of the forcing amplitude. Hence, the overall bubble size reduction they observed is mainly driven by the higher initial wave amplitude. Similar conclusions are reached in the DNS of Jones et al. [47], where disturbances are created by sinusoidal perturbations of the wall normal velocity exciting the LSB forming on a NACA-0012 airfoil.

In the works of Marxen et al. [75] and Lang et al. [54] PIV and LDV data were decomposed by a Fourier based technique in order to identify streamwise growth rate and wall-normal amplitude of different modes. The data highlight that the attached part of the boundary layer is mainly affected by spanwise waves, since the amplitude of the corresponding mode is higher than those characterizing the shear layer most unstable frequency. Conversely, this latter is sensibly amplified downstream of the separation and becomes the dominant mode at saturation position. The effects due to the superposition of spanwise wavenumbers, simulating the presence of streaky structures or Görtler vortices, to the most unstable shear layer frequency have been studied in Lang et al. [53]. The authors show that streaky structures induce transient growth in the fore part of the separation bubble, confirming what observed in flat plate experiments and computations for attached boundary layers (Jacob and Durbin [46], Brandt et al. [14], Zaki [132]). Interestingly, a variation of the amplitude of the spanwise wave does not influence the growth rate and the saturation level of the most unstable frequency. On the other hand, spanwise waves clearly influence the breakdown process of the K-H rolls in the rear part of the bubble, as described in Marxen et al. [74].

All these works give an exhaustive view of the theoretical expectation for the development of monochromatic, or eventually simply composed wave trains. The inspection of the effects due to the superposition of a multitude of waves with different amplitude (whose importance is also highlighted by Spalart and Strelets [112]) should further contribute to the understanding of the dynamics driving laminar separation bubbles transition, since homogeneous free-stream turbulence represents an unsteadiness source more complex than controlled oscillations. The lack of a proper formulation of the disturbance spectra exciting the laminar separation bubbles can also justify the marked differences encountered in the recent DNS works, as stated by Jones et al. [47]. In Lardeau et al. [56] the procedures adopted to introduce free-stream oscillations in LES are described in detail. They show how the high frequency containing energy oscillations of the spectrum mainly affect the breakup process of vortices downstream of the bubble maximum displacement position. Also Langari and Yang [55] analyzed the effects due to Tu variations providing velocity disturbances on the free-stream rather than applying a normal to the wall velocity forcing. A careful observation of the vorticity contours shows the ability of these simulations in reproducing streaky structures that affect, at high Tu level, the fore part of the laminar separation bubble. Moreover, low frequency oscillations present in real flows can also contribute to the modulation of the vortex shedding phenomenon, as highlighted in the time-resolved PIV data analysis of Hain et al. [40]. The amplitude modulation of the incoming disturbances seems to induce a feedback loop involving the inviscid-viscous interaction and the time-dependent mean flow deformation, as described in Marxen and Henningson [73] and Marxen et al. [74].

The experimental investigation of the effects due to the independent variation of the main flow parameter governing the transition process is nowadays of great importance due to the limits of high-fidelity numerical simulations (LES and DNS) in terms of computational costs. For this reason, the numerical characterization of the simultaneous effects of Tu, Re and APG are usually obtained by cross-checking results of different works. This is the reason why this work is aimed at the characterization of the combined effects of all these three parameters. Some experimental works in the past tried to characterize the response of laminar separation bubbles to both Tu level and Reynolds number variation. In the work of Volino [120] the variation of the time-mean structure of a laminar separation bubble has been characterized by means of hot-wire instrumentation. Results clearly show that the higher the Reynolds number the shorter the bubble length due to the anticipation of the bubble maximum displacement and reattachment positions. Similar trend has been found by the author raising the Tu level. However, the shear layer thickness at separation appears more affected by the Reynolds number variation and it becomes significantly thinner at higher Reynolds numbers. In the work of Yaras [129] the positions characterizing the separated flow transition (i.e. the separation, maximum displacement and reattachment positions) on a flat plate subjected to a strong adverse pressure gradient have been identified to formulate correlations able to predict the overall bubble structure as a function of Reynolds number, Tu and integral length scale. In the pioneering work of Gaster [33], the time traces of velocity oscillations clearly highlight the periodic activity of the vortex train shed by the bubble, while the variation of the peak frequency of the shedding phenomenon developing on a NACA 0018 airfoil is reported in Boutilier and Yarusevych [12]. Their results, obtained for a wide range of Reynolds numbers and different angles of attack and with low Tu level typical of airfoil flight conditions, clearly show that a power law links the peak frequency to the Reynolds number.

2.5.4 Wake-induced transition

In turbomachinery, a fundamental role is played by impinging wakes produced by upstream blades, which interact with the attached or even separated boundary layer of the following rows [26]. When the perturbations carried by the wakes is moderate, the transition process is similar to the steady case (without incoming wakes) and a by-pass like transition takes place due to the free-stream turbulence intensity level typical of turbomachinery. In this context the wake-induced transition can be outlined by figure 2.8. Following a path under wake, the attached boundary layer starts as laminar, undergoing transition as far as it moves downstream until it becomes turbulent. Between two wakes, the evolution of the boundary layer is similar to the one under the passage of the wake, but with a later transition onset and completion. This is due to a relaxation of the boundary layer towards a laminar state, even if the velocity profile stays close to the turbulent one. The effect of these combined events is the *calming* of the boundary layer, that increases its resistance to transition and separation. Turbulent spots generated by the wake can even periodically suppress or reduce the dimensions of a separation bubble occurring along the surface.

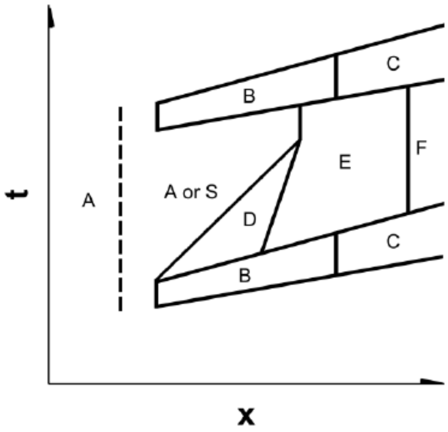

Fig. 2.8 Diagram of wake-induced transition. The A zone stands for laminar flow, B is for transitional under wake impact, C represent turbulent flow after the impact, D is the calmed zone, E and F are, respectively, transitional and turbulent between the passage of two wakes. S represents the condition of separated boundary layer.

A strong kinematic impact of wakes can instead significantly alter the transition process. The leading part of the jet causes an acceleration in the boundary layer thus a reduction of pressure. Since the pressure is higher in the center of the jet due to the occurrence of a stagnation point on the blade, the BL can experience a transient adverse pressure gradient in the leading zone of the jet, causing local flow reversal. Kelvin-Helmholtz instabilities can then occur in the outer part of the boundary layer, leading to a much faster breakdown than with by-pass transition in a statistically steady mean flow (see Dick [26]).

Wake-induced transition will not be analyzed in the present work, thus this transition mechanism will not be further discussed here. However, a wakes generation device has been installed in the testing facility and the effects of impinging wakes will be analyzed in further works.

2.6 Need for transition modelling

As highlighted in the previous sections, transition takes place in different ways depending on the flow conditions. In external aerodynamics the natural transition driven by the T-S waves typically occurs, while in turbomachinary applications by-pass transition and separation induced transition occur as a consequence of the elevated Tu levels and APG imposed to the flow. The analysis of the different transition mechanisms reported in the previous sections highlighted the substantial differences between the different transition processes from both the physical and mathematical point of view, resulting in the difficulty of developing transition models applying in such a wide range of flow conditions.

The present need for transition modelling arises from the impossibility to make high fidelity simulations (DNS) in the everyday engineering applications due to the high computational costs. This is due to the complex geometries and elevated Reynolds numbers that typically characterize the industrial applications in which CFD solver are used. It follows that the most CFD solvers adopted in modern engineering problems are Reynolds Averaged Navier Stokes (RANS) based codes, which require reliable transition models to correctly predict the transition process. One of the main issue related to the implementation of transition models in RANS based solver is that the averaging procedure leading to the formulation of the RANS equations does not allow the consideration of linear amplification effects, which have been shown to drive the initial step of transition, until saturation occurs and nonlinearities dominate. Methods based on the stability analysis, like the ones proposed by Smith and Gamberoni [111] and van Ingen [119] avoid this limitation. However, these methods typically refer to non-local operations and quantities, which are not easily implemented into today's CFD solver [81]. The correct prediction of the boundary layer transition process therefore represents a challenge to RANS solvers, since the momentum transfer due to the Reynolds stress can significantly alter the performance of components of practical interest, like aircraft wings or turbomachinery blades. Two-equation models (like $k-\varepsilon$ or $k-\omega$) based on the eddy viscosity concept (EVM) represent the most viable tools for the closure of RANS solvers (Leschziner [83]). Transition is frequently modelled by discriminator functions (Kubacki and Dick [50]), dynamic equations for intermittency (Menter et al. [81]), or the laminar kinetic energy concept (Pacciani et al. [90], Dick and Kubacki [26]). Irrespective of the turbulence and transition models adopted into the numerical scheme, model constants and/or damping functions and wall-limiting values of the eddy viscosity are typically calibrated and tuned by fitting experimental or DNS data. In the past, extensive works have been carried out with the aim of identifying correlations useful for the definition of transition related quantities. Examples are the correlation of Abu-Ghannam and Shaw [1] for the prediction of the transition onset, the intermittency based quantities reported by Gostelow et al. [36] for the definition of the turbulent spot production rate in case of by-pass transition as a function of the APG and Tu level, as well as the correlations based on the comprehensive literature overview reported in the work of Mayle [80]. However, all these mentioned works are mainly focused on databases and correlations for attached boundary layers, and the rare exceptions describing separating flows are developed with a scarce population of the data ensemble, thus reducing the accuracy of the correlations and the possibility to account for a large variation of the most influencing parameters. Since the mechanisms driving the transition of attached boundary layers (for both natural and by-pass cases) are completely different from those leading to the separated flow transition process (see Lengani and Simoni [60] and Istvan and Yarusevych [45]), the construction of a new test case focused on both separated and attached flows can help to improve the capability of CFD codes to correctly predict the evolution of transitional flows.

2.7 Reynolds number effects on the transition process

The Reynolds number is well known to affect the development of the boundary layer along a solid surface. When Reynolds number is increased, the effects of the inertial forces grow respect to the viscous ones, thus reducing the thickness of the boundary layer δ_{99}. As presented in section 2.1 for the Blasius solution, at a given station x along a flat plate the boundary layer thickness decreases as a function of $Re_x^{\frac{1}{2}}$ in case of laminar flow and as $Re_x^{\frac{1}{5}}$ in case of a turbulent boundary layer. Similar trends can be observed considering the integral parameters δ^* and θ calculated for a laminar boundary layer:

$$\theta \propto \frac{1}{Re_x^{\frac{1}{2}}} \tag{2.49}$$

$$\delta^* \propto \frac{1}{Re_x^{\frac{1}{2}}} \tag{2.50}$$

As Re_x is increased, both displacement thickness and momentum thickness decreases for a fixed position on the flat plate, reducing the blockage effect and viscous losses.

For what concerns the effects of Reynolds number on the transition process, when the local Reynolds number (Re_x) reaches a certain value, that is, for a given velocity field a certain position on the surface is reached, transition occurs. The value of the local Reynolds number at which transition occurs strongly depends on the geometry considered (e.g. flat plate, pipe). Even though Re_x is generally adopted to indicate the position at which transition occurs, another useful dimensionless parameter considered for the study of transition is the momentum thickness Reynolds number:

$$Re_{\theta} = \frac{U_e \theta}{\nu} \tag{2.51}$$

Re_{θ} is generally referred to in literature for the development of empirical correlations able to predict the development of the transition process in terms of transition onset and length. This is because the momentum thickness at a given position is a function of the pressure gradient imposed to the flow and the boundary layer state up to that position (see the Von Karman equation 2.29). It follows that the momentum thickness Reynolds number evaluated for instance at the separation position in case of separated flows, takes into account for the evolution of the BL from the leading edge up to the specified position, differently from the local Reynolds number simply based on the streamwise position considered. In this context, the correlation proposed by Mayle [80] is one of the most popular ones for the prediction of the Reynolds number based on the distance between separation and transition onset $(Re_x)_{st}$ as a function of the momentum thickness Reynolds number at separation $(Re_{\theta,s})$:

$$(Re_x)_{st} = 300 Re_{\theta,s}^{0.7} \quad for\, short\, bubble \tag{2.52}$$

$$(Re_x)_{st} = 1000 Re_{\theta,s}^{0.7} \quad for\, long\, bubble \tag{2.53}$$

Although the correlations proposed by Mayle for the prediction of the transition onset are different for short or long bubble, the correlation proposed for the prediction of the transition length Reynolds number (Re_L) is the same for both the bubble configurations:

$$Re_L = 400 Re_{\theta,s}^{0.7} \tag{2.54}$$

Several other works carried out in the past have focused on the effects of the Reynolds number on the development of the transition process in case of both attached and separated flows. Volino [120][121] analyzed the effects of the Reynolds number on the development of laminar separation bubble over turbine blade profiles, showing that the higher the Re, the shorter the bubble. Since the reattachment is induced by the BL transition, it follows that the higher the Re, the more upstream transition occurs. The same holds in case of attached flows, where the transition onset moves upstream if the Reynolds number is increased [100]. Indeed, in terms of stability properties, the Reynolds number is the most influencing parameter affecting the properties of the Orr-Sommerfeld operator, as shown in the previous sections.

2.8 Turbulence intensity effects on the transition process

As previously mentioned in section 2.5, the free-stream turbulence intensity is known to strongly affects the transition process. For a low level of turbulence, the disturbances in the boundary layer are amplified in the form of the 2D Tollmien-Schlichting waves, while for higher turbulence level ($Tu > 0.5 - 1\%$) this mechanism is by-passed and transition due to streamwise streaks is observed. Free-stream turbulence is responsible for the penetration of velocity fluctuations inside the boundary layer and, on the other hand, can promote the breakdown of the structures that have been amplified inside the boundary layer by means of different interaction mechanisms between the BL and the free-stream region (see e.g., Jacob and Durbin [46]). Whatever the transition process is (natural, by-pass or separation induced), increasing the free-stream turbulence is reflected in a higher value of the initial disturbances that will be amplified by the BL and the transition occurs upstream.

Turbulence appears to be the most important parameter for natural transition correlations, as shown in the one proposed by Hall and Gibbins [41] for the prediction of the start of transition:

$$Re_{\theta S} = 163 + exp(6.91 - Tu) \tag{2.55}$$

Where $Re_{\theta S}$ is the momentum thickness Reynolds number at transition onset. Note that the higher turbulence level the lower is $Re_{\theta S}$ at transition, thus the transition onset location moves upstream. The momentum thickness Reynolds number at the end of transition ($Re_{\theta E}$) is instead related to $Re_{\theta S}$ in the form:

$$Re_{\theta E} = 2.667 Re_{\theta S} \tag{2.56}$$

which is valid for low Tu level up to the high values typical of turbomachinery applications. In case of by-pass transition, Mayle proposed the following correlation for the momentum thickness Reynolds number at the transition onset:

$$Re_{\theta S} = 400 Tu^{-\frac{5}{8}} \tag{2.57}$$

Where $Re_{\theta S}$ is again expressed as a function only of the free-stream turbulence. However, to have a more reliable prediction of the transition onset, the effects of pressure gradient should be also considered (see Abu-Ghannam and Shaw [1]), as shown in the following section.

In case of both natural and bypass transition with zero pressure gradient, Mayle [80] developed a simplified correlation for the spot production parameter $\hat{n}\sigma$ as a function of free-stream turbulence:

$$\hat{n}\sigma = 15 \cdot 10^{-12} Tu^{\frac{7}{4}} \tag{2.58}$$

Here $\hat{n} = n\nu^2/U_e^3$ is the dimensionless spot production parameter, while σ is the Emmon's constant equal to 0.27. The spot production parameter $\hat{n}\sigma$ is an important parameter in the transition analysis which is directly linked to the transition length. Indeed, a function called *intermittency* can be defined being representative of the fraction of time during which the flow over any point P on a surface is turbulent. According to the original formulation of Emmons the intermittency function is defined as:

$$\gamma(P) = 1 - exp[-\int\int\int g(P_0)dx_0dz_0dt_0] \tag{2.59}$$

where $g(P_0)$ is the production term of turbulent spots, while their propagation and growth in time are accounted for by means of the integrals over the (x,z,t) domain. When $\gamma = 0$ the flow is laminar, while when $\gamma = 1$ is turbulent. Successively, Dhawan and Narasimha [25] wrote the production term $g(P_0)$ appearing in the Emmons' equation as a function of the turbulent spot production rate n defined for unit distance in the spanwise direction z, obtaining the following formulation for the intermittency function:

$$\gamma(x) = 1 - exp[-\frac{n\sigma}{U_e}(x - x_t)^2] \quad (x \geq x_t) \tag{2.60}$$

where x_t is the transition onset location. Introducing the local Reynolds number $Re_x = xU/\nu$, the previous equation can be rewritten as:

$$\gamma(x) = 1 - exp[-\hat{n}\sigma(Re_x - Re_{x_t})^2] \quad (x \geq x_t) \tag{2.61}$$

where $\hat{n}$ is the dimensionless spot production parameter appearing in equation 2.58. It is clear that, if the spot production parameter $\hat{n}\sigma$ increases, the gradient of the intermittency function γ becomes higher. Comparing now equations 2.61 and 2.58, it follows that the turbulence intensity acts reducing the transition length. Later, Suzen et al. [114] implemented a new correlation starting from the one proposed by Mayle, which is valid also in case of non-zero pressure gradient defined as:

$$\hat{n}\sigma = F(K) \cdot \hat{n}\sigma_{zpg} \tag{2.62}$$

$$F(K) = 10^{-3227K^{0.5985}} \quad (K > 0) \tag{2.63}$$

$$F(K) = (120 - 100Tu^{-0.5} + 850Tu^{-3})^{[1-exp(0.75 \cdot 10^6 K \cdot Tu^{-0.7})]} \quad (K < 0) \tag{2.64}$$

Where $\hat{n}\sigma_{zpg}$ refers to the spot production rate in case of zero pressure gradient and $F(K)$ is a function of both turbulence and K, with this latter representing an acceleration parameter defined by

$$K = \frac{\nu}{U_e^2}\frac{dU_e}{dx} = \frac{\lambda_\theta}{Re_\theta^2} \tag{2.65}$$

To keep into account for the effects of turbulence intensity in case of separated flows, Suzen [114] proposed the following correlation for the transition onset:

$$(Re_x)_{st} = 874 Re_{\theta,s}^{0.71} exp(-0.4Tu) \tag{2.66}$$

From which it is evident that the length necessary for transition to take place, proportional to the transition onset Reynolds number $Re_{x,st}$, reduces when increasing the free-stream turbulence intensity.

2.9 Pressure gradients effects on the transition process

The presence of an adverse pressure gradient is well known to strongly affect the flow development, inducing a further thickening of the boundary layer. Furthermore, the thickening of the boundary layer of turbine blades or flat plate profiles with imposed pressure variation generates a remarkable increasing in the loss of momentum. This can be seen recalling the Von Karman equation introduced in section 2.2:

$$\frac{d\theta}{dx} + \frac{\theta}{U_e}\frac{dU_e}{dx}[2 + H_{12}] = \frac{c_f}{2} \tag{2.67}$$

Different correlations have been proposed for the prediction of the transition onset in case of non-zero pressure gradient for both natural and bypass transition. Of great interest is the correlation proposed by Abu-Ghannam and Shaw [1], that keeps into account for the pressure gradient in the streamwise direction through the dimensionless parameter λ_θ already introduced in equation 2.65. When natural transition occurs, then λ_θ can be expected to play an essential role in the transition process [80], and the critical momentum thickness Reynolds number for which transition starts can be computed by means of the following equation derived by Abu-Ghannam and Shaw [1]:

$$Re_{\theta S} = 163 + exp\left(F(\lambda_\theta) - \frac{F(\lambda_\theta)}{6.91} Tu\right) \tag{2.68}$$

where:

$$F(\lambda_\theta) = 6.91 + 12.75\lambda_\theta + 63.64\lambda_\theta^2 \quad (\lambda_\theta < 0) \tag{2.69}$$

$$F(\lambda_\theta) = 6.91 + 2.48\lambda_\theta - 12.27\lambda_\theta^2 \quad (\lambda_\theta < 0) \tag{2.70}$$

Equation 2.68 gives curves that are shown in figure 2.9. It should be noticed that, for a given level of turbulence, the influence of the adverse pressure gradient in promoting transition is greater than the capability of a favourable pressure gradient in delaying it. Moreover, the effect of the pressure gradient is diminished as the turbulence level increases.

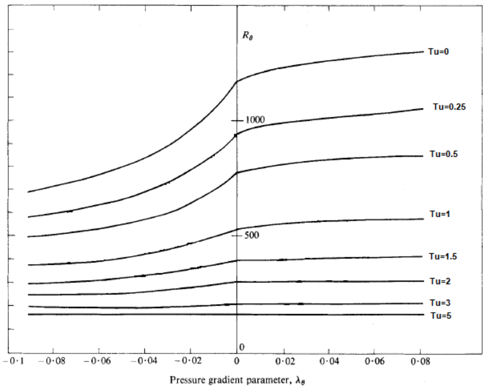

Fig. 2.9 Momentum thickness Reynolds number computed at the transition onset for different values of λ_θ and free-stream turbulence [1].

Abu-Ghannam and Shaw [1] also proposed a correlation for the momentum thickness Reynolds number at the end of transition $Re_{\theta E}$ which is valid for both adverse and favourable pressure gradient:

$$Re_{\theta E} = 540 + 183.5(Re_L 10^5 - 1.5)(1 - 1.4\lambda_\theta) \tag{2.71}$$

Note that in this formulation the Reynolds number based on the transition length (Re_L) is considered. It was first defined by Dhawan and Narashima [25] based on a length L_γ, over which the intermittency (defined in equation 2.61) increases from 0.25 to 0.75; furthermore, Dunham [30] demonstrated that the total length of transition L is proportional to L_γ as $L = 3.36L_\gamma$. Once L is known the Reynolds number Re_L can be calculated, thus $Re_{\theta E}$.

If the adverse pressure gradient imposed to the flow is sufficiently high, the boundary layer separates, as previously mentioned in section 2.5. In this context, the reference criterion for the estimation of the laminar separation position expressed in terms of the momentum thickness Reynolds number at separation is the criterion of Thwaites [117]:

$$Re_{\theta,s}^{2}K \leq -0.0082 \tag{2.72}$$

where K is the acceleration parameter defined in equation 2.65. Note that equation 2.72 implies that the momentum thickness Reynolds number at separation is automatically fixed if the distribution of K, i.e. the pressure gradient imposed to the flow, is known. The case of turbulent boundary layer separation was investigated with a similar approach by Buri, who proposed the following correlation for the momentum thickness Reynolds number at separation:

$$Re_{\theta,s}^{5/4}K \leq -0.050 \tag{2.73}$$

Comparing these two equations, it is clear that a turbulent boundary layer resists more to the separation if compared with a laminar one, being capable of sustaining higher adverse pressure gradients, has highlighted by the different exponent of $Re_{\theta,s}$. In case of laminar separation, the correlation that is widely adopted for the prediction of the transition onset Reynolds number is the one proposed by Suzen et al. [114] defined in equation 2.66 and reported here:

$$(Re_x)_{st} = 874Re_{\theta,s}^{0.71}exp(-0.4Tu) \tag{2.74}$$

Note that, once $Re_{\theta,s}$ is computed as a function of the pressure gradient imposed to the flow by means of equation (2.72), then $(Re_x)_{st}$ can be obtained.

Chapter 3

Test facility and experimental devices

In order to analyze with great details the transition and separation processes of the boundary layer for different combinations of Re, Tu and APG, a new flat plate test section has been designed and installed in the laboratory of Aerodynamics and Turbomachinery of the University of Genova. The previous test section, where preliminary results have been acquired, only allowed the variation of the flow Reynolds number and Tu level, since it was designed with a fixed endwall geometry. To overcome this limitation, thus making possible to explore also the effect due to the APG imposed to the flow, a variable area opening test section has been designed and commissioned in the present work. The core of both the test sections adopted in this work is constituted by a thick flat plate. The advantage of the flat plate configuration consists in the possibility of a detailed characterization of the boundary layer development due to the simplified geometry and the possibility to achieve a larger scale of the phenomena analyzed. Moreover, both the test sections allowed the use of both intrusive and non-intrusive instrumentation for a detailed characterization of the transition process.

3.1 The wind Tunnel

The wind tunnel installed in the laboratory of Aerodynamics and Turbomachinery of the University of Genova is an open-circuit low-speed wind tunnel. The mass flow rate inside the wind tunnel is supplied by a centrifugal fan actuated by an asynchronous three-phase electric engine, with a nominal power of 55 kW. The engine is regulated by means of an inverter and the control system of the inverter installed in the facility allows a frequency adjustment with a resolution of 0.01 Hz. Varying the output frequency of the inverter allows the variation of the rotational speed of the fan, which results in a variation of the velocity of the air inside the wind tunnel and therefore in a variation of the flow Reynolds number.

The bell mouth is located on the upper side of the fan (see figure 3.1) and it is provided with a filter that prevents particles of dust and other impurities to be sucked by the fan. Dust particles can stick to the walls of the test section, which is equipped with optical accesses, generating bright reflections that drop the accuracy of optical measurements close to the wall. A settling chamber is then interposed between the fan and the test section, with the aim of uniforming the flow and reducing the spontaneous turbulence of the tunnel. In the settling chamber, five screens and a honeycomb are mounted. Screens are constituted by a thin metal mesh used to reduce the scale of turbulence by acting both on the large-scale structures and on the smaller ones produced by the interactions between the flow and the sidewalls and other tunnel elements. After the passage through the screens the flow can be considered uniform, but it is far from laminar, being animated by small-scale vortices that need to decay. After the five metal screens a honeycomb composed of small hexagonal shaped holes obtained by bending a thin metal sheet is used to re-direct the flow by forcing it to pass through its cells in only axial direction, allowing the survival of only the axial component of velocity and further reducing the turbulence level.

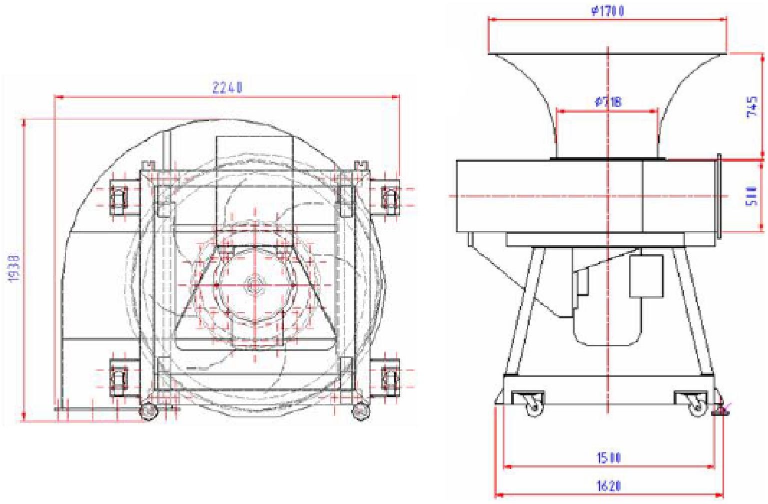

Fig. 3.1 Drawing of the fan installed in the wind tunnel

Downstream of the settling chamber a converging duct is installed, connecting the chamber to the test section, with a length of 420 mm and an area ratio of 2.77. The convergent accelerates the flow from the low velocity typical of the settling chamber to the velocity required for the condition selected for the data acquisition. During the acceleration, the boundary layer developing on the sidewalls of the tunnel reduces its thickness. Moreover, a continuous slot for the suction of the boundary layer developing on the side walls of the wind tunnel is installed upstream of the test section. At the end of the convergent part of the channel, turbulence generating grids can be located to induce a controlled Tu level at the inlet of the test section, as illustrated in figure 3.2. After the test section, the air is sucked and

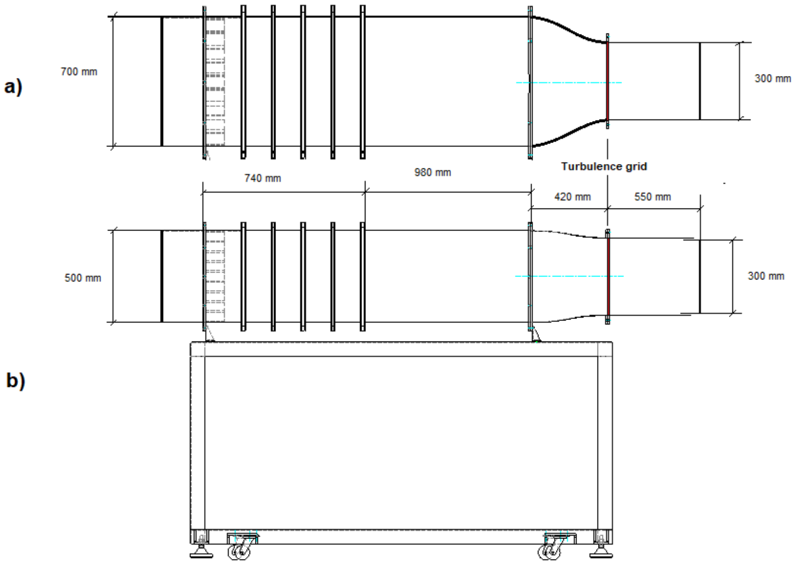

Fig. 3.2 (a) top view and (b) side view of the settling chamber and the convergent section of the wind tunnel. The location of turbulence generating grids is highlighted in the figure.

expelled out of the laboratory. A valve installed on the exit duct allows setting the pressure downstream of the test section.

3.2 The test section

The results obtained by two main measuring campaigns will be discussed in this work. During the first experimental campaign, the effects of the Re and Tu variation on the transition process in case of both separated and attached flows have been experimentally characterized with reference to the test section depicted in figure 3.3, which was originally installed in the wind tunnel adopted in this work. Note that in this case the adverse pressure gradient imposed to the flow was fixed due to the impossibility of varying the geometry of the test section. With the aim of studying the combined effects of Re and Tu for different APG, as well as to further validate and extend the analysis carried out in the first part of this work, a new test section, equipped with moving endwalls, has been designed (figure 3.4), allowing the acquisition of a large number of flow conditions regarding a large and independent variation of Re, Tu and APG. The comparative analysis of the experimental data acquired by means of both the test sections reported in figures 3.3 and 3.4 highlighted the consistency of the results obtained for all the conditions tested.

As shown in figure 3.3, the test section used in the first part of this work consists of

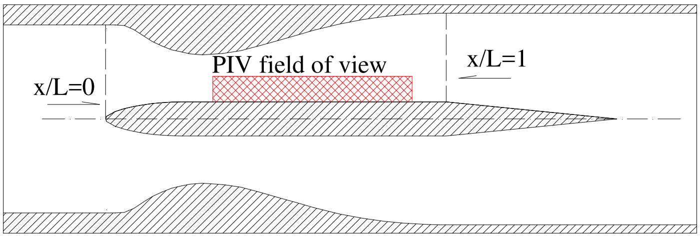

Fig. 3.3 Scheme of the *fixed-geometry* test section originally installed in the wind tunnel. The APG imposed to the flow is fixed.

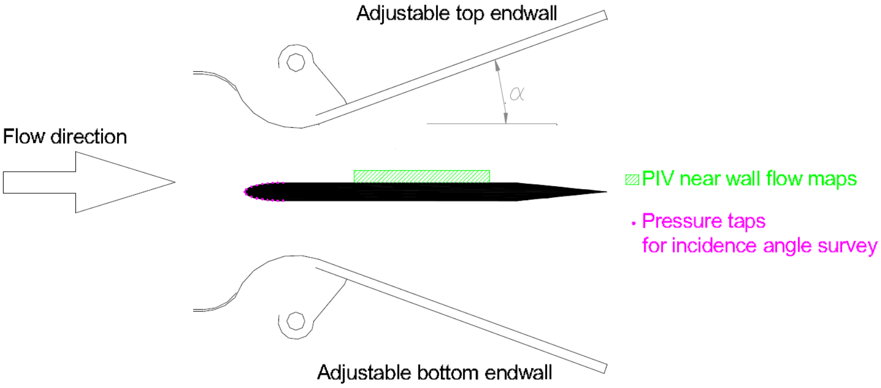

Fig. 3.4 Scheme of the new *variable geometry* test section designed in this work. The APG imposed to the flow can be adjusted by means of the movable endwalls.

a thick flat plate with a length of 200 mm, a 4:1 elliptic leading edge and a sharp trailing edge. This plate is located between two contoured walls that produce the prescribed adverse pressure gradient typical of Ultra-High-Lift turbine profiles. In this case, the fixed endwall geometry was scaled from the Talan and Hourmouziadis [115] test case. Further data and examples of results obtained in this test section are well documented in previous works of the research group ([61],[105],[106]).

The new test section shown in figure 3.4 still consists of a flat plate which is installed in a variable area opening endwall channel, allowing the variation of the pressure distribution along the plate. The front part of the test section, from the plate leading edge to the geometrical throat of the channel, is fixed and accelerates the flat plate boundary layer. The rear part of the channel is composed by two independently adjustable straight endwalls. Thus, the variation of the pressure gradient is limited to the middle and rear parts of the plate, while the accelerating front part is kept constant. Note that both the test sections used in this work are equipped with optical accesses allowing measurements with Particle Image Velocimetry (PIV) and Laser Doppler Velocimetry (LDV) instrumentation. Moreover, the test section depicted in figure 3.4 is located in a constant-section airtight pressurised casing, thus avoiding external leakage due to the presence of the adjustable endwalls. The flat plate installed in the latest test section has been made longer and larger than the previous one in order to improve the maximum achievable spatial resolution. The second flat plate adopted in this work is 300 mm long and 300 mm wide in order to ensure 2D time-mean flow at mid-span (the condition of 2D flow at midspan was also ensured in the first test section considered). A 3:1 elliptic leading edge has been adopted to mitigate possible occurrence of leading edge separation that may introduce uncontrolled wave packets into the flat plate boundary layer, thus altering the transition process. Moreover, the adjustable endwalls can be set in non-symmetric positions to control the incidence angle on the leading edge of the flat plate, preventing the occurrence of BL separation on the top endwall of the test section. The setting and control of the proper angle of attack for the different conditions is surveyed by several pressure taps (17) on the top and the bottom sides of the leading edge. In the straight part of the plate, 51 pressure taps have been installed to provide the characterization of the pressure gradient imposed by the different endwall settings. The same pressure taps arrangement characterized the flat plate installed in the test section shown in figure 3.3. The pressure taps are then connected to the acquisition system by means of a scannivalve which allows the acquisition of the signals coming from all the pressure taps with a reduced number of pressure transducers.

3.2.1 Grids for turbulence generation

Turbulence intensity is one of the parameters that strongly affect the development of a boundary layer and its transition mode, as discussed in section 2.8. For this reason, a gradual variation of the free-stream turbulence intensity level has been considered in this work. To this end, turbulence generating grids have been installed upstream of both the test sections adopted to induced controlled levels of turbulence at the leading edge of the plate. Turbulence grids are locked in such a way that excessive vibrations are inhibited and do not produce fluctuations in the turbulence level generated.

As shown in figure 3.5, the grids are composed of a steel net made of bars with rectangular section. The net was created with a laser cutting machine. The most significant parameter defining the geometry of a grid is the ratio between the empty spaces between the bars and the overall surface of the mesh [52]. This parameter can be calculated as:

$$\beta = \left(1 - \frac{s}{m}\right)^2 \tag{3.1}$$

The values of β for the different grids adopted are reported in table 3.1 with their related values of turbulence. For the grids used in this work the height h is 300 mm, the width w

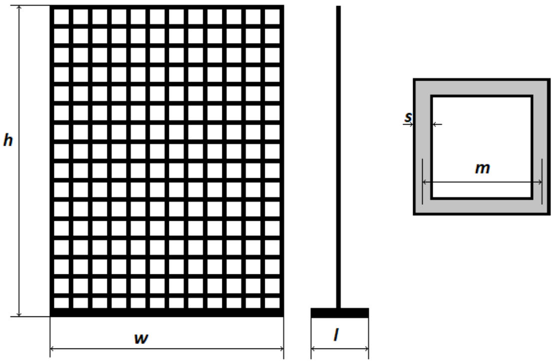

Fig. 3.5 Scheme of the turbulence generating grids installed in the test section.

Table 3.1 Geometries of the different turbulence grids adopted. Subscripts 1 and 2 refer to the two different test sections depicted in figure 3.3 and 3.4, respectively.

Grid	**s [mm]**	**m [mm]**	β **[-]**	**Turbulence level [%]**
NG_1	-	-	-	0.65
LTU_1	3	11	0.53	1.2
HTU_1	4	12	0.44	2.87
NG_2	-	-	-	1.5
LTU_2	2	10	0.64	2
HTU_2	4	12	0.44	2.8
$HHTU_2$	8	16	0.25	5

is 300 mm and the length l of the base measures 40 mm. The names of the grids reported in table 3.1 indicates the no-grid condition (NG), the low-Tu condition (LTU), the high-Tu condition (HTU) and the highest-Tu condition ($HHTU$). Subscripts 1 and 2 in table 3.1 refer to the two different test sections depicted in figure 3.3 and 3.4, respectively. Different Tu levels observed between the cases 1 and 2 are due to the variation of the grids geometry, jointly with the modification of the test section, and the operating point of the fan, which induce also the modification of the spontaneous turbulent of the channel (i.e. the no-grid conditions).

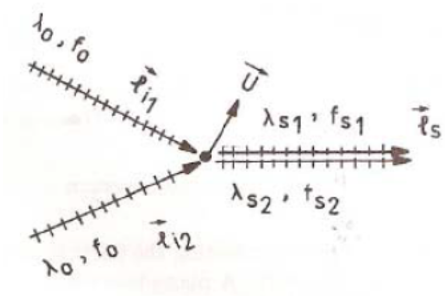

Fig. 3.6 Crossed beam scheme.

3.3 Measurement techniques

3.3.1 Laser Doppler Velocimetry

Laser anemometers are non-intrusive optical instruments for the investigation of fluid flow structures in gases and liquids. Their working principle is based on the laser light, which presents unique properties (constant wavelength above all) of spatial and temporal coherence, making possible to design an efficient optical anemometer. Application of laser velocimetry to a large variety of flows has been made since the technique exists. This instrument appeared immediately to be the answer to a wide variety of problems. Its capability of being not-intrusive is one of its main advantages, being capable of probing the flow with focused laser beams without disturbing the flow neither in the measuring volume nor in the portions of fluid crossed by the beams. LDV measurements require a transparent medium with a proper concentration of seeding particles. Optical access to the flow through a window is another necessary condition. The optics of the laser anemometer can define a minimal measuring volume and thus provides excellent spatial resolution and allows local measurement of velocity. The small measuring volume in combination with fast signal processing electronics also allows time-resolved measurements of fluctuating velocities. Note that the temporal resolution is usually limited by the concentration of seeding rather than the measuring equipment itself. Combinations of laser anemometer systems with component separation based on colour, polarisation or frequency shift allow one-, two- or three-components LDV systems to be combined in optical modules.

The optical setup designed to allow measurements in fluid flow is the crossed beam scheme, shown in figure 3.6. In this system two laser beams are illuminating the particles, each one with its frequency and wavelength f_0 and λ_0. The two scattered beams moving along the direction defined by the unit vector l_s have a frequency which is given by:

$$f_{s,1} = f_0 + \frac{u}{\lambda_0}(l_s - l_{i,1}) \tag{3.2}$$

and

$$f_{s,2} = f_0 + \frac{u}{\lambda_0}(l_s - l_{i,2}) \tag{3.3}$$

where l_i is the unit vector defining the propagation direction of the incoming beams. Combining the frequencies of both beams the Doppler frequency f_D is found as:

$$f_D = f_{s,1} - f_{s,2} = \frac{u}{\lambda_0}(l_{i,1} - l_{i,2}) \tag{3.4}$$

With this scheme, the detected frequency is no longer dependent on the direction of the scattering, and it is of the order of magnitude of the flow dynamics phenomena taking place in the observed fluid. The effectiveness of the dual beam mode can be analysed considering the "fringe" method. When two laser beams of equal intensity are crossing, the formation of interference fringes in the crossing region occurs following the constructing and destructive interference scheme, due to the superposition principle of waves. When the frequency of the light is the same for both beams, these fringes are stationary and create a region characterised by enlightened and dark zones (see figure 3.7). When a solid particle is passing through this region, it is crossing successively bright and dark fringes. The light will be scattered when a bright fringe is crossed, with a frequency depending on the velocity with which the particle is moving in a perpendicular direction to the fringes and the distance between fringes. A stationary observer such as a photo-detector receives information about the particle only when it is illuminated, passing over a bright fringe. The distance between bright fringes is a function of the wavelength of the laser and the angle Θ defined by the direction of the beams.

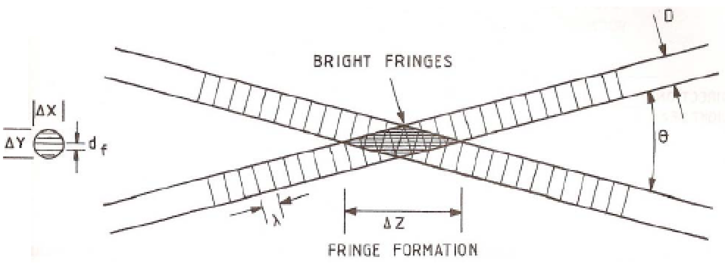

Fig. 3.7 The fringe model showing the interaction between two laser beams.

Referring to figure 3.7 the fringe spacing d_f results:

$$d_f = \frac{\lambda}{2sin\frac{\Theta}{2}} \tag{3.5}$$

hence, considering the distance between the bright fringes introduced above, the velocity can be measured as:

$$u_\perp = \frac{d_f}{\Delta t} = \frac{\lambda_0}{2\sin\frac{\Theta}{2}} \cdot f_D \tag{3.6}$$

where f_D is the Doppler frequency. The measured velocity component lays on the same plane of the two laser beams, but it is perpendicular to the bisector of the angle Θ between them. In order to detect two velocity components and to achieve a 2-D measurement, two couple of beams are required.

Thanks to its analytical transfer function the Laser Doppler Velocimetry is capable of giving exact results in a vast range of velocities without calibration. The only two sources of error in equation 3.6 are the angle between the beams, which can be measured with a negligible uncertainty, the wavelength of the laser, that is not affected by variations once the laser type is chosen and the error on the evaluation of the Doppler frequency, which depends on the frequency resolution adopted. The only source of uncertainty is therefore substantially related to the frequency resolution used for the evaluation of f_D.

In the present work, a four-beams Laser Doppler Velocimeter (Dantec Fiber Flow) was employed in a backwards scatter configuration for the velocity measurements of the vertical and horizontal velocity components. The light sources are two diode-pumped solid-state lasers with a power of 200 mW each. The two pairs of green and blue beams, employed to investigate the two velocity components, have respective wavelengths of 532 and 488 nm. The frequency of one of each pair of beams was shifted by 40 MHz with a Bragg cell. The probe consists of an optical transducer head of 60 mm diameter, with a focal length of 300 mm and a beam separation of 38 mm, connected to the emitting optics and the photomultipliers employing optic fibres, with a beam intersection angle of 7.4 °. The LDV head is mounted on a 3-axis traversing system numerically controlled. This allowed solving with great details the velocity profiles in the normal to the wall direction at different positions along the plate as well as the characterization of the velocity and rms of velocity fluctuations in the free-stream regions, as shown in section 5.

3.3.2 Particle Image Velocimetry

The Particle Image Velocimetry (PIV) is a non-intrusive, optical measurement technique capable of solving a vectorial map of a two-dimensional velocity field with a single acquisition. Using a PIV it is possible to gain an accurate and complete picture of the situation involving the flow, visualising velocity fluctuations and velocity profiles in the domain considered [24]. A PIV system is composed of:

- High power laser system;
- CCD camera;
- Synchronizer;
- PIV postprocessing calculator;

When using the PIV instrumentation, a pulsed light source provided by a laser through its optics is used to generate a thin light sheet necessary to illuminate a cross-section of the seeded flow field. With this technique the laser's coherence property is not a requirement for measurements, differently from the LDV system. PIV images need to be acquired using brief light pulse in order to fix a steady image of the particles, without streaking, making pulsed lasers the natural choice for PIV analysis. The most commonly used laser is the Nd:YAG laser, that emits infrared radiation at 1064 nm. When implemented in PIV applications, the wavelength is reduced to 532 nm, allowing for particle lightening and reflection in the visible spectrum with a green light. Each image requires to be singly exposed to obtain images suitable to the cross-correlation process. To do so, the laser must produce powerful impulses at a high frequency: to achieve a wide range of pulse separations, two separate laser cavities are used where the laser pulses features can be set depending on the exigency. These lasers, called dual lasers, are housed into a single module containing the elements shown in figure 3.8.

The generation of the laser sheet is usually entrusted to optics, with the objective of controlling both the spreading angle and the thickness of the light sheet involved in the measurements. Common ways to achieve a proper illumination include a variety of combinations of cylindrical and spherical lenses. A cylindrical lens is used to spread the beam into a sheet, while the distance between the following lenses, combined with their geometry and orientation, acts for the regulation and adjustment of the light sheet [24]. The camera which is part of the acquisition system is located perpendicularly to the light sheet, thus visualising the whole flow field. In addition, a synchronizer is used to impose the proper timing between the laser pulsing and the frame rate timing sequence of the camera, such

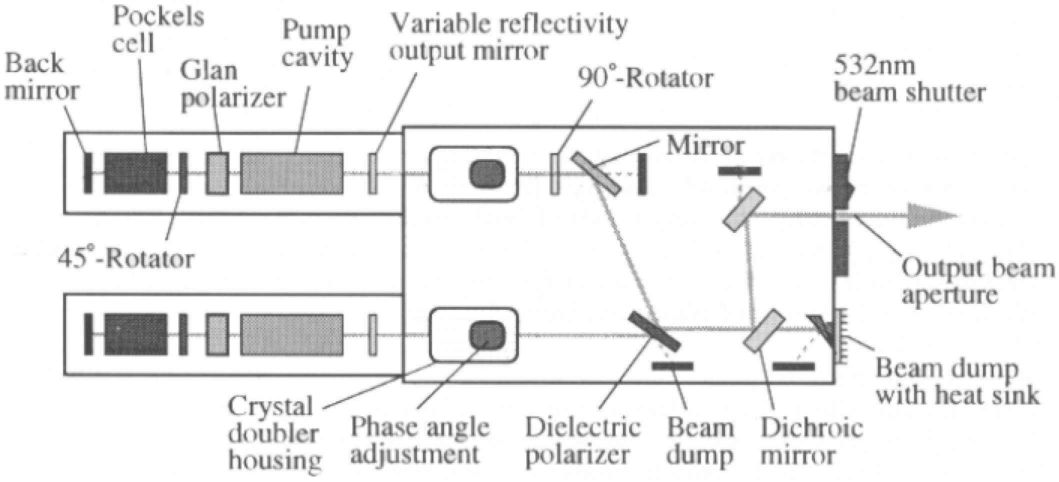

Fig. 3.8 Components of the dual laser single module commonly used in PIV applications.

that each image is singly exposed and the captured particles appear steady in each image. Cross-correlation cameras have become the preferred method of acquiring images. The cross-correlation cameras use high-performance CCD chips, which transforms the captured light immediately in a digital signal stored in the camera memory. Such chips include $m \times n$ light sensitive picture elements, corresponding to pixels, and an equal number of storage cells. The light of each pixel is evaluated in grey scale. The first laser pulse exposes the first frame, which is transferred from the light-sensitive cells to the storage cells immediately after the laser pulse. The storage cells now contain the first camera frame of the pair with information about the initial positions of seeding particles. The first image is transferred to the storage memory allocated inside of the CCD camera itself. The second laser pulse is then fired to expose the second frame and the light-sensitive pixels acquire the second image, which has information on the final positions of the seeding particles.

Particle images must be systematically processed to obtain a quantitative measure of the velocity field. For this reason, these recorded images are sampled using an interrogation region (see figure 3.9), the dimensions of which determine the spatial resolution. The interrogation regions can be adjacent to each other, or more commonly, have partial overlap with their neighbours to increase the spatial resolution. The shape of the interrogation regions is usually a square, but it can be customized while taking into account strong gradients in the velocity field (such as those occurring in boundary layers). The PIV velocity field is computed as the most likely displacement of a group of particles contained in each interrogation region. For a single pair of images, each interrogation region of the first image is compared with those of the second image of the same couple of images in order to determine the mean displacement of the particles of each interrogation region. This is made by means

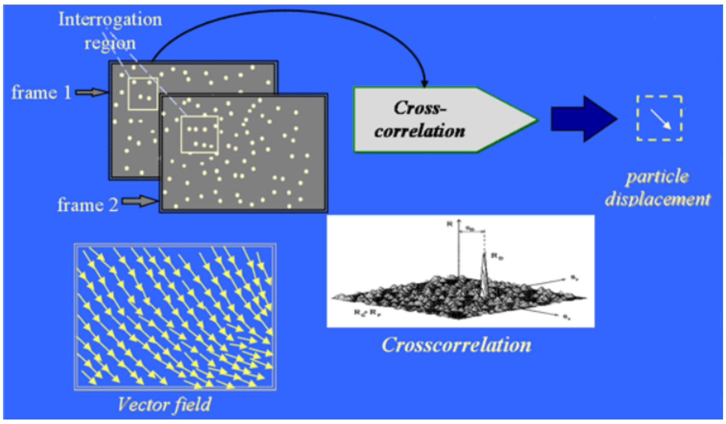

Fig. 3.9 Functional scheme of a Particle Image Velocimetry system

of the cross correlation between the two images of each acquired couple. To cross-correlate two PIV snapshots, the reference system has to be established. Once the (x,y) plane is set, the computer will perform its calculations considering the coordinates on the plane measured in pixels (m,n) and later transformed in meters considering the *magnification factor*, which takes into account the relation between the sensor scale and the real scale. For each interrogation region two functions are defined: $f_1(m,n)$ at time t and $f_2(m,n)$ at time $t+\Delta t$, where Δt is the time step between two laser pulses and both f_1 and f_2 are matrices in which each element has a value comprised between 0 and 1 related to their brightness in gray scales; dark pixels have the value of zero, while the bright saturated ones present the unity value. The probable mean displacement $\Delta x = (\delta x, \delta y)$ is calculated from the peak of the cross correlation function Φ:

$$\Phi = \int f_1(x+\Delta x)\cdot f_2(x)dx \tag{3.7}$$

which in its discrete formulation is

$$\Phi = \sum_m \sum_n f_1(m+i,n+j)\cdot f_2(m,n) \tag{3.8}$$

where i and j can vary from one to the number of pixels of the images. A peak in the cross-correlation function Φ occurs where a higher number of particles subjected to the same displacement in the first image finds correspondence with its counterpart in the second one. Subsequently, once the most probable displacement is known, its value is assigned to the interrogation region and becomes one of the vectors shown in the flow field after post-processing. The velocity related to the mean displacement of each window is then computed, keeping into account the scale factor between pixel coordinates and real dimensions of the flow field. To this end, a target has been designed and located inside the test section in order to measure the magnification factor for each acquisition. Once velocity vectors are calculated, a validation of the found value is required. Vectors are filtered both for their magnitude and for their direction since they have to be of a similar length of the surrounding ones and be compatible with the gradients given by other interrogation regions. When a vector is filtered out, it is usually substituted with a moving average centred in the same window.

In the present work, a fast response DANTEC time-resolved PIV system was adopted. The instrumentation is constituted by a dual-cavity Nd:YLF pulsed laser Litron LDY 300 with a maximum energy per pulse of 30 mJ at 1000 Hz repetition rate and 527 nm wavelength. The optical system forms a light sheet of 1 mm thickness. The light scattered by the vaseline oil droplets is recorded on a high-sensitive SpeedSense M340 digital camera with a cooled 2560 × 1600 pixels matrix. Further details on the measuring set and achieved uncertainties are provided in chapter 5 with reference to the particular results presented.

3.3.3 Seeding system

The seeding system is a necessary element for a correct working of non intrusive optical measurements, inserting seeding particles inside the flow moving in the wind tunnel and allowing the observation of the phenomena that develop in the test section. The seeders used for PIV and LDV measurements are composed of a tank containing the fluid to atomise, an atomiser, mechanical devices for the regulation of the dimension of the particles, an inlet for pressurised air and an outlet for the mixture of air and seeding. The air, pressurised by an external compressor enters the device from the inlet, thanks to a soft piping system. Here the pressure of air is commuted into velocity, and the atomization takes place thanks to the velocity gradient between the air and the seeding fluid. The mixture of air and small particles are collected at the outlet of the seeder and brought by a nozzle at the inlet of the wind tunnel, just downstream of the filter, such that a higher amount of particles is delivered to the downstream test section. Two seeders were used in parallel in order to obtain a proper seeding density both for PIV and for LDV measurements, where the data rate needed to be increased in the measuring point close to the wall of the flat plate.

Whenever a particle is carried by a fluid flow a difference between the velocity of the flow and the particle itself exists and a percentage variance can be defined as:

$$\varepsilon = \frac{u - u_p}{u} \tag{3.9}$$

Where u is the flow velocity and u_p is the velocity of the particle, that is a function of the density of the seeding fluid and the drag force carried out on the particle. Hence, to obtain precise results, it is to use a fluid that can be atomised in particles small enough to have a small value of ε but, at the same time, with a dimension capable of impressing the CCD camera of the PIV. In the present work vaseline oil droplets with a mean diameter of 1.5 μm were used, having the property of low density and hence dumping the inertial effects, with a consequent quick response to velocity variations of the flow.

Chapter 4

Data Processing

4.1 Boundary layer statistics

In order to obtained a statistical characterization of the time-mean response of the boundary layer to Re, Tu and APG variation, the main statistical properties of the boundary layer (i.e. time-mean velocity , rms of velocity fluctuations, and BL integral parameters) have been characterized in details for all the conditions tested. This allowed obtaining a quick view of the response of the transition process to the parameters variation, useful for guiding the modelling strategies (i.e. for the development of empirical correlations providing non-local terms appearing in closure equations used in RANS based CFD solvers). Particularly, the mean flow results in terms of time-averaged velocity fields and rms of velocity fluctuations, obtained by means of the PIV and LDV systems described in chapter 3, allowed the determination of the boundary layer growth, transition onset and amplification rate of velocity fluctuations as well as a detailed characterization of the BL response to the inflow conditions change in terms of mean velocity and rms profiles. Moreover, in case of separated flows the separation position has been identified by both the time mean velocity and the integral parameters distributions. More precisely, the distributions of the integral parameters computed for different Re and Tu levels are known to start to diverge downstream of the separation position due to the different time mean response of the separation bubble, while they are superimposed upstream of the transition location (see Lardeau et al. [56]). Additionally, the distributions of the displacement thickness δ^* and the shape factor H_{12} provide useful information to identify the bubble maximum displacement position and the transition onset location. On the other hand, the momentum thickness θ at separation is an important parameter appearing in most of the empirical correlations for the prediction of the transition length and onset (see chapter 2). For this reasons, the distributions of the main BL integral parameters (δ^*, θ and H_{12}) have been computed for all the flow conditions tested completing the analysis of the time-averaged velocity distributions and rms of velocity fluctuations.

To compute the distribution of δ^*, θ and H_{12}, the time-averaged velocity fields were obtained by a large number of instantaneous PIV snapshots in order to improve statistics (thousands of statistically independent snapshots are considered for each condition). Then, using an ad-hoc developed Matlab code, the boundary layer edge has been identified with a threshold on the local vorticity magnitude. More precisely, for each streamnwise location the BL edge has been identified as the point at which the relative normal variation of the time-mean streamwise velocity is equal to 0.01, according to the definition of δ_{99} reported in section 2.1. Since in the BL $\partial V/\partial x << \partial U/\partial y$, the spanwise vorticity ω_z can be approximated with the derivative $\partial U/\partial y$, which directly relates to the velocity variation in the y-direction due to the fixed spatial grid. Due to the large number of independent snapshots adopted for the computation of the time-mean velocity field, the spanwise vorticity was found to be almost null in the averaged field outside of the BL. Indeed, the random propagation of vortical structures generated by the turbulent grids are the unique source of spanwise vorticity in the channel near the BL edge. Data were spatially filtered in order to contain the error in the determination of the local free-stream velocity and its derivatives. While the local free-stream is necessary for the computation of the boundary layer integral parameters, the derivatives of the free-steam velocity are used for the computation of the acceleration parameters K and λ_θ, which are defined in chapter 2 and were adopted for the characterization of the velocity gradient imposed to the flow along the plate.

In figure 4.1 the distributions of the shape factor and the displacement thickness for a fixed APG and different Tu levels and Reynolds numbers are reported as an example of the effects of these two parameters on the bubble maximum displacement (peak of δ^*) and transition onset (peak of H_{12}) positions.

4.2 Proper Orthogonal Decomposition (POD)

Due to the large amount of data collected for each flow condition tested (thousands of PIV snapshots were acquired for each condition), a statistical reduction of the experimental database produced in this work was necessary in order to characterize the dynamic response of the BL to the variation of Re, Tu and APG. In this context, the Proper Orthogonal Decomposition is known to be a suitable tool for the characterization of the main dynamics occurring in a given data set composed of a large amount of observations (see e.g. Legrand [57]). When the POD is computed with reference to the temporal cross-correlation matrix [57], the POD eigenvectors (i.e. the temporal coefficients) provide the dynamic behaviour of the main coherent structures within the flow (ranked on the basis of their energy content),

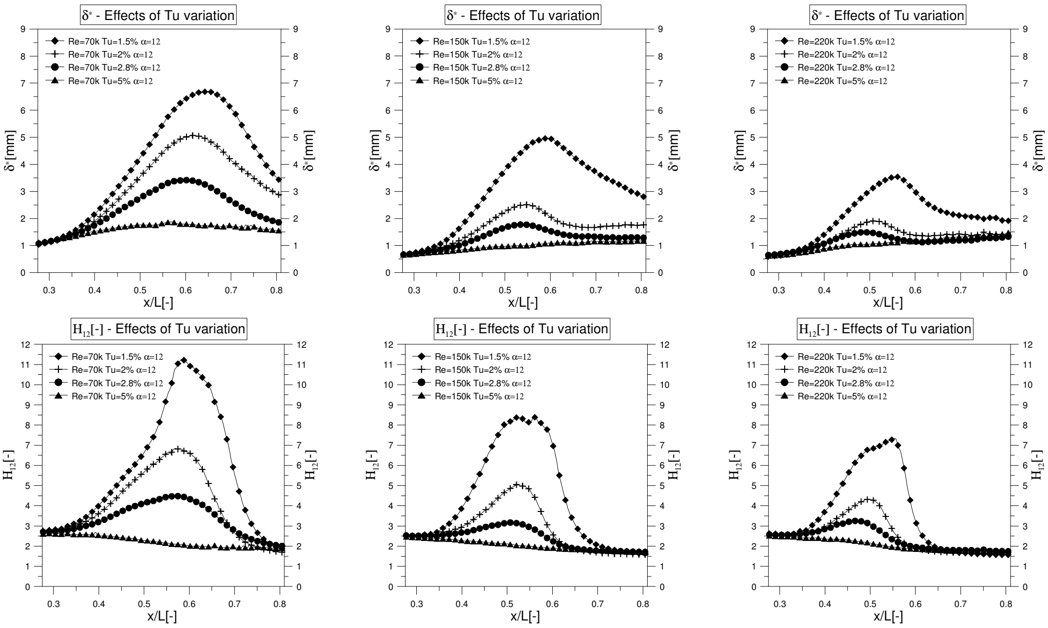

Fig. 4.1 Example of boundary layer integral parameters distribution obtained by PIV measuremets.

while their spatial distribution is obtained by the corresponding modes. In order to make the reader familiar with this decomposition technique, the main features of the POD procedure are reported in the following.

The POD was introduced in its original formulation by Lumley [69] for the analysis of turbulent flows, while the so-called *snapshot* POD, which is largely used for the detection of coherent structures in both experimentally and numerically derived fields, was subsequently introduced by Sirovich [110]. This modal decomposition technique is now largely understood and applied in different fields thanks to the works of several research groups (e.g., Glauser and George [34] and Ukeiley et al. [118]). As recently shown by Legrand et al. [58], this procedure may be also adopted to provide a temporal reconstruction of the flow from non-time resolved, statistically independent data. Although POD is usually adopted for the analysis of coherent structures in fluid flows, that is the modes are derived from the velocity field, the same procedure can be applied to any other quantity of interest which is space and time dependent (e.g., Borée [11]). The main feature of the POD procedure is that the modes obtained by the decomposition are ranked on the basis of their energy content relative to the energy of the fluctuating field in the whole domain considered. This means the the first modes are representative of the coherent structures with the highest energy within the flow. This is the main difference between the POD and the widely used discrete Fourier transform (DFT), which provides *frequency-ranked* modes. Moreover, due to the optimality of the POD procedure, a high percentage of the energy of the overall fluctuations is captured by the first few modes, allowing low rank representation of the flow with a small number of modes.

In order to introduce the mathematical framework constituting the basis of the classical POD introduced by Lumley [69] and the successive snapshot POD of Sirovich [110], let consider an ensemble of observations $u^i := u(\mathbf{x}, t^i)$ which are a function of both space and time (u^i denotes the fluctuating velocity of a given field at the time t^i). In the original approach of Lumley [69], the POD looks for the function $\Phi(\mathbf{x})$ that maximizes the normalized square projection of a given data set in a mean sense, i.e.:

$$\underset{\|\Phi(\mathbf{x})\|=1}{max} \frac{\left\langle \left| \left(u^i, \Phi(\mathbf{x})\right) \right|^2 \right\rangle}{\|\Phi(\mathbf{x})\|^2} \tag{4.1}$$

Here $\langle . \rangle$ denotes the ensemble average, while (,) and $\|.\|$ indicate the L^2 inner product and norm, given as:

$$\left(u^i(\mathbf{x}), \Phi(\mathbf{x})\right) := \int u^i(\mathbf{x}) \cdot \Phi^*(\mathbf{x}) d\mathbf{x} \qquad \|\Phi(\mathbf{x})\| := \sqrt{(\Phi(\mathbf{x}), \Phi(\mathbf{x}))} \tag{4.2}$$

where * denotes the conjugate complex. Using the calculus of variations the function $\Phi(\mathbf{x})$ can be shown to provide a solution for the following Fredholm's equation:

$$\int_\Omega R(\mathbf{x}, \mathbf{x}') \cdot \Phi^*(\mathbf{x}') d\mathbf{x}' = \lambda \Phi(\mathbf{x}) \tag{4.3}$$

where Ω is the spatial domain of interest, λ is the Lagrange multiplier, and $R(\mathbf{x}, \mathbf{x}')$ is the ensemble averaged two-points spatial correlation tensor, defined as:

$$R(\mathbf{x}, \mathbf{x}') := \left\langle u^i(\mathbf{x}) \otimes u^i(\mathbf{x}') \right\rangle \tag{4.4}$$

where $\otimes$ is the dyadic product. In the classical approach of Lumley [69], the eigenfunctions $\Phi(\mathbf{x})$ of the correlation tensor $R(\mathbf{x}, \mathbf{x}')$ constitute the POD spatial modes, while the related temporal coefficients are obtained by projection. Note that, since $R(\mathbf{x}, \mathbf{x}')$ is a self adjoint and non-negative operator, the POD modes $\Phi(\mathbf{x})$ are implicitly orthogonal, which is a suitable feature for reduced order models construction.

The successive snapshot POD was introduced by Sirovich [110] to reduce the computational requirements of the classical POD calculations. Starting from the formulation of Lumley, Sirovich derived a discrete eigenvalue problem for the correlation matrix C defined as:

$$C^{ik} := \frac{1}{N_t}(u^i(\mathbf{x}), u^k(\mathbf{x})) \tag{4.5}$$

where N_t is the number of observations. From the procedure point of view, all the PIV snapshots collected for a given condition have been ordered in a matrix U, whose columns contain all the instantaneous acquisitions, that is, the matrix U sizes $N_p \times N_t$, where N_p is the number of spatial positions considered. In this way, equation (4.5) can therefore be rewritten in a matrix form as:

$$C := \frac{1}{N_t}U^T U \tag{4.6}$$

Note that since C is a real symmetric positive-definite matrix, its eigenvalues are real and non-negative and are sorted according to $\lambda_1 \geq \lambda_2 \geq \ldots \geq \lambda_m$. Each eigenvalue is representative of the energy associated to the corresponding mode. The related eigenvectors $\chi_m = [\chi_m^1, \ldots, \chi_m^{N_t}]$ provide a complete orthogonal basis and are obtained from the following eigenvalue problem:

$$C\chi_m = \lambda_m \chi_m \qquad m = 1, \ldots, N_t \tag{4.7}$$

In the snapshot POD the temporal coefficients are therefore obtained from the eigenvectors of the correlation matrix C, and the POD modes are computed as a linear combination of the observations:

$$\Phi_m(\mathbf{x}) = \frac{1}{\sqrt{N_t}} \sum_{i=1}^{N_t} \chi_m^i u^i(\mathbf{x}) \tag{4.8}$$

The POD modes $\Phi_m(\mathbf{x})$ obtained from the (4.8) also provide a complete orthogonal basis and they still satisfy equation (4.3).

4.3 Weighted Proper Orthogonal Decomposition (WPOD)

In the present work, a new POD based procedure was developed with the aim of emphasizing the coexistence and the possible interaction between structures with different energy magnitude, also providing their frequency content. The need for a variation of the POD procedure arises from the energy based ranking of the classical POD approach, which implies that structures with different energy content are captured by different modes, thus preventing the characterization of their interactions, if any. The proposed method is based on two different and subsequent steps. First, spatial and temporal weighting matrices are introduced in the maximization problem constituting the initial step of the classical POD procedure (equation 4.1). This is to increase the homogeneity of the data ensemble in terms of the energy of velocity fluctuations captured by all the observations of the flow. More precisely, the spatial weighting matrix makes structures characterized by sensibly different kinetic energy that can appear in the same snapshot (i.e. BL streaks and free-stream vortices), more comparable in terms of energy. This allows these structures to be captured by the same mode, showing their coexistence. On the other hand, the temporal weighting matrix acts normalizing in time the velocity fluctuations at a fixed position, increasing the statistical stationarity of the data ensemble. Note that depending on the definition of the weighting matrices, different homogenisation are produced on the data ensemble. Then, after the modes are computed in a similar way to the classical procedure described in the previous section, the WPOD modes are further decomposed as a combination of Fourier transforms of the WPOD temporal coefficients and velocity maps, thus highlighting the coexistence of structures with different energy and also frequency content. This is something similar to what applied by Glauser et al. [34], Arndt et al. [9] and Liu and Adrian [67] in homogeneous spatial directions. In this section, the mathematical framework of the proposed method is presented comparing it to the classical *snapshot* POD of Sirovich [110].

First, it can be shown that the vectors χ that are solution to equation (4.7) can be also obtained by solving the constrained optimization problem (4.9):

$$\max_{\|\chi\|=1} \frac{\|U\chi\|^2}{\|\chi\|^2} \tag{4.9}$$

where U is the matrix containing the N_t realizations of the field such that $UU^T = C$ (i.e. the correlation matrix), as previously introduced. More precisely, the vector χ obtained from the (4.9) maximizes the square projection on the observations in a mean sense. In the present method we introduce weighted scalar products and norms in equation (4.9) obtaining a new maximization problem

$$\max_{\|\chi_w\|_{W_T}=1} \frac{\left\|(U\chi_w)_{W_T}\right\|^2_{W_S}}{\|\chi_w\|^2_{W_T}} \tag{4.10}$$

where two weighting matrices (called W_T and W_S) are used to define the following inner products and norms:

$$(U\chi_w)_{W_T} = (UW_T\chi_w) \tag{4.11}$$

$$\left\|(U\chi_w)_{W_T}\right\|^2_{W_S} = (U\chi_w)^T_{W_T}\, W_S\, (U\chi_w)_{W_T} \tag{4.12}$$

$$\|\chi_w\|^2_{W_T} = \chi_w^T W_T \chi_w \tag{4.13}$$

The weighting matrix W_T is a real diagonal matrix (sizing N_t) whose entries are the reciprocal of the spatial rms of velocity fluctuations of each observation (N_p is the number of spatial points):

$$W_T^{ik} = \begin{cases} \left[\frac{1}{N_p}\sum_{p=1}^{N_p} u(\mathbf{x}_p, t_i)^2\right]^{-0.5} & \text{for } i = k \\ 0 & \text{for } i \neq k \end{cases} \tag{4.14}$$

similarly, W_S is a real diagonal matrix (sizing N_p) whose entries are the reciprocal of the temporal rms of velocity fluctuations at each position:

$$W_S^{ik} = \begin{cases} \left[\frac{1}{N_t}\sum_{p=1}^{N_t} u(\mathbf{x}_i, t_p)^2\right]^{-0.5} & \text{for } i = k \\ 0 & \text{for } i \neq k \end{cases} \tag{4.15}$$

From a physical viewpoint, W_T acts normalizing the energy content of the instantaneous velocity fields, while W_S increase the spatial homogeneity of each PIV snapshot in term of energy. This allows emphasizing events characterized by low kinetic energy (e.g. free-stream vortices) that can play a crucial role in the dynamics of coherent structures captured by the most energetic POD modes.

Now using the calculus of variations, the functions χ_w being a solution for equation (4.10) are conveniently obtained from the solution of the following eigenvalue problem

$$C_W \chi_{w_m} = \lambda_m \chi_{w_m} \qquad m = 1, \ldots, N_t \tag{4.16}$$

where C_W is the new defined weighted correlation matrix:

$$C_W^{ik} := \frac{1}{N_t}(u^i(\mathbf{x}), u^k(\mathbf{x}))_{W_S} W_T^{ii} \tag{4.17}$$

The weighting matrix W_T can be also used to blank spatial positions characterized by extremely low kinetic energy, that otherwise may be responsible for numerical instability in the computation of the cross-correlation matrix. According to the snapshot POD approach, the weighted modes $\Phi_{w_m}(\mathbf{x})$ are obtained by projection of the snapshot fluctuations on the eigenvectors χ_{w_m}:

$$\Phi_{w_m}(\mathbf{x}) = \frac{1}{\sqrt{N_t}} \sum_{i=1}^{N_t} u^i\, W_T^{ii}\, \chi_{w_m}^i \tag{4.18}$$

It should be noted that since the new defined correlation matrix C_W is not symmetric, both the eigenvectors χ_{w_n} and the corresponding modes $\Phi_{w_n}(\mathbf{x})$ do not provide an orthogonal basis for the Hilbert space L^2. More precisely, right multiplying by W_T in the (4.17) forces the eigenvectors of C_W to be pairwise orthogonal with respect to this weighting matrix, i.e.:

$$(\chi_{w_n}, \chi_{w_m})_{W_T} = \delta_{nm} \tag{4.19}$$

while the modes are orthogonal with respect to the weighting matrix W_S:

$$(\Phi_{w_n}(\mathbf{x}), \Phi_{w_m}(\mathbf{x}))_{W_S} = \delta_{nm} \tag{4.20}$$

The non-orthogonality of the WPOD temporal coefficients implies that the contributions of the modes to the energy of the reconstructed fields are not independent to each others, since modal interaction exists. Moreover, the energy of the modes is redistributed with respect to the snapshot POD, even though the total kinetic energy (TKE) of the data set is still preserved by the decomposition. The optimality and orthogonality characteristics of the present method will be discussed in detail in section 5.3 where the application of this new technique to experimental data will be presented.

4.4 Mixed Fourier-Empirical decomposition

A further Fourier-based decomposition of the modes obtained by the weighted POD procedure was considered in order to allow the identification of the frequency content of the structures captured by the modes, as well as to highlight the coexistence of structures characterized by different frequency content. More precisely, the WPOD modes are obtained from the combination of the Fourier transforms of the normalized data ensemble with the Fourier transforms of the WPOD eigenvectors as coefficients (see for instance Citriniti et al. [20] and Liu and Adrian [67]).

$$\Phi_{w_m} = \frac{1}{\sqrt{N_t}} \sum_{i=1}^{N_t} u^i W_T^{ii} \chi_{w_m}^i = \frac{1}{\sqrt{N_t}} \sum_{i=1}^{N_t} u_w^i \chi_{w_m}^i \tag{4.21}$$

$$= \frac{1}{\sqrt{N_t}} \sum_{i=1}^{N_t} \sum_{n=1}^{N_t} \widehat{u}_w^n \exp\left(j\omega_n t_i\right) \chi_{w_m}^i \tag{4.22}$$

$$= \frac{1}{\sqrt{N_t}} \sum_{n=1}^{N_t} \widehat{u}_w^n \sum_{i=1}^{N_t} \chi_{w_m}^i \exp\left(j\omega_n t_i\right) \tag{4.23}$$

$$= \frac{1}{\sqrt{N_t}} \sum_{n=1}^{N_t} \widehat{u}_w^n \widehat{\chi}_{w_m}^{n*} \tag{4.24}$$

Here t_i is the discrete time instant, ω_n is the angular frequency and * denotes complex conjugate. Equation (4.24) makes evident that each WPOD mode can be obtained as a combination of orthogonal functions which directly provides the *pure sinusoidal* content of each dynamics and related temporal coefficients. Note that the energy of each mode is preserved if the whole spectrum is considered for the mode reconstruction. The capability of this technique to further highlight and isolate structures that are not directly observed in the WPOD modes will be further pointed out in section 5.3.

Chapter 5

Results and Discussion

5.1 Inspection of the dynamic properties of laminar separation bubbles: free-stream turbulence intensity effects for different Reynolds numbers

In this section the effects of free-stream turbulence intensity on the transition process of a pressure induced laminar separation bubble are analyzed for different Reynolds numbers. Measurements were carried out under fixed APG typical of high-lift blade profiles in the test section depicted in figure 3.3 by means of time-resolved (TR) PIV (see section 3.3.2). A test matrix spanning 3 Tu levels and 3 Reynolds numbers has been considered, allowing the estimation of cross effects of these parameters on the instability mechanisms driving the separated flow transition process. Boundary layer integral parameters, spatial growth rate and saturation level of velocity fluctuations are discussed for the different cases in order to characterize the base flow response as well as the time-mean properties of the Kelvin-Helmholtz instability. The inspection of the instantaneous velocity vector maps highlights the dynamics of the large scale structures shed near the bubble maximum displacement, as well as the low frequency motion of the fore part of the separated shear layer. Proper Orthogonal Decomposition has been implemented to reduce the large amount of data for each condition allowing a rapid evaluation of the group velocity, spatial wavelength and dominant frequency of the vortex shedding process. The dimensionless shedding wave number parameter makes evident that the modification of the shear layer thickness at separation due to Reynolds number variation mainly drives the length scale of the roll-up vortices, while higher Tu levels force the onset of the shedding phenomenon to occur upstream due to the higher velocity fluctuations penetrating into the separating boundary layer.

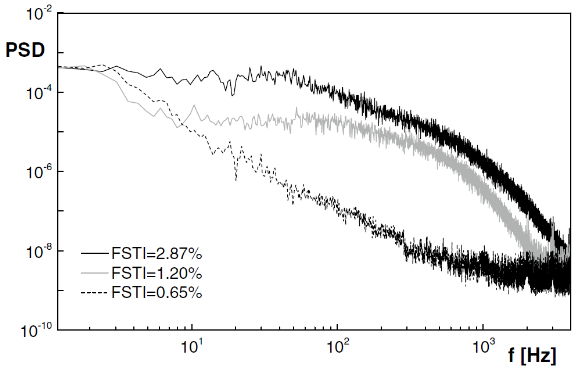

Fig. 5.1 Spectra of instantaneous velocity measured with hot-wire instrumentation in inlet free-stream for three different turbulence intensity levels.

5.1.1 Measurement techniques

The experimental apparatus and test section adopted are described in chapter 3. In this case, the test section shown in figure 3.3 was adopted, which did not allow the variation of the pressure gradient imposed to the flow. Measurements have been performed in the midspan plane of the flat plate reported in figure 3.3 for three Reynolds numbers and three Tu levels. The tested Reynolds numbers were 40000, 75000 and 90000, and the Tu levels at the plate leading edge were 0.65, 1.2 and 2.87%. These values were obtained integrating the turbulence spectrum (from f = 0.61 Hz to f = 20000 Hz) and normalizing by the mean velocity. The minimum value of Tu is due to the spontaneous turbulence of the tunnel, while two different turbulence generating grids have been used for the other conditions (see table 3.1). Thus, an experimental data set of nine different conditions, representative of aero-engine turbine operation, constitute the overall test matrix. The Fourier transform of the velocity measured with hot-wire instrumentation allowed the free-stream turbulence characterization at the measuring domain inlet: spectra relative to the two turbulence generation grids and the no-grid condition are reported in figure 5.1 . The higher the Tu the higher the energy content at the highest frequencies, whereas spectra are similar in the low-frequency range. In order to in depth analyze the dynamics of the laminar separation bubble, the DANTEC time-resolved PIV system described in chapter 3 has been adopted. The magnification factor for the present experiments was set to 0.184. This provides a particle image diameter of the order of 2–3 pixels and a particle image density of around 0.02–0.03 particles per pixel. The DANTEC FlowMap tool has been used for the cross-correlation of each image pair. The adaptive cross-correlation algorithm has been used with a finer interrogation area of 16 × 16 pixels and 50% overlap. This gives a distance between adjacent vectors of 0.43 mm. This measuring grid allows solving in great detail the velocity oscillations in the shear layer as well as the large-scale structures shed by the laminar separation bubble. A peak validation has been used to discriminate between valid and invalid vectors. With these settings, a Gaussian fitting procedure is likely to guarantee a subpixel recognition accuracy of particle displacement of the order of 0.1 pixel, according with the accuracy analysis reported in Sciacchitano et al. [102] and Wieneke [127]. Limiting the maximum particle displacement to 1/4 of the interrogation area the relative error in the evaluation of the instantaneous velocities is less than $\pm 3.0\%$ of the maximum measurable value. This ensures a relative error in the computation of statistical moments smaller than about 5% in the flow regions characterized by velocity equal or higher than half of the maximum measurable one, as it occurs in the separated shear layer (main area of interest) and in the attached boundary layer downstream of the laminar separation bubble. For each condition of the 3×3 PIV test matrix two time sequences, each of them consisting of 3100 instantaneous PIV snapshots, have been acquired at high sampling frequency (3168 Hz), which is at least ten times the vortex shedding frequency measured in the worst condition (high Reynolds number). One additional time sequence consisting of 3893 snapshots has been acquired for each tested condition at a significantly smaller sampling frequency (485 Hz). High- and low-frequency acquisitions allow better analyzing phenomena characterized by significantly different frequencies and speeds of propagation. High acquisition frequency improves spectral and modal analysis, whereas low acquisition frequency allows a better definition of the oscillations characterizing the separated shear layer as well as a better statistical treatment of the data.

5.1.2 Time-mean boundary layer characterization

The distributions of the dimensionless mean velocity $\overline{u}/U_0$ and of the rms of velocity fluctuations u'_{rms}/U_0 are shown in figure 5.2 for $Re = 40000$ and $Tu = 0.65\%$ as a reference condition. Coordinates *(x,y)* in the streamwise and the normal to the wall directions are normalized by the length of the plate L. The distributions of $\overline{u}/U_0$ and u'_{rms}/U_0 clearly show the occurrence of a laminar separation bubble. The boundary layer separates at about $x/L = 0.39$, while the abscissa corresponding to the bubble maximum displacement (i.e. to the maximum displacement thickness) is about $x/L = 0.69$. The separation position has been identified through extrapolation of the zero velocity streamline toward the wall and, due to the distance of the first measuring point from the wall, the accuracy is of the order of $\pm 0.01x/L$. Since the reverse flow magnitude is smaller than 15%, a convective inviscid instability process is expected to drive the amplification of disturbances along the separated shear layer, according to Alam and Sandham [4] and Michelassi et al. [84]. Maximum values of u'_{rms}/U_0 are localized inside the separated shear layer, along the velocity profile inflection line (black dashed line in the plots), reaching the highest peak in the flow region just downstream of the

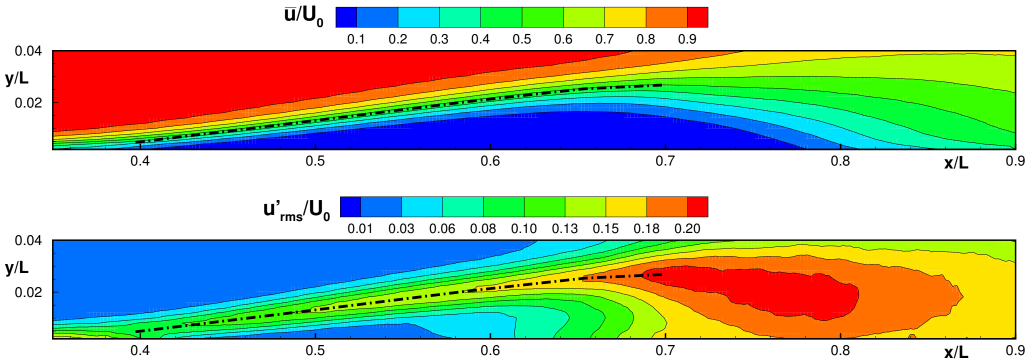

Fig. 5.2 Mean streamwise velocity $\bar{u}$ and rms of velocity fluctuations u'_{rms} normalized by free-stream velocity at measuring domain inlet U_0 for $Re = 40000 - Tu = 0.65\%$. Inflection line ($\partial^2\bar{u}/\partial y^2 = 0$) is drawn with black dashed line.

bubble maximum displacement position. This behavior is consistent with previous literature results (see Yang and Voke [128] for example). Moreover, a further peak can be observed in the wall region in the rear part of the separated shear layer (downstream of $x/L = 0.63$), as also observed in Watmuff [123].

To give an overall view of the Tu level effects on the time-mean structure of the bubble for the different Reynolds numbers tested, contour plots of $\bar{u}/U_0$ and u'_{rms}/U_0 for $40000 \leq Re \leq 90000$ and $0.65\% \leq Tu \leq 2.87\%$ are shown in figure 5.3 and figure 5.4, respectively (plots are stretched in the normal to the wall direction for clarity of presentation). The effects due to Reynolds number variation can be observed moving from top to bottom, while turbulence intensity varies from left to right. The separated flow region observed at $Re = 40000$ and $Tu = 0.65\%$ (top-left corner) reduces with increasing Reynolds number and Tu, according to Volino [120] and Yaras [129]. Particularly, it becomes so thin (or vanish) at the highest Reynolds number and Tu level that cannot be directly recognized in the plot. Thus, due to the lack of resolution, the condition $Re = 90000 - Tu = 2.87\%$ will not be further characterized in the following.

In order to better highlight the effects of these two parameters on the pressure distribution and the bubble topology (i.e. long or short according to the definition of Gaster [33]), the isentropic pressure coefficient distribution $C_p = (\bar{u}/\bar{u}_{ex})^2$ ($\bar{u}$ is the local edge velocity, while $\bar{u}_{ex}$ is the time-mean velocity at the exit plane) is plotted in figure 5.5 for the four extreme test conditions of the data set. The case $Re = 90000 - Tu = 2.87\%$ provides the reference pressure distribution, since it does not show any flex typical of separation occurrence (as shown by Gaster [33] and Volino [120] for example). Comparison with the reference distribution allows the computation of the Gaster's parameter $P = (\theta_s/\nu)(\Delta U/\Delta x)$ for the other cases. Here θ_s is the momentum thickness at separation; ν is the kinematic viscosity of the flow; ΔU

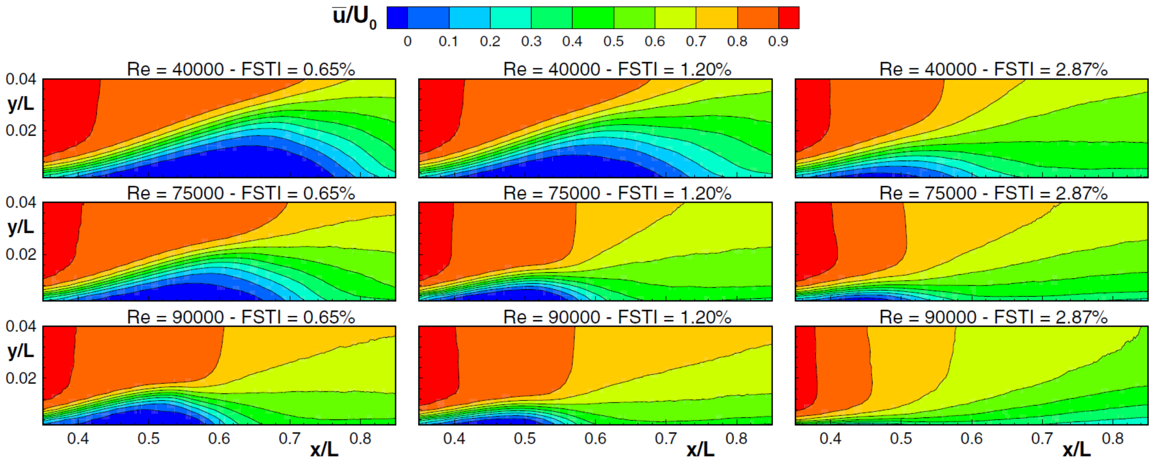

Fig. 5.3 Mean streamwise velocity normalized by free-stream velocity at measuring domain inlet $\overline{u}/U_0$ for different Tu levels and Reynolds numbers.

is the velocity rise over the bubble length Δx determined by comparison with the reference condition (see figure 5.5 for the case $Re = 90000 - Tu = 0.65\%$). The threshold $P = 0.24$ is commonly adopted to discriminate between long and short bubble configurations. The absolute value of the Gaster's parameter has been found to be equal to 0.19, 0.25 and 0.24 for the cases $Re = 40000 - Tu = 0.65\%$, $Re = 40000 - Tu = 2.87\%$ and $Re = 90000 - Tu = 0.65\%$, respectively. For the case $Re = 40000 - Tu = 0.65\%$ the occurrence of a long bubble type is confirmed by the marked change in the pressure coefficient distribution upstream of the separation position. In the other conditions the short bubble configuration is confirmed by the small local effects on the curves near the separation position. Consequently, the experimental results discussed here concern both long and short bubble types.

The effects induced by the Tu and the Reynolds number variation will be discussed with reference to the case $Re = 40000 - Tu = 0.65\%$ by increasing the turbulence level to Tu=2.87% and the Reynolds number to Re=90000 independently. Cross effects can be visualized in figure 5.3 and figure 5.4 and they will be presented in tables in the following. The discussion will be mainly focused on the effects of these two parameters on the base flow variation and on the propagation of velocity oscillations inside the separated shear layer.

No variation of the separation position exceeding the accuracy has been detected. For all cases the separation occurs in the surround of $x/L = 0.39(\pm 0.01)$. Conversely, both the bubble maximum displacement and the reattachment positions move significantly upstream with increasing Tu and Reynolds number, according to previous literature works (e.g. Volino [120] and Yaras [129]). Thus, the higher the value of these two parameters the shorter the laminar separation bubble and the smaller the bubble maximum displacement, as also shown by Ol et al. [89].

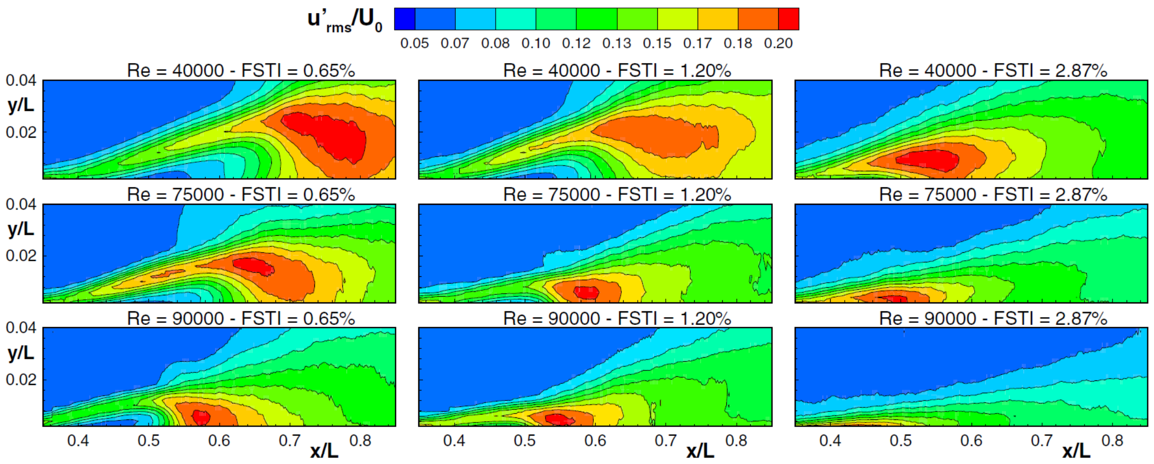

Fig. 5.4 Rms of streamwise velocity fluctuations normalized by free-stream velocity at measuring domain inlet u'_{rms}/U_0 for different Tu levels and Reynolds numbers.

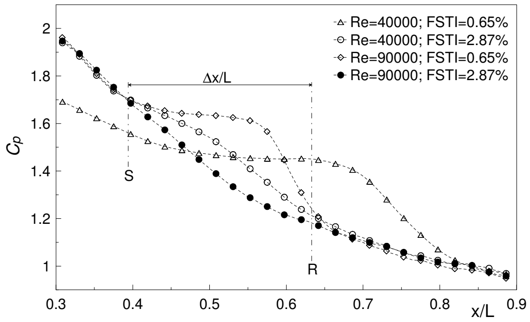

Fig. 5.5 Pressure coefficient (C_p) distributions for extreme conditions of data set. An example of estimation of streamwise length appearing in Gaster's parameter is also shown for $Re = 90000 - Tu = 0.65\%$; time-mean separation (S) and reattachment (R) positions are indicated for the same condition.

To synthesize Tu and Reynolds number effects on the time-mean properties of the bubble, the boundary layer displacement thickness δ^* and the shape factor H_{12} have been calculated (the boundary layer edge has been determined by way of a minimum-vorticity threshold). Results are plotted in figure 5.6 between $x/L = 0.35$ and $x/L = 0.8$, range including the separation region.

At the measuring domain inlet $(x/L = 0.3)$ the shape factor collapses for the different cases to the value typical of a laminar state $(H_{12} \approx 2.5)$. For the case $Re = 90000 - Tu = 2.87\%$ H_{12} reduces continuously to the value typical of a fully developed turbulent boundary layer $(H_{12} \approx 1.5)$ at $x/L = 0.65$. For the other cases the curves start diverging downstream of the separation.

At the separation point δ^* is affected by Reynolds number, but does not vary significantly

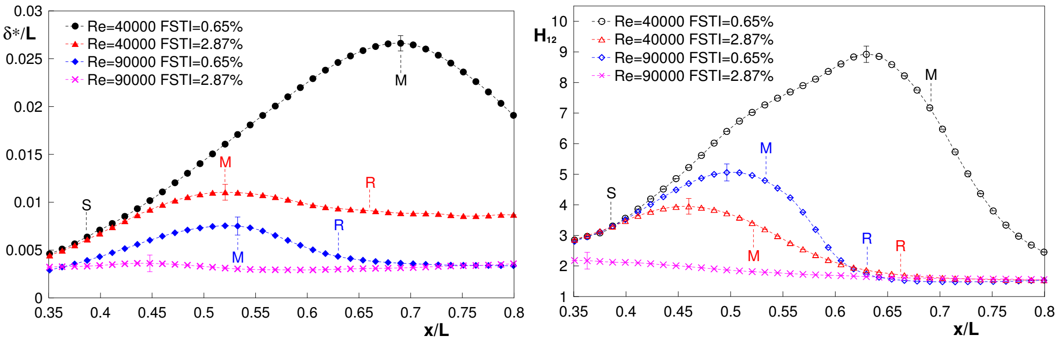

Fig. 5.6 Streamwise variation of (left) dimensionless displacement thickness δ^*/L and (right) shape factor H_{12} with error bars at the maximum values. Time-mean separation (S), maximum displacement (M) and reattachment (R) positions are indicated into the plots.

for different Tu levels at constant Reynolds number. Moreover, the higher the Tu level and the Reynolds number the lower the displacement thickness downstream of separation, according to Lardeau et al. [56]. As the curves of δ^* diverge, the shape factor H_{12} grows faster for lower Tu levels. Graphs of displacement thickness δ^* show the peak at the abscissa corresponding to the bubble maximum displacement positions, whereas the maximum of the shape factor H_{12} occurs upstream and may be attributed to the onset of transition (see Sarkar [96]). Table 5.1 summarizes the positions of maximum H_{12} and δ^* for the different cases, confirming that the distribution of H_{12} always peaks upstream of the maximum δ^* position, with a shift that appears to be affected by the Tu level for each Reynolds number tested.

In order to statistically characterize the evolution of velocity fluctuations along the separated shear layer, the streamwise distributions of the maximum u'_{rms}/U_0 and v'_{rms}/U_0 are shown in figure 5.7, where the ordinates are plotted in logarithmic scale (as previously stated, the case $Re = 90000 - Tu = 2.87\%$ is not discussed). A straight line in the plots indicates an exponential amplification of disturbances. The maximum of u'_{rms}/U_0 assumes relatively high values already from the measuring domain inlet, where a transient linear growth characterizes the disturbances evolution. Importantly, the higher the Tu level the higher the values of velocity fluctuations affecting the separating shear layer, while the Reynolds number variation only marginally affects the velocity fluctuations observed at the separation position. The

Tu	0.65%	1.20%	2.87%
$Re = 40000$	0.64	0.54	0.46
$Re = 75000$	0.56	0.49	0.43
$Re = 90000$	0.50	0.46	-

Tu	0.65%	1.20%	2.87%
$Re = 40000$	0.69	0.64	0.52
$Re = 75000$	0.61	0.50	0.47
$Re = 90000$	0.53	0.48	-

Table 5.1 Maximum H_{12} (left) and δ^* (right) positions (x/L) for different Tu levels and Reynolds numbers.

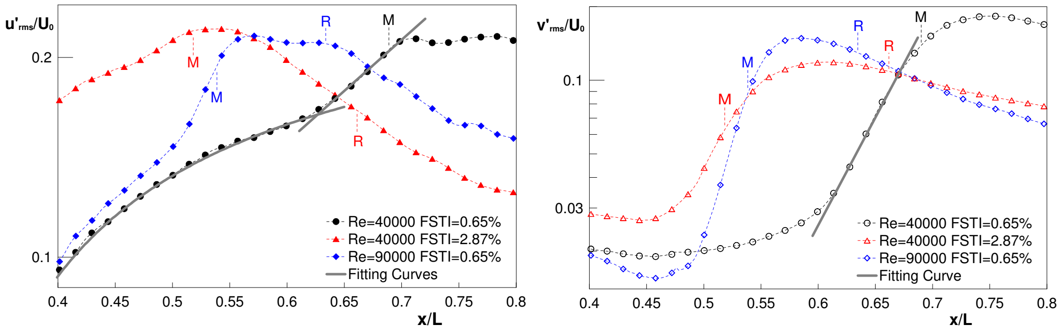

Fig. 5.7 Streamwise variation of maximum u'_{rms}/U_0 (left) and v'_{rms}/U_0 (right). Time-mean separation (S), maximum displacement (M) and reattachment (R) positions are indicated into the plots. Transient and exponential growth rates are highlighted for the condition $Re = 40000 - Tu = 0.65\%$.

maximum of v'_{rms}/U_0 is instead very low in the fore part of the laminar separation bubble and exhibits a marked (exponential) growth only well behind the separation position. The beginning of the exponential amplification of the v'_{rms}/U_0 corresponds to the position where the u'_{rms}/U_0 exhibits a clear change in the amplification process from transient to exponential. This condition evidently shifts upstream increasing the Tu level and Reynolds number. Then, both maxima of u'_{rms}/U_0 and v'_{rms}/U_0 grow exponentially up to reach the saturation level close to the bubble maximum displacement.

The different growth rates measured in the fore and the rear parts of the separated shear layer show analogies with the different amplification observed by MArxen et al. [77]: the transient amplification in the fore part of the bubble, attributed to spanwise waves, is substituted by an exponential behavior in the rear part of it, typical of the K-H instability mechanism. Moreover, the u'_{rms}/U_0 level measured where the growth rate changes from transient to exponential ($15\% - 18\%$) is very closed to the threshold of 20% reported in Zaki [132] for the breakup of streaky structures. Results shown in figure 5.7 suggest that different kind of instability processes may affect the fore part of the bubble and further investigations are required in order to shed light on these phenomena.

The mean spatial growth rates have been measured in the exponential growth regions referring to the v'_{rms}. According to Sarmast et al. [97] the spatial growth rate ς can be defined as:

$$\varsigma = \frac{\ln(v'_{rms}/U_0)_{sat} - \ln(v'_{rms}/U_0)_0}{(x/L)_{sat} - (x/L)_0} \tag{5.1}$$

where subscripts “0” and “*sat*” refer to the abscissas corresponding to the exponential amplification onset and saturation, respectively (results are reported in Table 5.2 with an uncertainty of $\varepsilon_\varsigma = \pm 0.2$). Note that no filtering criteria as those applied in Simoni et al.

Tu	0.65%	1.20%	2.87%
$Re = 40000$	7.9	7.5	7.4
$Re = 75000$	9.2	9.1	9.2
$Re = 90000$	15.8	15.2	-

Table 5.2 Mean spatial growth rate ς of v'_{rms}/U_0 for different Tu levels and Reynolds numbers.

[109] has been used to determine the spatial growth rate.

Data show that the spatial growth rate of the v'_{rms}/U_0 is marginally affected by the Tu variation for each Reynolds number. Conversely, the growth rate has been found to be strongly affected by the Reynolds number variation at fixed Tu level. The higher the Reynolds number the higher the exponential growth, as also observed in Dovgal et al. [29] and Yarusevych et al. [130]. The growth rate seems to significantly change only once the base flow before separation is altered. Particularly, the smaller the displacement thickness (i.e. the higher the Reynolds number, figure 5.1) the higher the growth rate.

Importantly, the saturation level of u'_{rms}/U_0 is only marginally affected by the Tu level and Reynolds number, being equal to about 20% for every condition, whereas the saturation level of v'_{rms}/U_0 reduces with increasing Tu and Reynolds number (results are reported in Table 5.3).

Tu	0.65%	1.20%	2.87%
$Re = 40000$	0.21	0.20	0.23
$Re = 75000$	0.21	0.19	0.21
$Re = 90000$	0.22	0.18	-

Tu	0.65%	1.20%	2.87%
$Re = 40000$	0.19	0.15	0.12
$Re = 75000$	0.15	0.13	0.09
$Re = 90000$	0.15	0.12	-

Table 5.3 (left) saturation level of u'_{rms}/U_0 and (right) v'_{rms}/U_0 for different Tu levels and Reynolds numbers.

5.1.3 Dynamic view of the laminar separation bubble

Thanks to the high frequency response of the PIV system, a dynamic view of the flow can be obtained by means of a sequence of evenly time spaced instantaneous velocity fields. figure 5.8 compares three sequences of vector maps of the perturbation velocity (defined by the classical Reynolds decomposition) for the cases previously discussed: $Re = 40000 - Tu = 0.65\%$, $Re = 40000 - Tu = 2.87\%$ and $Re = 90000 - Tu = 0.65\%$. Large scale vortical structures are shed near the time-mean bubble maximum displacement position, and they are clearly observable in all the plots. Red dotted lines connecting the center of the vortices allow estimating the propagation speed of these structures, thus the group velocity (C_g) of the

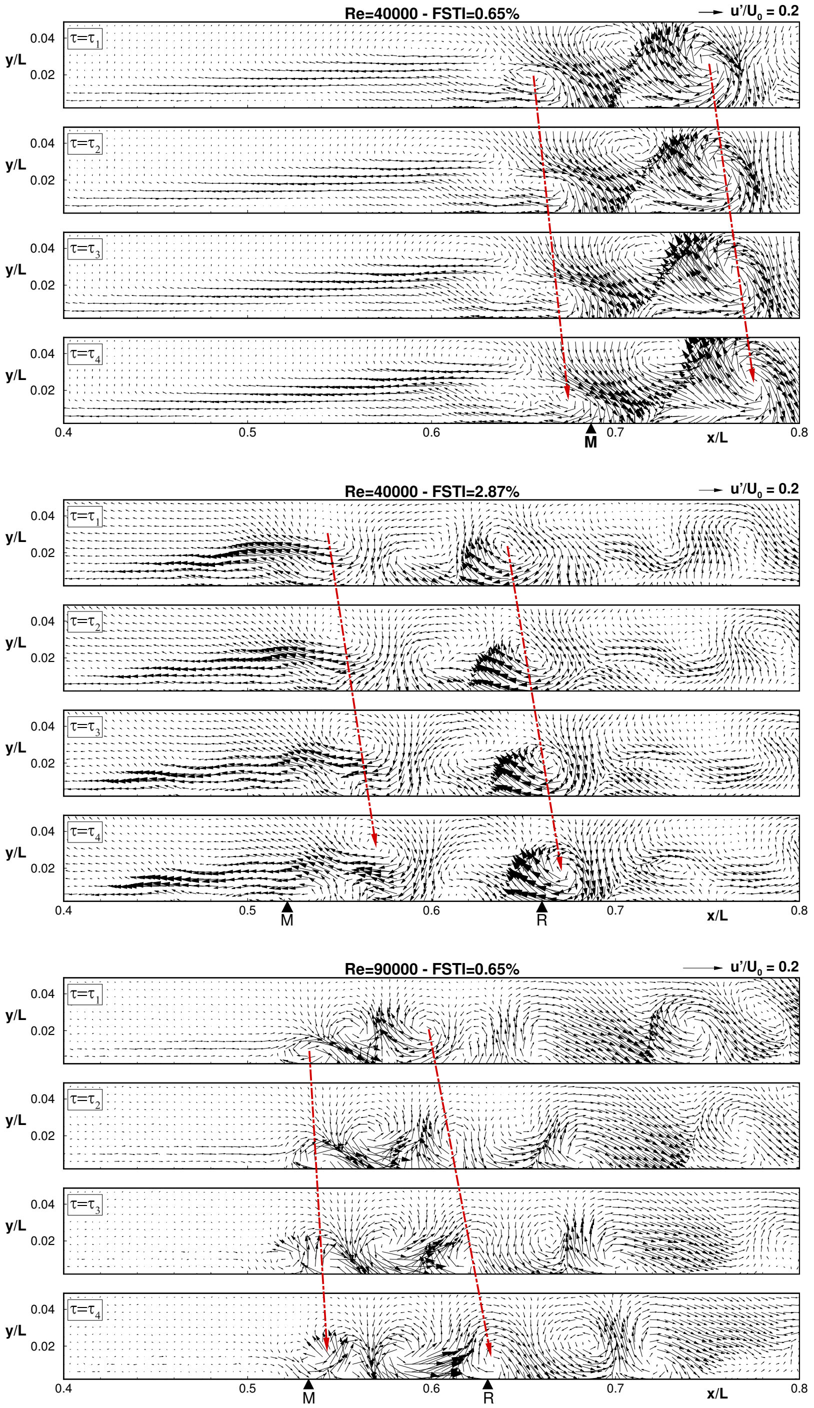

Fig. 5.8 Instantaneous perturbation velocity vector fields (u', v') for different Tu levels and Reynolds numbers. Red lines are superimposed to the plots to track vortices evolution. Reference vector length is also reported in the top-right corner for each condition. Time-mean maximum displacement (M) and reattachment (R) positions are labeled in the lower panel of each plot.

wave packet leading to the formation of the K-H rolls. Values measured for the different test conditions vary, once made dimensionless with the local free-stream velocity, in the range $0.40 < C_g/U_e < 0.48$ for the different Tu levels and Reynolds numbers. Interestingly, with high external forcing ($Re = 40000 - Tu = 2.87\%$) elongated pointing upstream perturbation velocity vectors can be observed into the separated shear layer, similarly to the instantaneous velocity maps shown in the works of Jacob and Durbin [46], Zaki [132] and Lengani et al. [66] for attached flows under elevated Tu. The vortex shedding activity appears significantly shifted upstream at high Tu levels and Reynolds numbers, according with the time-mean structure of the separated flow region previously observed. Moreover, the vortices are more confined toward the wall according to the reduction of the bubble maximum displacement (see section 5.1.2). On the other side, the wavelength of these structures appears much more influenced by the Reynolds number variation instead of the Tu variation.

In order to overcome the limitations of the visual inspection and to obtain a useful reduction of the experimental data collected for each condition, the POD has been adopted to provide a statistical representation of the dynamics governing the separated flow transition.

5.1.4 POD Results

Thanks to the ability of the POD to sort flow dynamics looking at their relative energy content, a statistical characterization of the dominant structures previously observed can be obtained. The systematic analysis for the characterization of the vortex shedding phenomenon reported in the following concerns with POD kernel defined by the normal to the wall velocity (v-based kernel). This gives rise to an orthonormal basis that better highlights structures associated with the K-H roll-up vortices ([62, 64]), filtering the dynamics inducing the streamwise velocity fluctuations previously observed in the fore part of the bubble. These latter dynamics are instead better highlighted by the most energetic modes obtained by the u-based kernel. This is evident in figure 5.9, where the first two POD modes obtained by the u and v-based kernels are reported for the reference condition $Re = 40000 - Tu = 0.65\%$. The vectorial representation of the POD modes is also superimposed to the plots. The vector components in the two cases are obtained by projection of the instantaneous fields on the two different orthonormal basis corresponding to the proper kernel. The time-mean bubble structure can be identified by means of the isocontour lines of the mean streamwise velocity. The distributions of the first two POD modes of the v-based kernel clearly provide the statistical representation of the vortex train shed behind the bubble maximum displacement position, since the projection of the instantaneous flow field on this eigenspace captures well the K-H dynamics. The modes assume not null values in the surround of the bubble maximum displacement position, and appear shifted of 1/4 of the observable wavelength. This is a

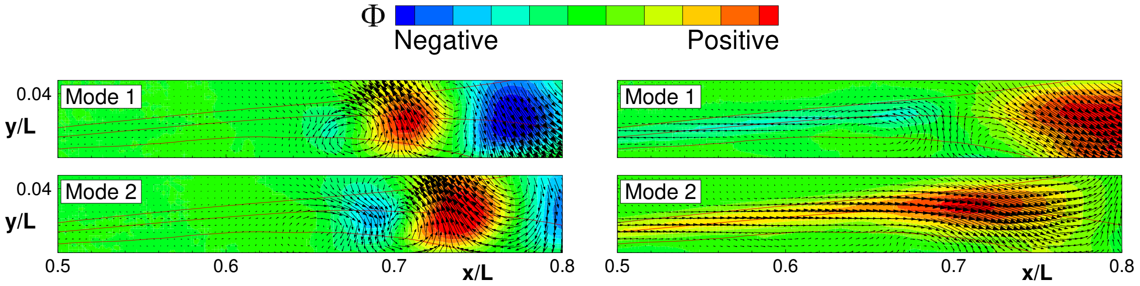

Fig. 5.9 First two POD modes of v-velocity (left) and u-velocity (right) based kernel for the condition $Re = 40000 - Tu = 0.65\%$. Vectorial representation of POD modes and isocontour lines of $\overline{u}/U_0$ = 0.0, 0.4 and 0.8 are superimposed to the plots.

common property of the POD when applied to pseudo-periodic convective flows (see Wee [124], Simoni et al. [62], Wen et al. [125] and Yarusevych et al. [131] for example). No oscillations are instead captured in the fore part of the separated shear layer. Conversely, the first two POD modes computed with the u-based kernel statistically describe "elongated" coherent oscillations inside the separated shear layer. Thus, the sub-space spanned by these two eigenvectors mainly captures the dynamics inducing streamwise velocity fluctuations in the fore part of the separated shear layer, while poorly highlights the K-H dynamics. In this case the shedding phenomenon has significant projection only onto the higher order eigenvectors, that require further efforts to be extracted. Since one of the main goals of this work is the characterization of the K-H instability driving the transition of the separated shear layer, the POD modes of the v-based kernel have been chosen to investigate the effects of Tu level and Reynolds number on the vortex shedding process.

The distributions of the first two POD modes of the v-based kernel for the four extreme conditions of the test matrix are plotted in figure 5.10. The relative energy content of the first two POD modes ranges from 26% to 11% for the cases $Re = 40000 - Tu = 0.65\%$ and $Re = 90000 - Tu = 2.87\%$, respectively. The higher the Tu level and/or the Reynolds number the smaller the energy captured by the first POD modes, since the transition process becomes more chaotic and characterized by the presence of a "broader band" of structures.

The Tu level increases from left to right in figure 5.10. Results clearly show that at $Re = 40000$ the POD modes are representative of the vortex shedding process and a shift of 1/4 of the wavelength is still observable between the 1^{st} and the 2^{nd} modes at the highest Tu level. Evidence of the shedding process can be detected far upstream with respect to the lower Tu condition, coherently with the anticipation of the bubble maximum displacement (compare with Table 5.1). Note that the wavelength characterizing the coherent structures is only marginally affected by the turbulence intensity variation. Moving from the top-left to the bottom-left corner of figure 5.10 Reynolds number increases at constant Tu

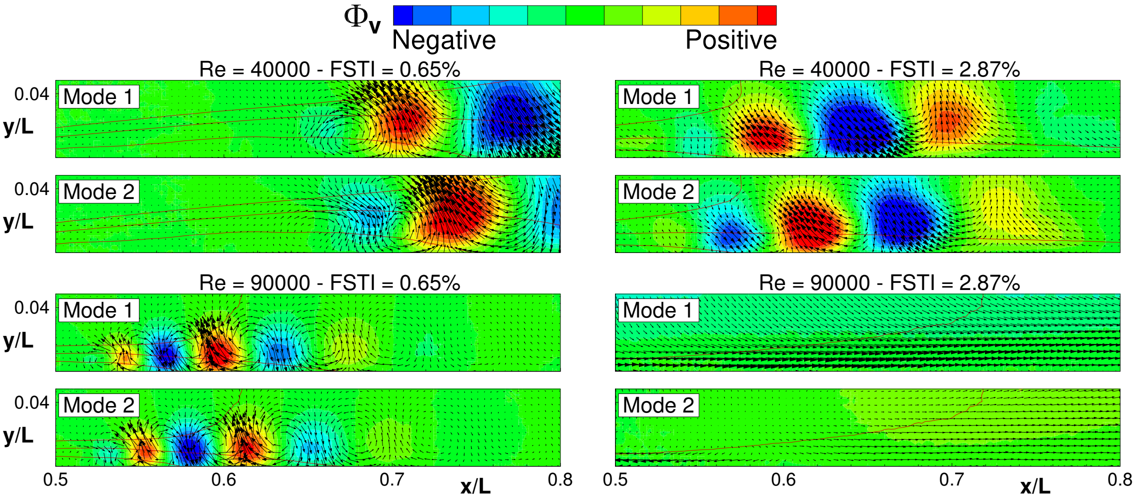

Fig. 5.10 First two POD modes of v-based kernel for extreme conditions of data set. Vectorial representation of POD modes and isocontour lines of $\overline{u}/U_0$ = 0.0, 0.4 and 0.8 are superimposed to the plots. For the condition $Re = 90000 - Tu = 2.87\%$ only the isoline $\overline{u}/U_0 = 0.8$ is reported.

level. Coherent vortical structures are still clearly recognizable downstream of the bubble maximum displacement position. They appear sensibly shifted upstream. Moreover, the vortex dimension and wavelength are significantly reduced. In the region downstream of $x/L = 0.7$ the boundary layer is in a fully attached condition (as shown by the shape factor distribution plotted in figure 5.6) and the intensity of the modes is almost null. The last condition of the test matrix on the bottom-right corner ($Re = 90000 - Tu = 2.87\%$) does not show any coherent structure and the intensity of the modes is almost zero everywhere (note that we are discussing only about the modes of the v-based kernel).

In order to better characterize the dynamics highlighted by the POD modes, the fast Fourier transform (FFT) of the corresponding temporal coefficients has been computed. The FFTs of the first POD eigenvectors are shown in figure 5.11 for the extreme test conditions, while the dominant peak and wavelength measured for all the other cases are reported in Table 5.4. The frequency resolution of the FFT is around 10 Hz and data concerning the peak frequency reported in Table 5.4 have been extracted using a cubic spline interpolation. A distinct peak at $f = 102$ Hz characterizes the spectrum of the 1^{st} eigenvector for the reference case ($Re = 40000 - Tu = 0.65\%$). The peak frequency is only slightly affected by the Tu level. Conversely, for $Re = 90000 - Tu = 0.65\%$ a sensibly higher dominant frequency is displayed by the diagram. Data reported in Table 5.4 further show that the Tu variation induces marginal effects on the vortex shedding frequency for all the different Reynolds numbers. Contrarily, the higher the Reynolds number the higher the peak frequency

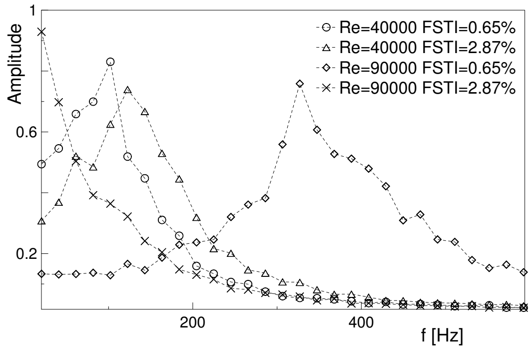

Fig. 5.11 FFT of first POD eigenvector of v-based kernel for extreme conditions of data set.

Tu	0.65%	1.20%	2.87%
$Re = 40000$	102	104	112
$Re = 75000$	225	245	256
$Re = 90000$	338	357	-

Tu	0.65%	1.20%	2.87%
$Re = 40000$	26	26	25
$Re = 75000$	20	18	18
$Re = 90000$	15	14	-

Table 5.4 (left) Peak frequency f_s [Hz] and (right) spatial wavelength λ_S [mm] of vortex shedding process for different Tu levels and Reynolds numbers.

characterizing the shedding phenomenon (as also discussed in the simplified model of Simoni et al. [107]). Opposite trend is shown by the spatial wavelength (see Table 5.4). The case $Re = 90000 - Tu = 2.87\%$ is dominated by low frequency oscillations, without any distinct peak in the related spectrum.

The wavelength and frequency characterizing the shedding phenomenon can be combined (equation 5.2) to compute the group velocity of the large scale coherent structures shown by the modes:

$$C_g = \lambda_s \cdot f_s \tag{5.2}$$

Results reported in Table 5.5 agree with the values previously computed by the visual inspection of the time sequences (see section 5.1.3). Thus, POD analysis also offers a rapid tool for the identification of the group velocity of the K-H rolls for the different cases.

Finally, the dimensionless shedding wave number parameter kl, involved in the temporal

Tu	0.65%	1.20%	2.87%
$Re = 40000$	0.46	0.49	0.49
$Re = 75000$	0.48	0.49	0.48
$Re = 90000$	0.47	0.48	-

Table 5.5 Dimensionless group velocity (C_g/U_∞) of K-H vortices computed by means of POD results. Values are normalized by free-stream velocity at bubble maximum displacement position.

formulation of the stability equations (see Häggmark et al. [39] and Simoni et al. [106] for example), has been computed. It is defined as $kl = 2\pi l/\lambda_s$, where l is the shear layer thickness at separation and λ_s is the wavelength characterizing the vortex shedding process. The wavelength is computed by the POD results, while the shear layer thickness at separation and the dimensionless distance of the shear layer from the wall (*d/l*) at the bubble maximum displacement position have been approximated by means of a simplified piecewise linear profile, as described in Simoni et al. [107].

The results of the present investigation provide values for kl in the range $0.74 < kl < 0.87$ for the different cases, in close agreement with the value predicted for the most amplified disturbance in a free mixing layer ($kl \approx 0.8$). The quite large distance of the shear layer from the wall at the maximum displacement position ($d/l > 1$ for all the different conditions) explains this agreement, because only minor wall damping effects on the most amplified frequency and spatial growth rate of the K-H instability are expected when d/l exceeds the threshold of 1 (see Diwan and Ramesh [27] and Simoni et al. [107]). Moreover, because of the small variation of the dimensionless wave number, the wavelength of the K-H structures for the different Reynolds numbers and Tu levels changes in the same way of the shear layer thickness. Thus λ_s decreases for higher Reynolds numbers, whereas it is marginally affected by the Tu level. This makes further evident that the dynamic properties of the shedding phenomenon are dominated by the parameter that mostly affects the shear layer thickness at separation.

5.1.5 Main findings on the effects due to Tu and Re variation on the separated flow transition mechanism

The results discussed here allows a characterization of the cross effects of Re and Tu on the separation induced transition process under fixed APG. The experimental data presented here constitute the starting point for the further analysis conducted under variable pressure gradient and reported in section 5.4. The time-mean results provide an overall view of the bubble response to large variation of both Tu and Re, for either short or long bubbles. The Tu level has been found to marginally affect the time-mean flow structure at separation. Similarly, the growth rate of the velocity fluctuations has been found to be only marginally affected by Tu variation for each Reynolds number tested. Thus, the bubble length and height reduction at high Tu level at fixed Reynolds number is due to the higher amplitude of velocity fluctuations penetrating into the separating boundary layer. Conversely, Reynolds number significantly influences the time mean boundary layer structure at separation. This translates into higher growth rates and different dynamic properties of the shedding phenomenon, even though the saturation level of streamwise velocity fluctuations has been found to be unaffected by both Tu and Reynolds number.

The dynamic analysis of the bubble and its POD statistical representation give further insight into the main properties of the K-H instability process. Instantaneous perturbation velocity vector maps highlight the large scale vortical structures shed near the bubble maximum displacement. Wavelength of the vortical structures shed near the bubble maximum displacement location is mostly affected by the Reynolds number. The higher the Reynolds number the smaller the wavelength of these structures. Variations of this quantity and of the dominant vortex shedding frequency have been found to be strongly related to the variation of the shear layer thickness at separation. The dimensionless wave number parameter kl well collapses to the value predicted by the linear stability theory for the different conditions, hence the vortex wavelength is approximately proportional to the shear layer thickness at separation for each condition tested.

5.2 Analysis of the statistical properties and dynamics evolution of the by-pass transition process under LPT-like adverse pressure gradient

Measurements carried out in the same test section adopted for the characterization of the separated flow response to Re and Tu variation has been used for the inspection of the by-pass type transition process under fixed APG. Particularly, the highest Tu level considered in the previous analysis (HTU_1 in table 3.1) together with a higher Reynolds number forced the BL to stay attached to the flat plate installed in the test section shown in figure 3.3. A single sensor hot-wire probe and a time-resolved PIV system have been employed for the investigations. The former allows high accuracy for the evaluation of the boundary layer integral parameters and the intermittency function of the flow, thus characterize in detail the statistical properties of the transition and explore self-similarity characteristics. The latter is used to provide a dynamic view of the structures propagating through the transitional boundary layer as well as free-stream region. Comparison with open literature results concerning transition under zero pressure gradient condition are presented. Overall, the dynamics driving the boundary layer transition, give further insights into the interpretation of the statistical properties of the by-pass transition process and highlight similarity characteristics as well as analogies with flat plate results in case of zero pressure gradient.

5.2.1 Measurement techniques

The test section used for this experimental study is shown in figure 3.3, which is the same of the previous section characterized by fixed pressure gradient imposed to the flow. For the present study the Reynolds number based on the inlet velocity and the plate length is 100000 and the inlet turbulence intensity induced by a turbulence generation grid is about 2.87% (see table 3.1). The high Reynolds number and turbulence intensity made sure of the occurrence of a by-pass transition. Further details about the experimental setup are provided in chapter 3.

A single-sensor miniature boundary layer hot-wire probe (DANTEC 55P15) has been adopted. The measuring grid was constituted of 25 traverses extending from $x/L = 0.2$ up to $x/L = 0.74$. Each traverse was constituted of 21 points along the normal to the wall direction with a smaller spacing close to the wall. In each point, 280000 samples have been collected with a sampling frequency of 40 kHz. Considering a confidence level of 95%, the uncertainty in the velocity measurements has been evaluated to be lower than 2%. In order to better quantify the pressure gradient imposed to the flow, the pressure gradient parameter

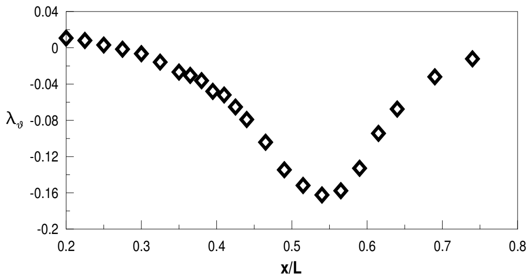

Fig. 5.12 Pressure gradient parameter λ_θ as function of the non-dimensional streamwise coordinate.

$\lambda_\theta = \theta^2/\nu(dU_e/dx)$ calculated from hot wire results is plotted in figure 5.12. The flow is accelerated up to $x/L = 0.285$, corresponding to the test section throat. Behind this position the flow undergoes strong diffusion, with a minimum of λ_θ at $x/L = 0.55$.

The DANTEC TR-PIV system described in chapter 3 has been also employed for the present measurement campaign. The measuring domain extends from $x/L = 0.315$ to $x/L = 0.9$. A time sequence of 3100 snapshots has been acquired at a sampling frequency of 3168 Hz in order to show the time-resolved behavior of the structures generating during transition. The magnification factor for the present experiments was set to 0.251 that allows sufficiently high spatial resolution. The cross-correlation function has been calculated over a 16×16 pixels interrogation area with a 50% overlap. This corresponds to a spatial resolution between independent samples of at least 0.638 mm and a distance between adjacent vectors of 0.319 mm (see Kähler [48] for further details). A Gaussian fitting procedure ensures a sub-pixel recognition accuracy of particle displacement of the order of 0.1 pixel, providing an experimental uncertainty for the instantaneous velocity of 3.0% of the maximum measurable one.

5.2.2 Hot-Wire PIV results comparison

The contours of the time-mean streamwise velocity and rms of velocity fluctuations normalized by the free-stream velocity at the domain inlet ($U_0 = 15.3$ m/s) are plotted in figure 5.13 and 5.14, respectively. The comparison between hot-wire and PIV results reveals that a reasonable agreement exists between the two data sets, thus allowing cross-checking of quantities extracted from either the two techniques in the following.

In figure 5.13 the time-mean defect of the flow momentum in the close to the wall region is clearly recognizable. The boundary layer thickness sensibly grows in the downstream direction as a consequence of the strong adverse pressure gradient imposed to the flow.

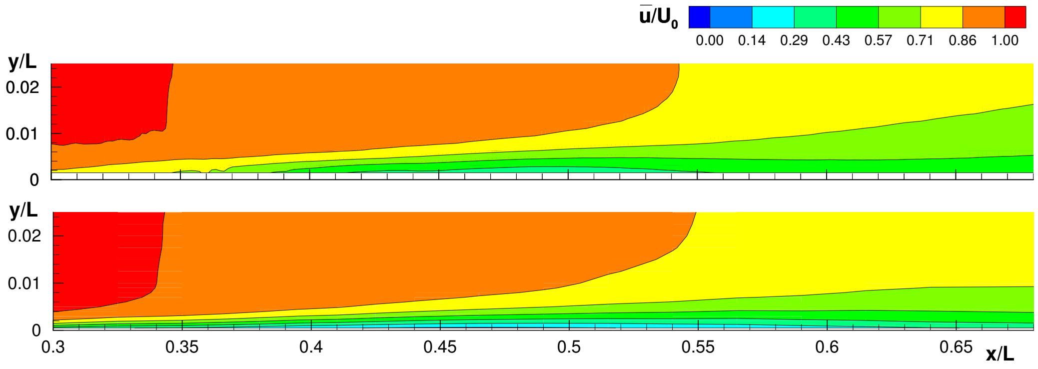

Fig. 5.13 Time-mean normalized streamwise velocity: PIV results (top); hot-wire results (bottom).

Similarly, figure 5.14 shows that the rms of the velocity fluctuations increases within the boundary layer in the downstream direction until saturation is reached. The increase of u'_{rms} and its further reduction suggests that the flow undergoes laminar to turbulent transition.

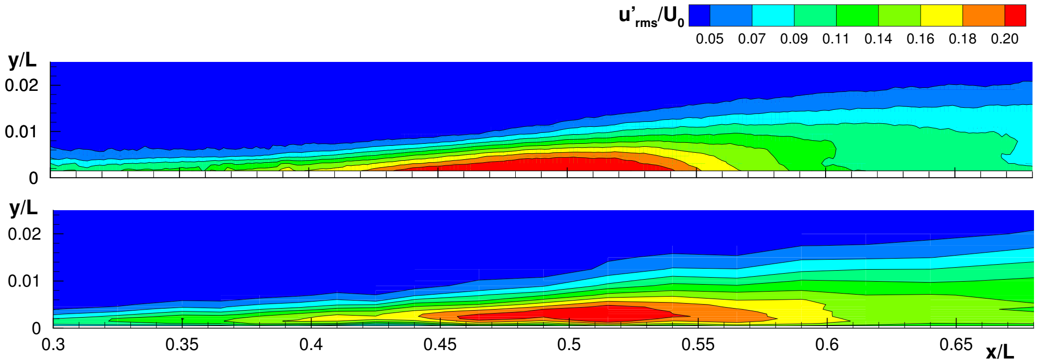

Fig. 5.14 Time-mean normalized streamwise velocity fluctuations rms: PIV results (top); hot-wire results (bottom).

5.2.3 Hot-wire results: statistical properties of the transition

The data from the hot-wire measurements have been used to compute the integral parameters of the boundary layer as well as the intermittency function of the flow in order to provide an overall statistical characterization of the transition process. The procedure described by Fransson et al. [32] has been adopted to compute the intermittency function. As suggested by the authors, data were high-pass filtered with a cut-off frequency equal to $f_{cut} = U_e/(5 * \delta)$

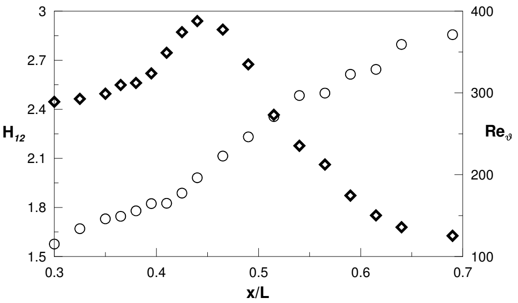

Fig. 5.15 Shape factor (rhombus symbol) and the momentum thickness Reynolds number (round symbols) distribution.

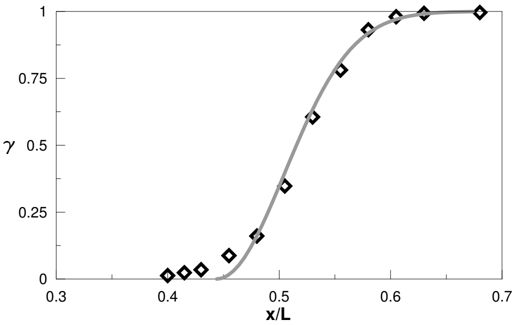

Fig. 5.16 Measured intermittency function (symbols) and Narasimha's universal curve (continuous line).

where δ is the boundary layer thickness and U_e is the local free-stream velocity. The intermittency presented in the following is evaluated in the normal to the wall position corresponding to the maximum velocity rms.

Figure 5.15 shows the shape factor H_{12} and the Reynolds number based on the momentum thickness Re_θ as functions of the non-dimensional streamwise coordinate x/L. The shape factor is about 2.5 in the region before $x/L = 0.4$, slightly smaller than the values for flat plate laminar boundary layers according to the acceleration imposed by the fore part of the channel. It rapidly rises behind $x/L = 0.4$ up to reach the value $H_{12} = 2.9$ at $x/L = 0.44$ and then reduces. The momentum thickness Reynolds number rises monotonically and a gradual change in the growth rate is observed around $x/L = 0.43$, where $Re_\theta \cong 190$. The intermittency function, plotted in figure 5.16, reveals that the onset of transition can be identified at $x/L = 0.44$ in correspondence of the peak of H_{12}. The non-dimensional spot production rate that appears into the universal law of Narasimha [86] is $\hat{n}\bar{\sigma} = 4.8 * 10^{-9}$. Further details on the definition of this parameter can be found in Simoni et al. [103]. According to the correlation proposed by Mayle [80] (see equation 2.57), with Tu $= 2.87\%$ the expected Reynolds number at the start of transition is $Re_{\theta S} \cong 200$ which is almost the measured value of Re_θ at $x/L = 0.44$.

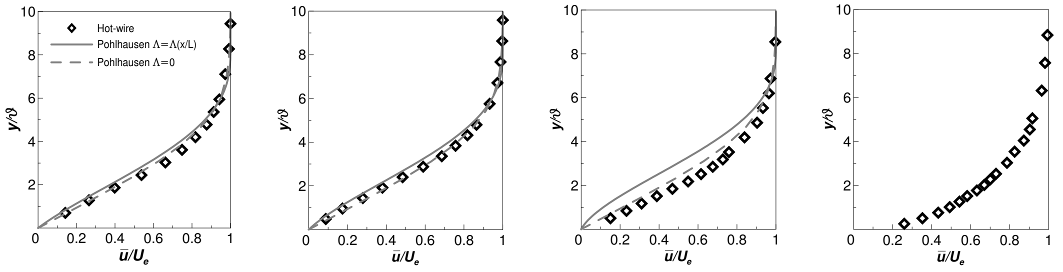

Fig. 5.17 Streamwise non-dimensional mean velocity profiles at *x/L*=0.41, 0.44, 0.52 and 0.59 moving from the left to the right of the figure.

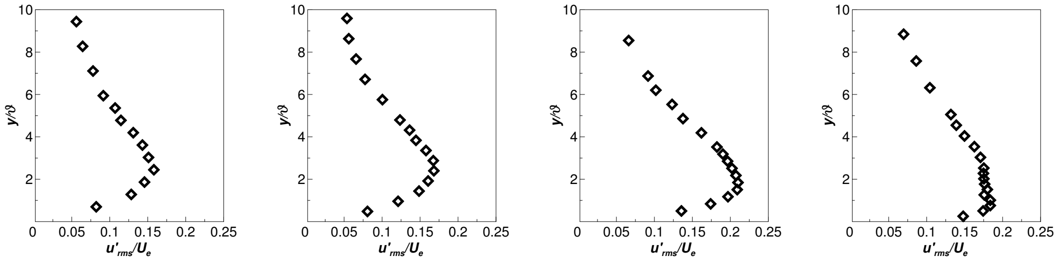

Fig. 5.18 Streamwise non-dimensional velocity rms profiles at *x/L*=0.41, 0.44, 0.52 and 0.59 moving from the left to the right of the figure.

The end of transition is recognized at $x/L = 0.58$ where $\gamma = 0.95$. It is worth noting that the shape factor continues to decrease even after the transition is complete. This behavior is in agreement with the observation of Halstead et al. [42], who showed that in the case of adverse pressure gradient the transition is rapid and H_{12} reaches the equilibrium sensibly after the transition end.

In order to better explore the similarity properties of the boundary layer through the transition process, local normalized velocity profiles of the streamwise time-mean velocity $\bar{u}/U_e$ and rms of velocity fluctuations u'_{rms}/U_e are plotted in figure 5.17 and 5.18, respectively. Four positions are considered, namely $x/L = 0.41, 0.44$, 0.52 and 0.59. They correspond to positions where the flow is fully laminar, at the onset of transition, where $\gamma = 0.5$ and where the flow is fully turbulent (i.e. $\gamma \cong 1$) respectively. The wall normal direction is scaled with the local momentum thickness of the boundary layer $\theta(x)$. The non-dimensional velocity $\bar{u}/U_e$ for the first three positions are compared with the Pohlhausen's velocity profile where the acceleration parameter $\Lambda(x) = \delta/\nu(dU_e/dx)$ is computed from the measured flow data. The case of $\Lambda(x) = 0$, that strictly corresponds to the Blasius' profile, is also added to the plots as a reference condition. It allows to better highlight the combined effects of the adverse pressure gradient and the turbulence penetrating into the pre-transitional part of the boundary layer on the time-mean boundary layer structure.

The boundary layer profiles appear strictly laminar in the first two positions, even for

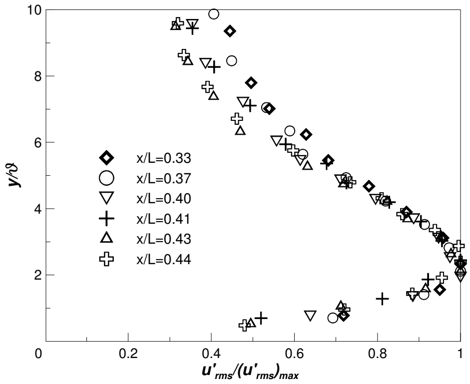

Fig. 5.19 (left) self-similarity of the $u'_{rms}/(u'_{rms})_{max}$ profiles in the laminar part of the boundary layer.

$x/L = 0.44$ where the intermittency of the flow starts rising. The Polhausen's profiles in both these positions show a lower momentum than the measured data. It is evident that the Blasius' profile provides a better fit of data. Thus, the high free-stream turbulence penetrating into the boundary layer in the pre-transitional part (as observed in figure 5.14) acts reducing the effect of the adverse pressure gradient on the inner part of the boundary layer, especially in terms of the profile curvature at the wall (see also Simoni et al. [108]).

In the third position the flow is transitional. It shows higher velocity in the close to the wall region if compared with the profiles in the previous positions, thus increasing also the velocity gradient at the wall (i.e. the skin friction, as expected during transition). Both reference velocity profiles fail to fit the experimental data. Finally, the last velocity profile in figure 5.17 is characteristic of a fully turbulent boundary layer, with evidently higher momentum in the close to the wall region with respect to the others.

The profiles of u'_{rms}/U_e for $x/L = 0.41$ and 0.44 show not null turbulence activity, even though the boundary layer is statistically in a laminar state. These profiles show an increasing maximum in the close to the wall region at $y/\theta = 2.3$, approximately in the position where $\bar{u}/U_e = 0.5$. The maximum shifts toward the wall ($y/\theta = 1.8$) as the flow becomes transitional (3^{rd} plot) and the peak of u'_{rms}/U_e increases up to 0.21. A local level of velocity fluctuations of about 20% is a good statistical threshold for streaks breakdown, according to the "breakdown amplitude" reported in Zaki [132] for flat plate boundary layer. In the 4^{th} plot the maximum u'_{rms}/U_e reduces to about 0.18.

In order to explore the similarity properties of the rms profiles, the latter are plotted in figure 5.19 against the dimensionless wall-normal coordinate y/θ for different streamwise positions. Interestingly, the rms profiles appear strictly self-similar in the laminar decelerating part of the boundary layer once adimensionalized with the local maximum rms. The position of the maximum keeps constant around $y/\theta = 2.3$. The momentum thickness results the best scaling quantity for the mean flow data in the present adverse pressure gradient case. Similar considerations have been proposed in the theoretical work of Bottaro et al. [8]. It is worth noting that the position of the maximum rms is sensibly lower than the one found by Luchini [68] in his theoretical work and also that observed by Westin et al. [126] and Matsubara [78] for flat plate ($y/\theta = 3.3$). Likely, the free-stream turbulence penetrating into the boundary layer, that reduces the effect of the pressure gradient in the inner layer as previously observed, also shifts the maximum of the disturbances towards the wall.

Finally, figure 5.20 shows the distribution of the maximum value of u'^2_{rms}/U_e^2 along the streamwise direction. It can be noticed that the pre-transitional part of the flow is characterized by a linear growth with x. Thereafter the growth rate increases around the position of the onset of transition (i.e. $x/L = 0.44$) where $u'^2_{rms}/U_e^2 \cong 0.03$ and it reaches the peak value at $x/L = 0.52$, where $\gamma \cong 0.5$. It further reduces and starts saturating at the end of the measuring domain. The behavior of u'^2_{rms}/U_e^2 is strictly like the one observed by Westin et al. [126] and Matsubara [78] for the zero pressure gradient flow, where streak dynamics have been documented to dominate the transition process.

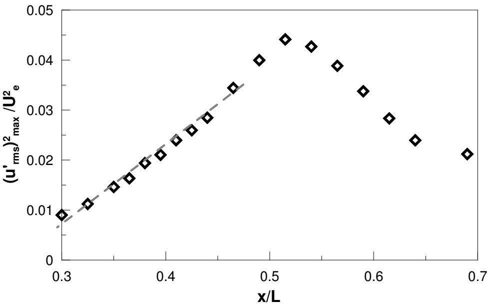

Fig. 5.20 Variation of the maximum value u'^2_{rms}/U_e^2 along the streamwise direction.

5.2.4 Instantaneous PIV Results

The dynamics driving the transition process under the condition tested can be captured thanks to the time-resolved PIV adopted in this work, similarly to what done for the insepction of the spearated flow response previously described. To this end, a sequence of evenly time spaced perturbation velocity maps is presented in figure 5.21, highlighting coherent structures propagating in both the free-stream and boundary layer. Note that contour plots are representative of flow regions where $|u'/U_e| \geq 0.15$, thus better highlighting the likely occurrence of the breakdown of boundary layer streaks (see Zaki [132]).

In the first image an elongated low speed streak ($u' < 0$) extends between $x/L = 0.46$ and

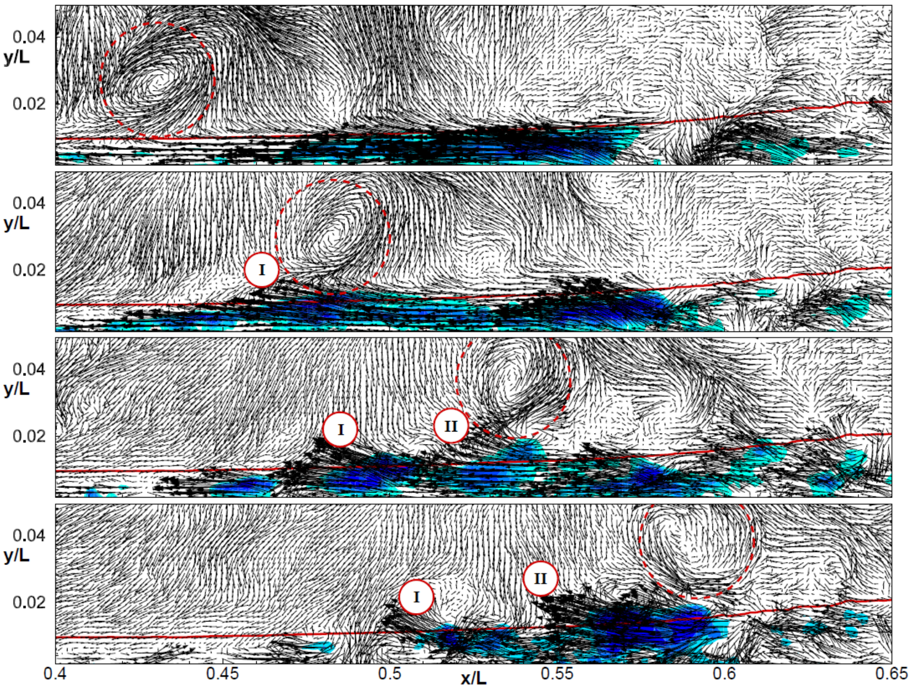

Fig. 5.21 Instantaneous perturbation velocity vector fields (u', v'). Q_2 events are labeled I and II. Free-stream vortical structure is traced by means of red circles. Time-mean boundary layer edge is also shown (red line).

$x/L = 0.57$ (blue contour), inducing large streamwise velocity fluctuations in the surround of the maximum u'^2_{rms}/U_e^2 ($x/L = 0.52$, where $\gamma \cong 0.5$). In the same snapshot a large scale vortical structure is observable into the free-stream region (red circle). It propagates above the streak in the subsequent frames and does not penetrate into the boundary layer, even if it seems to have a crucial role in the breakdown process. Indeed, a kind of relation seems to exist between the position of the free-stream structure tracked in the different snapshots and the occurrence of $Q2$ events (i.e. *ejections*, see Jacob and Durbin [46]). The term $Q2$ *event* refers to events characterized by negative streamwise velocity fluctuations ($u' < 0$) and positive normal to the wall fluctuations ($v' > 0$) (see e.g., Adrian [3]). The occurrence of such events results in the lifting up of low-speed streaks toward the edge of the BL, promoting their instability due to the possible interaction with free.stream disturbances (see Tardu [116], Jacob and Durbin [46] and Zaki [132]). This kind of phenomenon is first observed in the 2^{nd} snapshot of figure 5.21 at about $x/L = 0.48$ (I), where the low-speed streak in the BL starts to lose the ordered pattern characterizing the streak in the first map presented. Additional Q_2 events are induced in the 3^{rd} velocity map after the free-stream vortex has further propagated (II) and higher distortion of the streaky structure is recognizable. In the 4^{th} image the free-stream vortex is at the end of the transitional region (where $\gamma \cong 0.98$) and

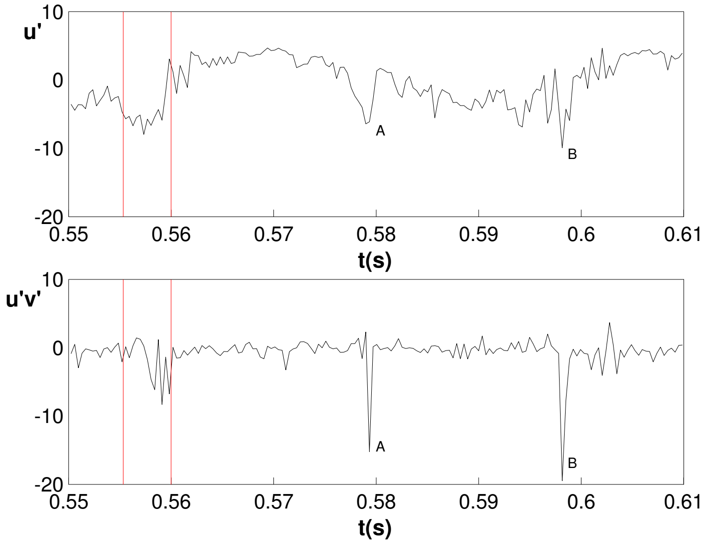

Fig. 5.22 Time trace of perturbation velocity u' (top) and instantaneous shear term $u'v'$ (bottom). The time interval corresponding to the sequence shown in figure 5.21 is identified between red lines.

large nuclei of Q_2 events are observable downstream of $x/L = 0.52$, as a consequence of streak breakdown.

In order to better highlight the link between streak breakdown and shear stress production, thus transition, the evolution of the instantaneous streamwise perturbation velocity u' and the shear term $u'v'$ are presented in figure 5.22. Note that the selected time trace extends over the time interval corresponding to the sequence of velocity maps presented in figure5.21 (highlighted with red lines in the plots). In this interval a negative peak in the evolution of u' is clearly recognizable. Two other peaks are observable at about $t = 0.579$ and $t = 0.598$ (labeled A and B in the plot). The related vector maps (not shown here for brevity) reveal that low speed streaky structures occur in the boundary layer at these time instants. In the first part of the time interval corresponding to the sequence of velocity maps presented in figure 5.21 the term $u'v'$ is almost null, even though the u' exhibits negative values. This is coherent with the occurrence of an ordered streak as observed in the first frame of figure 5.21. Subsequently, $u'v'$ assumes relevant negative values when the generation of Q_2 events are recognizable in figure 5.21. The PIV observations reported here highlight the role of BL streaks in the transition process, as also shown by Mandal [71] and Zaki [132]. They are responsible for the occurrence of the large streamwise velocity fluctuation highlighted by the statistical results reported in figure 5.20. Moreover, free-stream vortices seem to play a crucial role in promoting streaks breakdown, according to the models proposed by Jacob and Durbin [46] and Bradt et al. [13] based on their numerical results over flat plate.

5.2.5 Main findings on Tu and APG effects on the by-pass transition process.

The measurements presented in this section allowed the characterization of the by-pass transition process at fixed Re, Tu and APG. The attached flow condition has been obtained by means of elevated free-stream turbulence and Re, for the given APG. For different pressure gradients imposed to the flow, different values of Re and Tu are supposed to lead the transition process from the separation induced to the by-pass type, thus suggesting the need for further analysis on this kind of transition process for a wider range of Re, Tu and APG.

The integral parameters and the intermittency function reveal that the onset of transition can be identified in correspondence of the peak of H_{12}. Moreover, due the adverse pressure gradient, the transition is rapid and H_{12} reaches the equilibrium level sensibly after the transition end. The profiles of the mean streamwise velocity and velocity fluctuations rms show a self-similar behavior in the laminar part of the boundary layer. Here the momentum thickness resulted the best scaling quantity. It follows that the momentum thickness could be the optimal scaling quantity to be used for the development of empirical correlations aimed at the characterization of the global response of the transition process in case of both separated flow (previously analyzed) and by-pass transition.

The high free-stream turbulence acts reducing the effects of the pressure gradient on the curvature of the mean velocity profile and shifting the maximum of the turbulence peak towards the wall (at $y/\theta = 2.3$) with respect to a flat plate boundary layer perturbed by streaky structures.

PIV measurements show the processes leading to the generation of the main coherent structures that drives the transition process. Particularly, sequences of instantaneous velocity maps show that the breakdown of boundary layer streaks occurs more likely near the mid-transition point where the intermittency function is $\gamma \cong 0.5$ and free-stream vortical structures act destabilizing the boundary layer streaks, forcing $Q2$ events to occur.

5.3 Applications of the Weighted-POD procedure to experimental data concerning attached and separated flows.

In the previous sections the BL transition has been characterized in terms of the time-mean and dynamic response to the Re and Tu variation in case of both separation induced and by-pass transition. For what concerns the separated flow transition, boundary layer streaks were supposed to populated the fore part of the laminar separation bubble for high Tu level, while in the rear part of the bubble K-H vortices dominate. On the other hand, in case of by-pass transition free-stream vortices have been found to play a crucial role into the breakdown of the BL streaks, thus promoting transition. This means that different structures that are known to be characterized by a sensibly different energy content (e.g. BL streaks and free-stream structures) contribute to the BL transition in case of both attached and separated flows. With the aim of providing a statistical analysis of the coexistence and possible interaction between the different structures observed in such different transition processes, the WPOD procedure and the Fourier-based decomposition technique described in sections 4.3 and 4.4 are applied here to two different experimental data sets. More precisely, the condition at low Re and high Tu described in section 5.1 ($Re = 40000 - Tu = 2.87\%$) and the condition at high Re and high Tu level analyzed in section 5.2 ($Re = 100000 - Tu = 2.87\%$), are considered here for the application of the WPOD procedure to separated and attached flow conditions, respectively. The snapshot POD of Sirovich [110] (named POD in the following) has been applied first to the data sets to obtain a statistical reduction of the PIV data presented in the previous sections as well as to provide the reference results for the comparison with the WPOD procedure.

5.3.1 By-pass Transition

The first condition examined concerns the attached flow undergoing laminar to turbulent transition at high Reynolds number (100000) and high Tu level (2.87%) described in section 5.2. The streamwise and normal to the wall velocity distributions normalized by the free-stream velocity at the measuring domain inlet (U_0) are reported in figures 5.23 and 5.24, together with the corresponding fluctuations rms. Figure 5.23 highlights the defect of flow momentum and the occurrence of the BL transition (growing and reduction of u'_{rms}/U_0) already highlighted in section 5.2. The transition onset was found at $x/L = 0.44$ while the fully turbulent condition is reached at about $x/L = 0.6$. The normal to the wall velocity fluctuations (bottom plot of figure 5.24) are limited in the fore part of the transition process, and become relevant only in the later stage of transition, as it typically occurs in by-pass

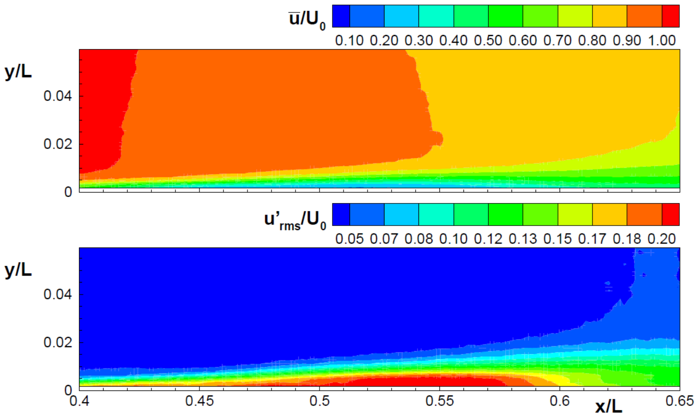

Fig. 5.23 Time-mean normalized streamwise velocity $\overline{u}/U_0$ (top) and rms of velocity fluctuations u'_{rms}/U_0 (bottom). Streamwise and the normal to the wall coordinates are scaled by the plate length L.

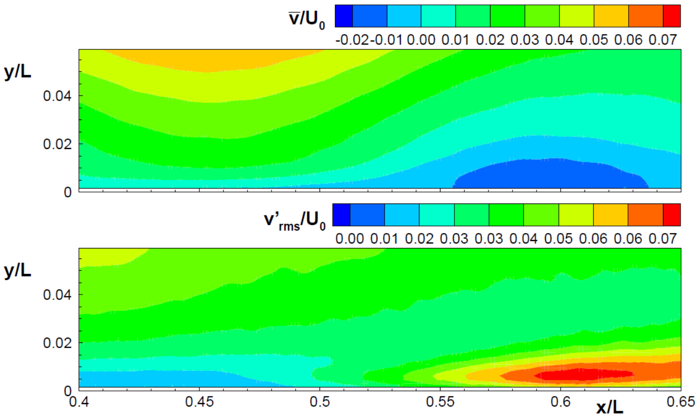

Fig. 5.24 Time-mean normalized normal to the wall velocity $\overline{v}/U_0$ (top) and rms of velocity fluctuations v'_{rms}/U_0 (bottom). Streamwise and the normal to the wall coordinates are scaled by the plate length L.

processes (see e.g., Zaki [132], Simoni et al. [103]).

As a first step, the comparison between the energy content of reconstructed fields obtained from an increasing number of POD and WPOD modes is presented in figure 5.25 with the aim of discussing the optimality characteristics of the new procedure. Particularly, the energy content of the 1^{st} POD and WPOD mode is 19% and 10%, respectively. The shift between the two curves reported on the right of figure 5.25 is due to the loss of optimality of the WPOD. However, after the first 10 modes the two curves do not differ by more than 5% and by no more than 3% after 100 modes. Note, that even though a small number of modes is typically needed to well reproduce simple or at least slightly complex flows, such as the wake of a circular cylinder or the mixing layer in axisymmetric jets (see Citriniti et al. [20]

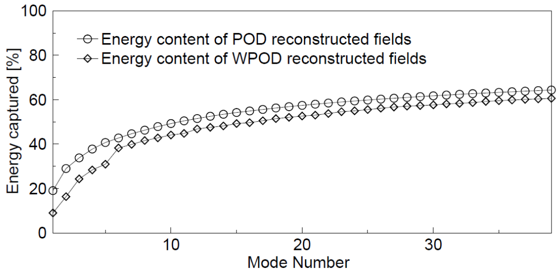

Fig. 5.25 Energy content of reconstructed fields obtained from an increasing number of WPOD (rhombus point symbols) and POD (circle point symbols) modes.

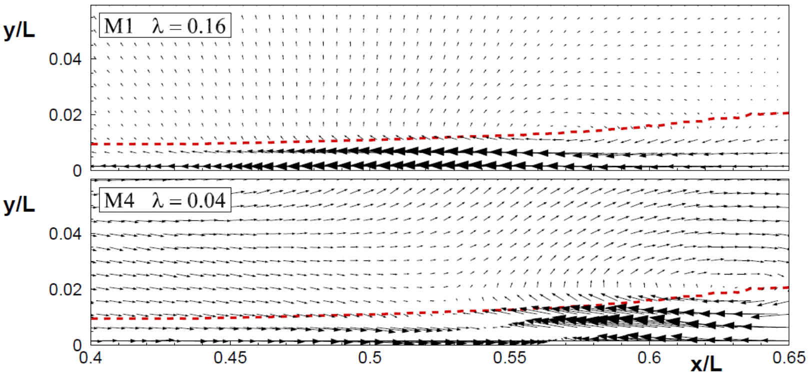

Fig. 5.26 Vector fields of selected POD modes. Mode number and energy content are indicated in the upper-left corner of each plot. Mean boundary layer thickness is indicated by red line.

and Perrin et al. [92] for instance), a higher number of modes are required in the case of strongly inhomogeneous flows, as also discussed in Glauser et al. [35]. Specific attention should be paid to the calculation of the energy magnitude of reconstructed fields when using a certain number of WPOD modes for the reconstruction. Indeed, modal interaction exists due to the non-orthogonality of the eigenvectors of the weighted correlation matrix defined by the 4.17. As a consequence, the energy content of the fields reconstructed with a specific number of WPOD modes differs from the sum of the energy captured by the same modes (i.e. the sum of the corresponding eigenvalues). For the given data set, the sum of all the WPOD and POD eigenvalues differ by no more than 3% of the overall TKE.

The POD was applied to the present data set with the aim of providing a statistical representation of what observed in section 5.2 by means of the PIV results, as well as to highlight the differences with the proposed WPOD procedure. To this end, two POD modes are reported in figure 5.26, where the vectorial representation of the modes, obtained by projection of the streamwise and normal to the wall velocity fields onto the POD eigenvectors, allows the visualization of the structures captured by the decomposition. The mode in the

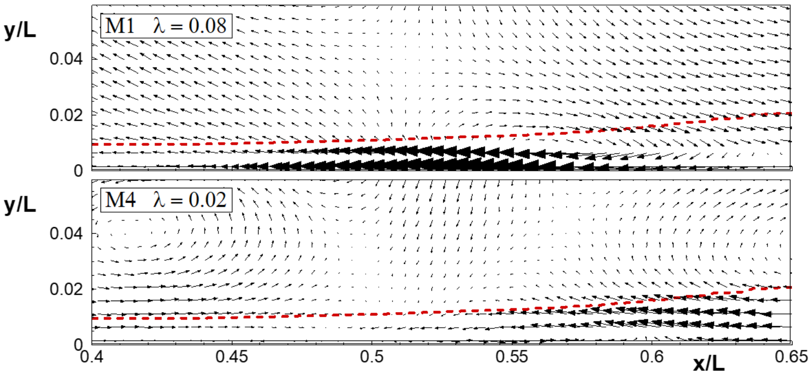

Fig. 5.27 Vector fields of selected WPOD modes. Mode number and energy content are indicated in the upper-left corner of each plot. Mean boundary layer thickness is indicated by red line.

upper plot of this figure (mode 1) shows a streamwise elongated structure in the region where an ordered streak was observed in the first PIV snapshot reported in figure 5.21. Note that in this context the POD provides a statistical reduction of the instantaneous PIV snapshots collected. The highest fluctuations shown by the first POD mode reported in figure 5.26 are in correspondence with the highest values of u'_{rms} observed in figure 5.23 and the peak of the the local maximum TKE distribution presented in figure 5.20. In the bottom plot of figure 5.26 (mode 4), vectors pointing upstream are observed close to the position of the transition end ($x/L = 0.6$) and a vortical structure is recognizable at the edge of the boundary layer. At this position, strong $Q2$ events were observed in the instantaneous PIV snapshots reported in figure 5.21.

To highlight the specific features of the new method, thus further emphasizing the additional information extracted by this procedure, two WPOD modes showing boundary layer structures similar to those shown in figure 5.26 are reported in figure 5.27. The WPOD mode in the upper plot of this figure (mode 1) is very similar to the first POD mode presented in figure 5.26, but free-stream fluctuations are better captured. The same is for the bottom plot of figure 5.27 (mode 4) where free-stream fluctuations are more evident than in the second POD mode presented in figure 5.26: a free-stream vortex is observed in the bottom plot of figure 5.27 at the measuring domain inlet that is not recognizable in the corresponding POD mode. Now, following the procedure described in section 4.4, the WPOD modes shown in figure 5.27 were further decomposed as a linear combination of pure sinusoidal contributions, thus isolating structures that occur at different frequencies. For the present case, the results obtained by the same decomposition of the POD modes of figures 5.26 will be presented with the aim of discussing the main differences between the application of the proposed method to the WPOD and the POD modes. The FFTs of the WPOD temporal

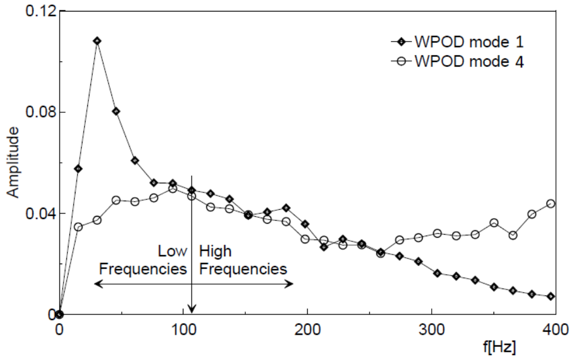

Fig. 5.28 FFTs of the eigenvectors corresponding to the WPOD modes 1 (rhombus point symbols) and 4 (circle point symbols) of figure 5.27.

coefficients have been computed first to provide the frequency content of the structures captured by the corresponding modes (see figure 5.28). A low frequency peak with rapid energy decrease characterizes the spectrum of the WPOD mode 1 (rhombus point symbols), while a broader band spectrum characterizes the structures depicted by the WPOD mode 4 (circle point symbols). Then, two bands were taken into account for the decomposition of the modes by equation 4.24. More precisely, the frequency capturing similar energy in both spectra was chosen to distinguish between low and high frequency contributions, as shown in the figure. The low frequency activity mostly characterizing the first WPOD mode is therefore isolated from the higher frequencies animating the second mode presented. Similar results have been found by means of the FFTs of the POD temporal coefficients, thus the same frequencies were adopted for the decomposition of the corresponding modes. In both cases the original modes are obtained from the sum of these partial reconstructions.

Low and high frequency contributions to the POD modes presented in figure 5.26 are shown in figures 5.29 and 5.30, respectively (vectors are enlarged in the case of high frequency contributions to the modes because of their lower energy content). The low frequency contributions to the modes are related to ordered boundary layer streaks (as also shown in Zaki [132]) and the plots look quite similar to the original modes of figure 5.26. The same holds for the high frequency contributions to the POD mode 1 (upper plot of figure 5.30) which is still representative of an elongated structure in the boundary layer region, even if a slightly wavy shape of this structure is recognizable just before $x/L = 0.6$. On the other hand, Q_2 events are recognizable in the bottom plot of figure 5.30 at $x/L = 0.6$, that were not observable in the corresponding original mode. Both the low and high frequency contributions to the POD modes presented are ultimately related to boundary layer structures.

The low frequency contributions to the WPOD modes are reported in figure 5.31 and they are related to the propagation of boundary layer streaks. Interestingly, in the present

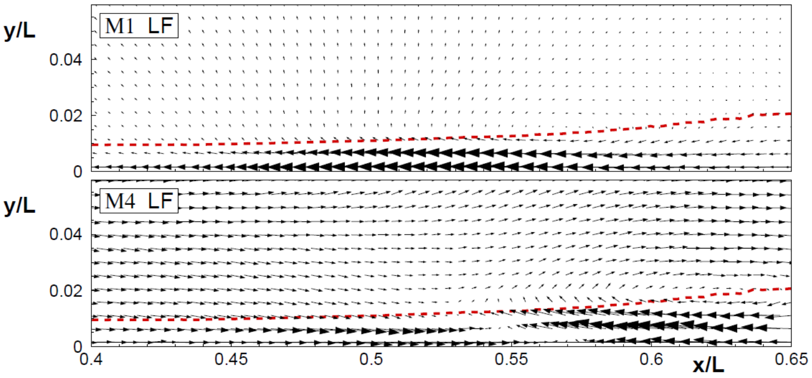

Fig. 5.29 Low frequency (LF) contributions to the POD modes 1 and 4. Mode number is indicated in the upper-left corner of each plot. Mean boundary layer thickness is indicated by red line.

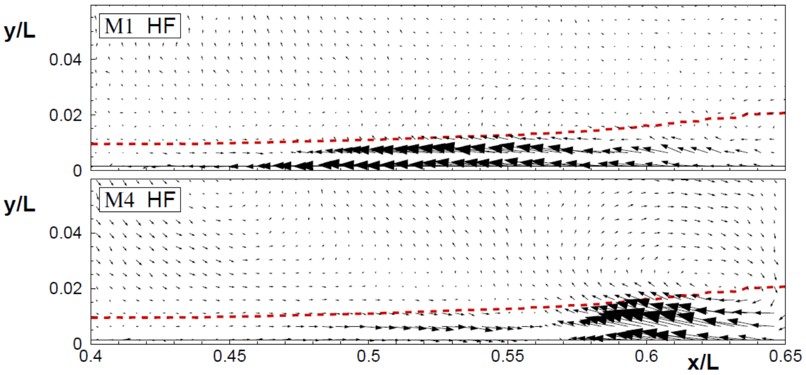

Fig. 5.30 High frequency (HF) contributions to the POD modes 1 and 4. Mode number is indicated in the upper-left corner of each plot. Mean boundary layer thickness is indicated by red line.

case the higher frequencies (figure 5.32) characterize mostly free-stream vortices which are located above the boundary layer edge, showing similarities with the *shear sheltering* mechanism well described by Jacob and Durbin [46] and successively by Zaki [134]. This represents the main difference between the results obtained by the proposed Fourier based decomposition of the POD and the WPOD modes. The weights introduced in the new procedure acts enhancing the spatial homogeneity of the data set, thus highlighting the less energetic high frequency fluctuations that animate here free-stream structures. In the bottom plot of figure 5.32, Q_2 events around $x/L = 0.6$ are also more evident than in the original WPOD modes. On the other hand, bursting events are not observable in the top plot of this figure where free-stream structures are evidently characterized by larger length scale. Velocity fluctuations associated with streak breakdown are animated by the same frequencies characterizing some of the propagating free-stream vortices, depending on their dimensions,

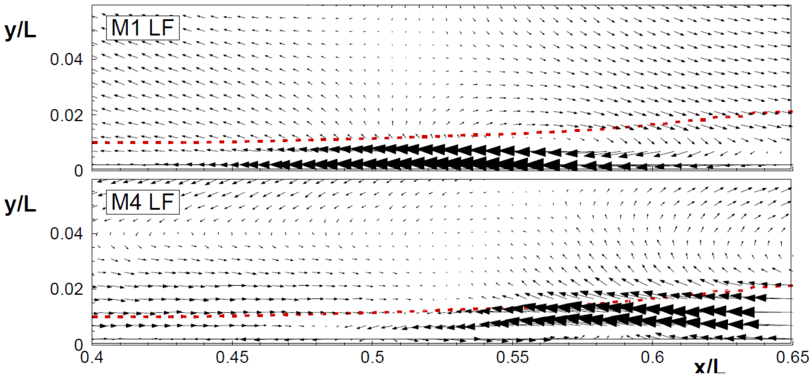

Fig. 5.31 Low frequency (LF) contributions to the WPOD modes 1 and 4. Mode number is indicated in the upper-left corner of each plot. Mean boundary layer thickness is indicated by red line.

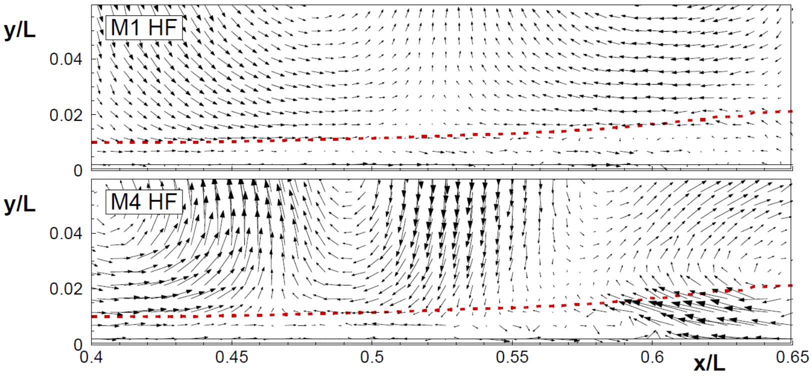

Fig. 5.32 High frequency (HF) contributions to the WPOD modes 1 and 4. Mode number is indicated in the upper-left corner of each plot. Mean boundary layer thickness is indicated by red line.

suggesting that interaction mechanisms may exist between free-stream and boundary layer structures in a particular range of scales.

5.3.2 Separated flow transition

The second data set considered here concerns separated flow transition under elevated free-stream turbulence. Particularly, the condition characterized by the lowest Reynolds number and the highest Tu level ($Re = 40000 - Tu = 2.87\%$) discussed in section 5.1 is considered. The contour plots of the streamwise and normal to the wall velocities $\overline{u}/U_0$ and $\overline{v}/U_0$, and their rms distributions u'_{rms}/U_0 and v'_{rms}/U_0 are reported in figure 5.33 and 5.34. Note that the contours of $\overline{u}/U_0$ and u'_{rms}/U_0 are the same shown in figure 5.3 and 5.4. The flow region with negative velocity confirms the occurrence of a separation bubble. The separation and

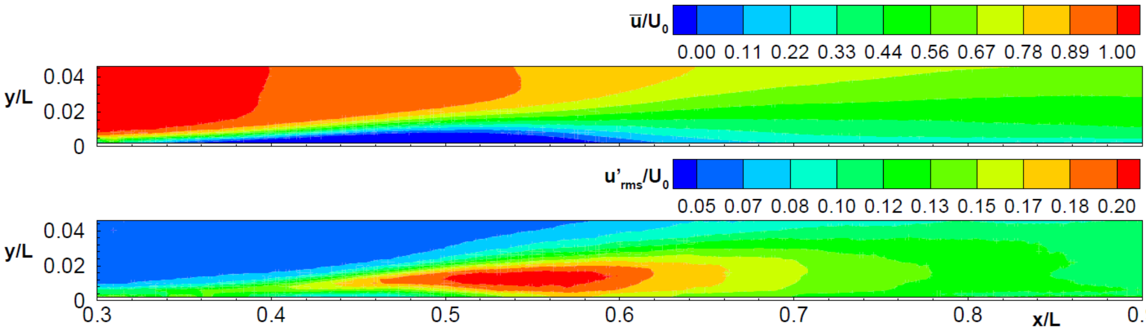

Fig. 5.33 Time-mean normalized streamwise velocity $\overline{u}/U_0$ (top) and rms of velocity fluctuations u'_{rms}/U_0 (bottom). Streamwise and the normal to the wall coordinates are scaled by the plate length L.

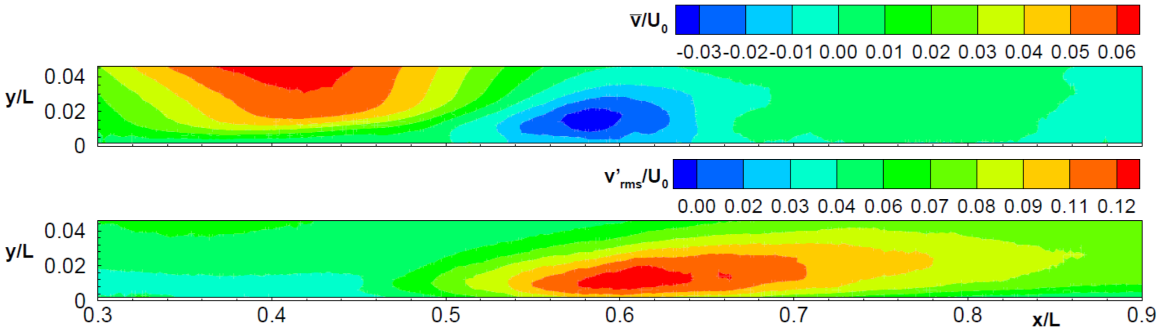

Fig. 5.34 Time-mean normalized normal to the wall velocity $\overline{v}/U_0$ (top) and rms of velocity fluctuations v'_{rms}/U_0 (bottom). Streamwise and the normal to the wall coordinates are scaled by the plate length L.

maximum displacement positions are $x/L = 0.39$ and $x/L = 0.52$, respectively, as highlighted by the integral parameters distribution discussed in section 5.1. Significant values of u'_{rms}/U_0 are observable in the fore part of the separated shear layer, while velocity fluctuations in the normal to the wall direction are negligible in this region and start to grow near the bubble maximum displacement position. This highlights the existence of different dynamics involving the separated boundary layer regions as also mentioned in section 5.1.

The optimality characteristics of the new procedure are discussed with reference to figure 5.35, where the energy magnitude of fields reconstructed with an increasing number of POD and WPOD modes is reported for the present case. The energy captured by the 1^{st} POD and WPOD mode is 14% and 8% of the total kinetic energy, respectively. The difference between the two curves is 6% after 10 modes and they differ by no more than 2% after 100 modes. As stated above, the non-orthogonality of the WPOD eigenvectors implies that the energy magnitude of the fields obtained by reconstruction from a selected number of WPOD modes differs from the sum of the corresponding eigenvalues. The difference between the sum of all

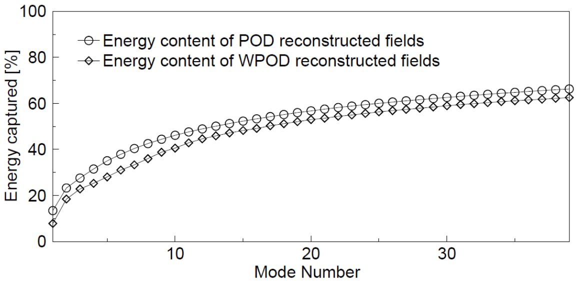

Fig. 5.35 Energy content of reconstructed fields obtained from an increasing number of WPOD (rhombus point symbols) and POD (circle point symbols) modes.

the POD and WPOD eigenvalues is lower than 2%, providing also in this case an estimation of the marginal effects of the non-orthogonality of the modes.

Figure 5.36 shows the vectorial representations of two POD modes in order to highlight the main structures captured by the POD applied to the present data set, providing also the reference cases for the comparison with the WPOD procedure. The mode 3 in the upper plot shows negative vectors in the fore part of the separated shear layer, while a large scale structure occurs behind the maximum displacement position at $x/L \approx 0.67$ and $y/L \approx 0.04$. The mode presented may be linked to the motions of the whole bubble due to the feed-back loop mechanism and mean flow deformation (see Marxen et al. [76]), or the propagation of streaky structures in the separated shear layer, due to the quite high Tu level. Otherwise, the POD mode 5 in the bottom plot of this figure clearly highlights a sequence of counter-rotating vortices generating downstream of $x/L = 0.58$, while the POD vectors are smaller upstream of this position, even though they are still recognizable. The present mode is mostly representative of the shedding process dominating the rear part of the bubble

To show the applicability of the WPOD in such flow configuration, two WPOD modes that are similar to those shown in figure 5.36 are presented in figure 5.37. The mode in the upper plot of this figure is very similar to the first POD mode depicted in figure 5.36 even though velocity fluctuations in the separated shear layer are more highlighted by the new procedure. A wavy streamwise oriented structure is evidently captured by the mode between $x/L = 0.46$ and $x/L = 0.6$ while large scale vortices are shown behind these positions. The less energetic structures occurring upstream of the bubble maximum displacement position are more highlighted thanks to the normalization terms introduced in the optimization problem driving the initial step of the WPOD procedure. On the other hand, the WPOD mode shown in the bottom plot of figure 5.37 is representative of the vortex shedding phenomenon observable behind the bubble maximum displacement position. The same wavelength observed in the bottom plot of figure 5.36 is provided by the spatial distribution of the mode, while free-stream fluctuations not shown by the corresponding POD modes are now clearly observable

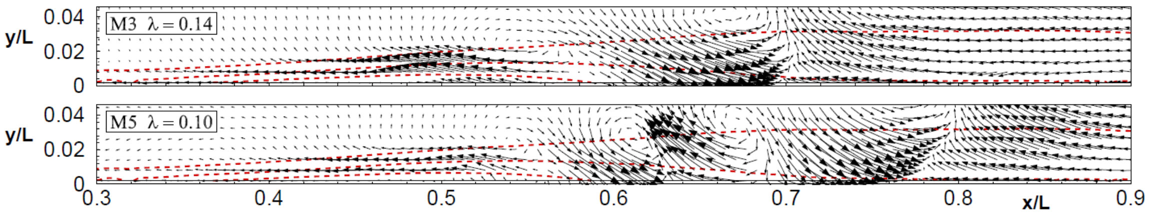

Fig. 5.36 Vector fields of selected POD modes. Mode number and energy content are indicated in the upper-left corner of each plot. Mean flow structure is highlighted by iso-contour lines of the mean velocity (red lines).

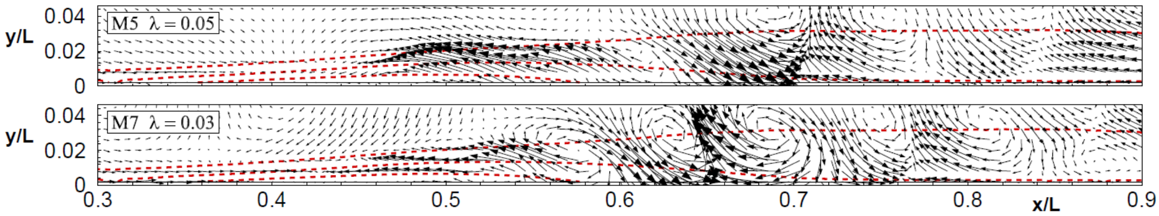

Fig. 5.37 Vector field of selected WPOD modes. Mode number and energy content are indicated in the upper-left corner of each plot. Mean flow structure is highlighted by iso-contour lines of the mean velocity (red lines).

upstream of $x/L = 0.45$ over the edge of the separated boundary layer.

The same Fourier-based decomposition adopted for the previous data set has been used to investigate the frequency content of the WPOD temporal coefficients and the related dynamics. The decomposition of the POD modes will not be discussed since the main differences between the application of this procedure to the WPOD and POD modes have been already pointed out in the previous section. The FFTs of the eigenvectors corresponding to the WPOD modes presented in figure 5.37 were therefore computed and they are shown in figure 5.38. Low frequency fluctuations mostly contribute to mode 5 (rhombus point symbols). On the other hand, mode 7 is representative of structures that are mostly characterized by deterministic higher frequencies. Particularly, a peak is recognizable in the spectrum of the corresponding eigenvector (circle point symbols) that is linked to the characteristic shedding frequency of the separated shear layer, as described in details in Simoni et al. [104]. The frequency capturing similar energy in these two spectra has been chosen also in this case to distinguish between low and high frequency fluctuations. Similarly to the previous section, *low* and *high* frequency contributions to the modes have been considered in their computation by equation 4.24. Low frequency contributions allow isolating velocity fluctuations in the fore part of the bubble (figure 5.39). Particularly, vectors pointing upstream are clearly observable in the plots, suggesting that streaky structures may propagate in the separated boundary layer due to the high Tu level, according to the different amplification of streamwise

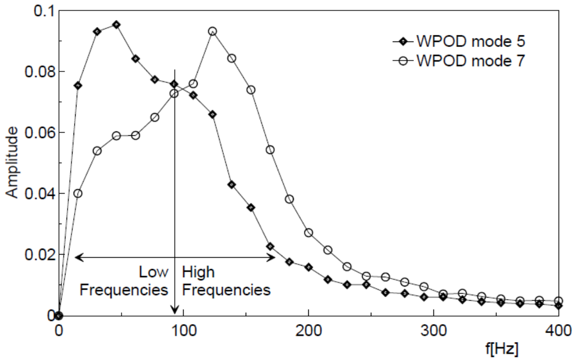

Fig. 5.38 FFTs of eigenvectors corresponding to the WPOD modes 5 (rhombus point symbols) and 7 (circle point symbols) of figure 5.37.

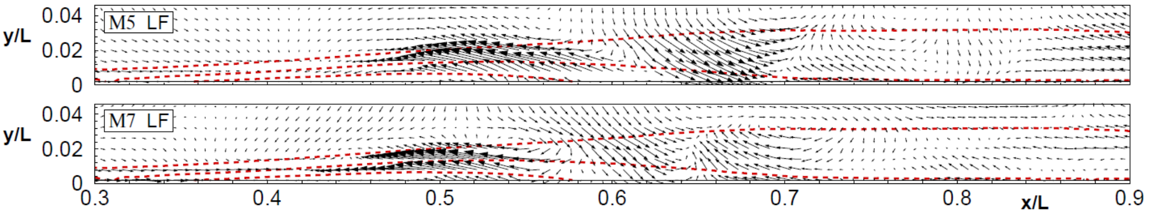

Fig. 5.39 Low frequency (LF) contributions to the WPOD modes 5 and 7. Mode number is indicated in the upper-left corner of each plot. Mean flow structure is highlighted by iso-contour lines of the mean velocity (red lines).

velocity fluctuations observed in the fore part of the bubble shown in figure 5.7 of section 5.1 (see also Yaras [45]). The role of streaky structures developing in the fore part of laminar separation bubbles in the transition of the separated shear layer has to be considered for the analysis of this kind of transition process, particularly under elevated free-stream turbulence. Note that a vortex is observable over the head of the sreaky struvture observed in the bottom plot of figure 5.39. On the other hand, the counter rotating vortices shown in the original modes downstream of $x/L = 0.6$ are not observable in these plots, being efficiently filtered

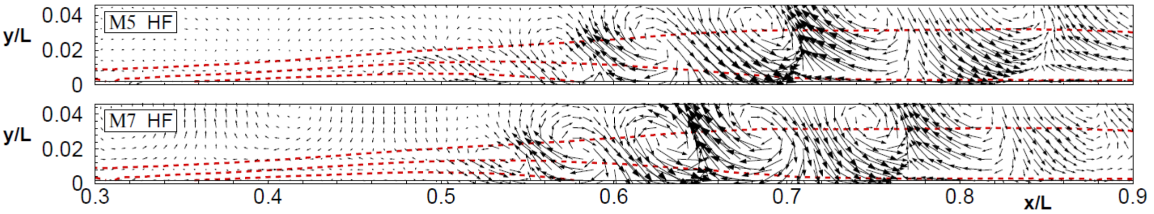

Fig. 5.40 High frequency (HF) contributions to the WPOD modes 5 and 7. Mode number is indicated in the upper-left corner of each plot. Mean flow structure is highlighted by iso-contour lines of the mean velocity (red lines).

by the procedure. Evidence of the shedding process are instead recognizable in figure 5.40, where only higher frequency contributions to the modes are used for their computation. In both plots coherent structures appear more organized than in the corresponding overall modes (compare figure 5.37 with figure 5.40). Additionally, high frequency contributions also highlight free-stream fluctuations in the bottom plot above the separated shear layer, thus sharing similarities with the results obtained for the attached flow configuration of the previous case. The Fourier based decomposition of the WPOD modes further highlights the coexistence of different dynamics characterize by different frequency content that affect the fore and the rear part of the laminar separation bubble.

5.3.3 Main findings

The application of the WPOD in the case of separation induced and by-pass transition beneath free-stream turbulence allowed the statistical characterization of the different dynamics taking part in the transition process in case of attached and separated flows. In this context, the WPOD constitutes a suitable tool to overcome the limit of the visual inspection of the instantaneous PIV snapshots, that do not provide a statistical characterization of the field at hand. Moreover, the capability of the WPOD procedure to capture structures characterized by different energy content within a single mode, constitutes a further improvement of the classical POD analysis in the study of the coexistence and possible interaction of these structures. In the case of by-pass transition, the occurrence of boundary layer streaks and less energetic free-stream vortices in the WPOD domain has been highlighted. The Fourier-empirical decomposition of the modes allowed isolating the low-frequency streaky structures from the high-frequency free-stream vortices. Interestingly, Q_2 events related to streak breakdown are characterized by the same frequency contributions characterizing free-stream vortices. Since the overall mode is obtained as the sum of these contributions, the coexistence of such structures is therefore made evident by the new procedure.

In the case of separated flow transition, the spatial normalization introduced in the WPOD procedure further highlighted velocity fluctuations in the fore part of the bubble. Low frequency contributions to the modes well isolate streaky-like structures upstream of the bubble maximum displacement that were not observed in section 5.1 by means of the visual inspection of the PIV snapshots presented in figure 5.8. On the other hand, higher frequencies have been found to be mostly related to the K-H rolls, originating downstream of the bubble maximum displacement position. Moreover, high frequency contributions to the modes also highlight the occurrence of free-stream structures at the edge of the separating boundary layer similar to those observed in the case of by-pass transition, thus showing similarities between these two different transition mechanisms.

5.4 Development of an accurate data base on transitional flows in variable pressure gradients

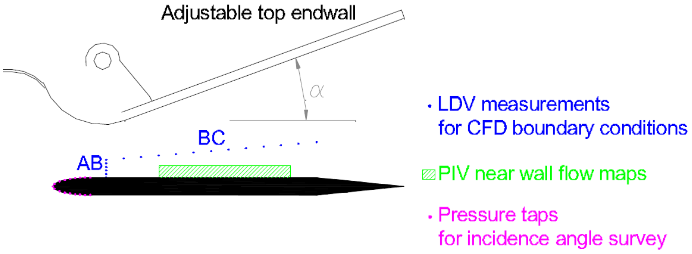

Fig. 5.41 Instrumentation layout

The need for a detailed characterization of the role of the pressure gradient variation in both attached and separated flow transition, led to a re-design of the test section adopted in the experimental analysis presented in the previous sections, where the effects of Re and Tu on the transition process were discussed for a fixed APG. The new test section equipped with adjustable endwalls (see figure 3.4) was designed to allow a continuous variation of the pressure gradient imposed to the flow from a geometrical zero pressure gradient condition, where the blockage effects induce a positive velocity gradient along the plate, up to the strong APGs typical of ultra high-lift profiles. The new test section so designed allows the extension and further validation of the results presented in the previous sections. The boundary layer evolution, as well as the freestream properties in terms of mean velocity and fluctuating velocity components have been acquired by means of the combined used of LDV and PIV instrumentation. This allowed the realization of a data set which can be adopted for the tuning and calibration of empirical correlations for the definition of transition related quantities and the development and testing of laminar-to-turbulent transition models.

The overall testmatrix spans 3 Reynolds numbers, 4 free-stream turbulence intensity levels and 4 pressure gradients. This large variation of flow parameters allows a gradual shift of the mode of transition from a by-pass process in attached flow, occurring with zero (Blasius like) and mild adverse pressure gradients at high free-stream turbulence, to separated flow transition, occurring with low Reynolds number, low free-stream turbulence intensity and elevated adverse pressure gradient.

5.4.1 Measurement techniques

Measurements were carried out in the variable area test section described in section 3.2 and reported here in figure 5.41 where the instrumentation layout is also highlighted. LDV and

TR-PIV have been adopted to provide high accuracy velocity and turbulence distributions characterizing the flat plate boundary layer and accurate boundary conditions requested by turbulence transport models. LDV guarantees high accuracy determination of the velocity and turbulence evolution in the free stream and the mean and statistical flow properties along a wall-normal line at the domain inlet. PIV gives a quick characterization of the boundary layer evolution in the rear part of the plate. The sketch reported in figure 5.41 provides an overall view of the instrumentation field of view and probe positions.

The boundary conditions have been acquired by means of LDV along the AB and BC lines, as ashown in figure 5.41. The AB line is located at $x/L = 0.19$ and covers different wall normal positions (from $y/L = 0$ till $y/L = 0.033$), while the BC line is inclined and extends from $x/L = 0.190$, $y/L = 0.033$ up to the end of the plate $x/L = 1$, $y/L = 0.133$, (see figure 5.41). 29 measuring points have been used on the AB line with the first one at a distance of 50 μm from the wall. A measuring point spacing of 50 μm has been adopted up to 1 mm from the wall, thus providing accurate flow and turbulence characterization near the wall. The BC line has been sampled with 13 equally spaced points in the streamwise direction. For each measuring point the acquisition period has been fixed to 120 s to ensure statistical convergence of the data. The data rate was of the order of 5 kHz away from the wall, and it reduces significantly in the region close to the wall due to wall reflection. Measurements have been carried out in coincidence mode, thus allowing also the evaluation of the Reynolds shear stress on both these lines.

The boundary layer developing along the rear part of the plate was surveyed by means of the DANTEC time resolved PIV system described in chapter 3. The measuring domain extends from around $x/L = 0.27$ to $x/L = 0.81$ (the test section throat is located at around $x/L = 0.19$). For each condition, eight independent sets of 2000 instantaneous velocity fields have been acquired at a sampling rate of 2 kHz. Thus, statistical moments have been computed processing 16000 PIV snapshots. The magnification factor and the cross-correlation window have been set to obtain a spatial resolution of $0.5 \times 0.5 mm^2$. Further details on the PIV arrangement and accuracy are provided by Simoni et al. [104].

5.4.2 Test matrix

Both LDV and PIV measurements have been carried out for each combination of the flow parameters. Particularly, three different adverse pressure gradients have been obtained by setting the opening angle of the endwalls to 12deg, 9deg and 5deg. A flat plate like condition (zero pressure gradient) has also been tested. For each opening angle, three different flow Reynolds numbers have been chosen: 70000, 150000 and 220000, based on the plate length

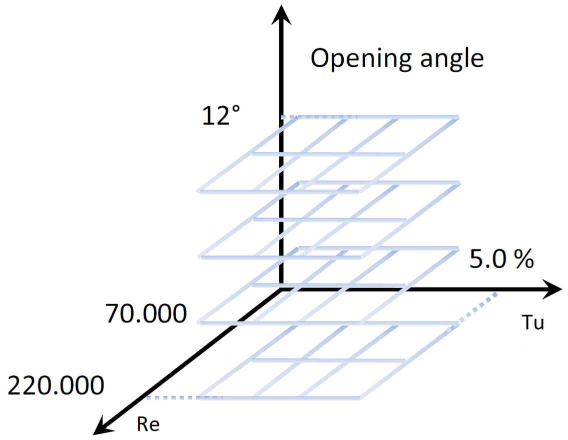

Fig. 5.42 Schematic representation of the test matrix

and the free-stream velocity at the plate leading edge. Different turbulence generating grids have been used in order to control and modify the Tu levels from 1.5% up to 5.0% (see table 3.1). It is worth noting that the grid Reynolds number has been kept constant for a chosen flow Reynolds number. The overall test matrix spans 48 different flow conditions. Figure 5.42 provides a schematic view of the design space spanned by the present experimental measuring campaign. Overall, 768000 velocity vector maps have been collected.

5.4.3 PIV nad LDV results: effects of Re, Tu and APG variation

In order to describe the effects of the parameter variation on the inflow boundary conditions, the time-mean velocity and velocity fluctuation rms profiles on the AB line are reported in figure 5.43. Data have been normalized with the free-stream velocity measured in the last point of the AB line. The case $Re = 70000$ with the smallest turbulence level ($Tu = 1.5\%$, NG in the plots) and 12deg opening angle is considered as the reference case. The velocity profile makes evident the laminar condition of the incoming boundary layer, and the free-stream velocity fluctuations appear only slightly amplified in the boundary layer (the peak value is around 2.5%). This peak is due to pre-transitional fluctuations, as discussed in the literature for relatively high free-stream turbulence intensity levels (Fransson et al [32]; Mandal et al [71]). Neither the Tu, nor the diffusion level significantly affect the shape of the velocity profile, even though the disturbances penetrating (and amplifying) into the boundary layer increase significantly for the highest turbulence intensity level (2.87%, HTU in the plots), reaching a peak of around 10%. The velocity profile appears instead mostly affected by the Reynolds number variation as expected (see the blue curve), while the pre-transitional activity growing into the boundary layer only marginally increases to a peak of around 3%.

The distribution of the time-mean velocity and the streamwise velocity fluctuation rms

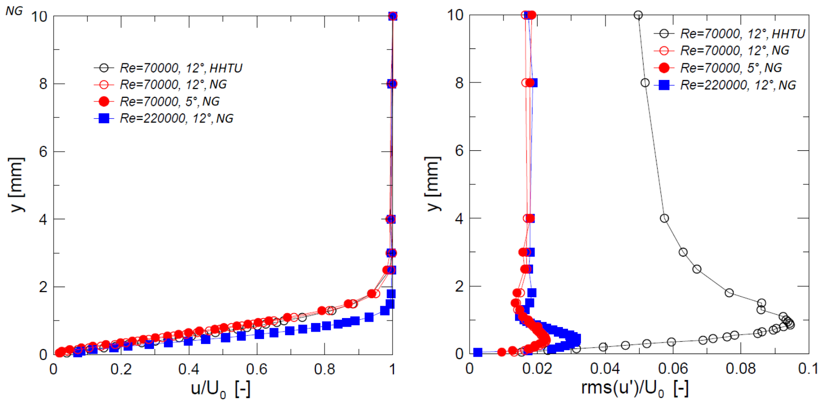

Fig. 5.43 Time-mean velocity (left) and velocity fluctuation root mean square (right) measured with LDV at $x/L = 0.2$.

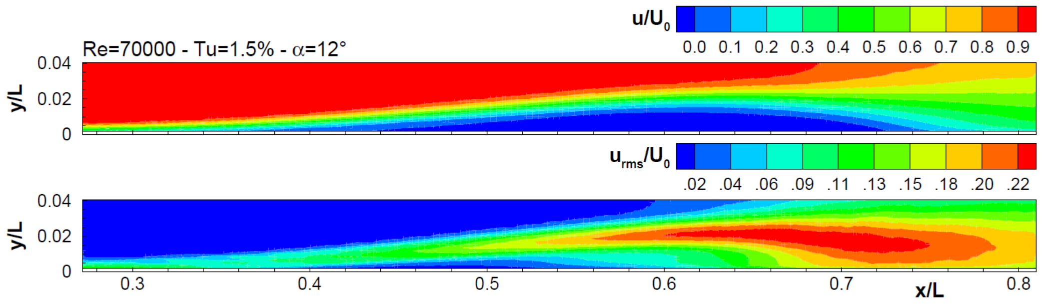

Fig. 5.44 Velocity and velocity rms contour plots for the reference case: $Re = 70000$, $Tu = 1.5\%$ and 12deg opening angle.

obtained by means of the PIV measurements for the reference case $Re = 70000$, $Tu = 1.5\%$ with 12deg opening angle are shown on figure 5.44. These plots provide the reference distributions for the further discussion of the effects of Re, Tu and APG variation on the time mean flow evolving on the flat plate. For the reference case, the boundary layer separates at around $x/L = 0.39$, while reattachment occurs around $x/L = 0.74$, in correspondence with the absolute maximum rms of velocity fluctuations, as highlighted also by Diwan and Ramesh [28]. Thus, a laminar separation bubble is formed as a consequence of the APG imposed to the flow and transition occurs in the separated shear layer inducing reattachment before the plate trailing edge. Velocity fluctuations are amplified along the separated shear layer, with a maximum level just downstream of the bubble maximum displacement position, where an intense vortex-shedding phenomenon is known to drive transition (see section 2.5.3). In the following, the effects of the variation of Re, Tu and APG will be presented. Particularly, each of these three parameters will be changed independently starting from the reference condition described above with the aim of highlighting the different flow configuration obtained as a

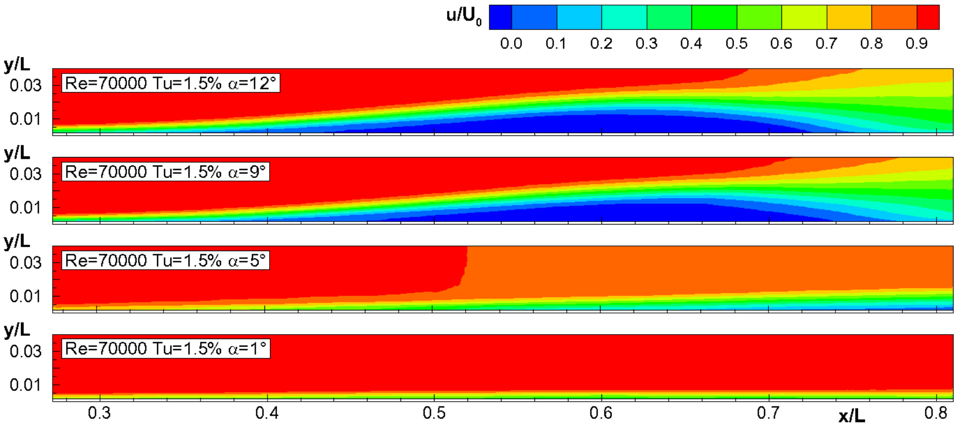

Fig. 5.45 APG effect on streamwise velocity distribution at Re=70000 and $Tu = 1.5\%$.

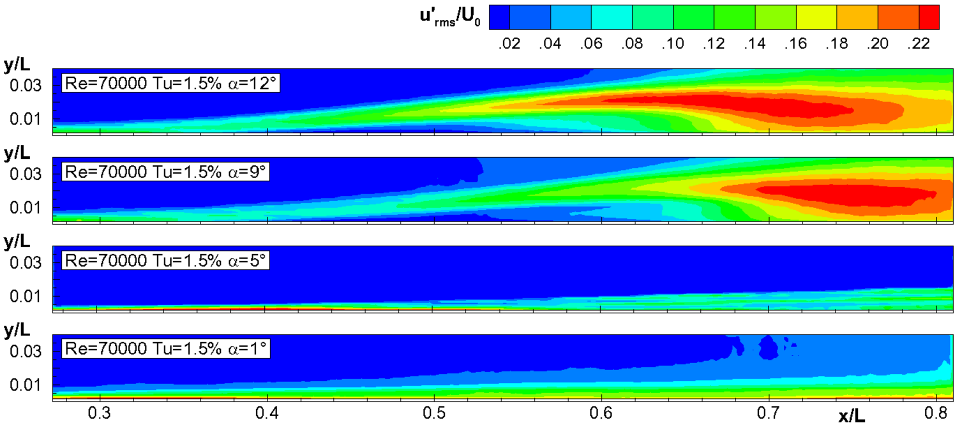

Fig. 5.46 APG effect on streamwise velocity fluctuations rms at Re=70000 and $Tu = 1.5\%$.

consequence of their variation.

In figures 5.45 and 5.46 the effects due to the variation of the pressure gradient imposed to the flow (i.e. opening angle α of the adjustable endwalls shown in figure 5.41) are presented in terms of both the mean streamwise velocity distribution and the rms of velocity fluctuations, respectively, for $\alpha = 12$, 9, 5 and 1 deg. Note that the opening angle of 1deg compensates the blockage effect due to the BL, thus this condition corresponds to a Blasius like condition. The flow Reynolds number and the Tu level have been kept the same of the reference condition, which is reported in the first plot for comparison. As the diffusion reduces, the separation position slightly moves in the downstream direction and the separation zone becomes longer (compare the velocity distributions for $\alpha = 12$ and $\alpha = 9$). This last effect is against intuition. The velocity fluctuation rms contour makes evident a delayed transition process into the separated shear layer for the 9deg case. Since velocity fluctuations

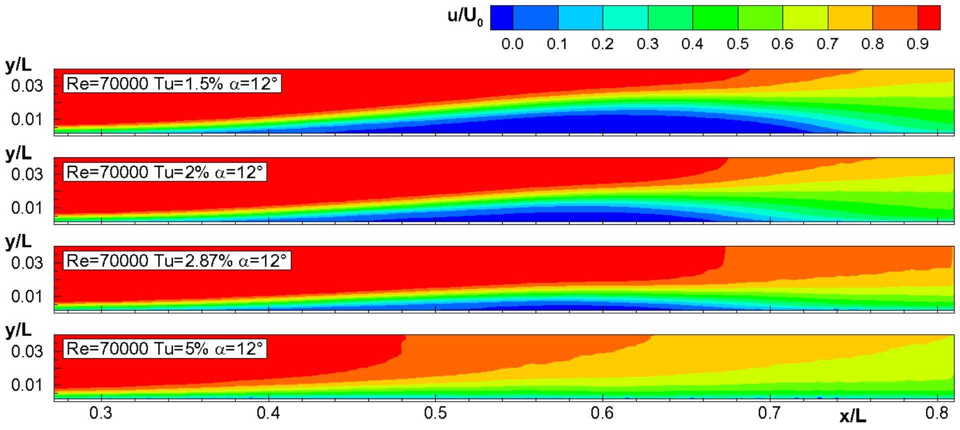

Fig. 5.47 Tu effect on streamwise velocity distribution at Re=70000 and 12deg opening angle.

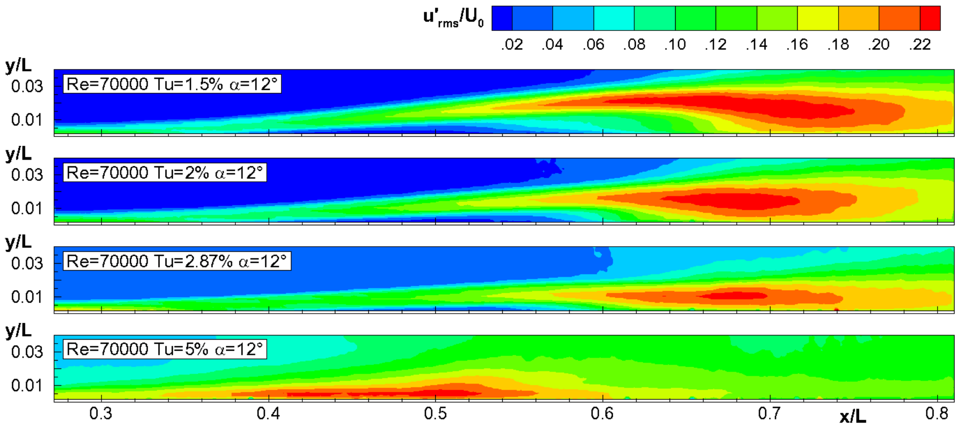

Fig. 5.48 Tu effect on streamwise velocity fluctuations rms at Re=70000 and 12deg opening angle.

penetrating into the boundary layer are practically unaffected by the diffusion level (see the LDV data shown in figure 5.43), it is argued that the variation of the shear layer thickness at the separation point is the main cause for the delayed transition. Indeed, the smaller the diffusion, the thicker the boundary layer at separation. According to the laminar separation criterion of Thwaites reported in equation (2.72), reducing the velocity gradient imposed to the flow, (i.e. reducing the acceleration parameter K) results in a higher momentum thickness Reynolds number at separation, that is, the BL separates downstream requiring a longer distance from the leading edge of the plate to reach the BL thickness imposed by the Thwaites's criterion. Moreover, a thicker BL at separation also results in a lower growth rate of velocity fluctuations amplified inside the separated shear layer, as highlighted in section

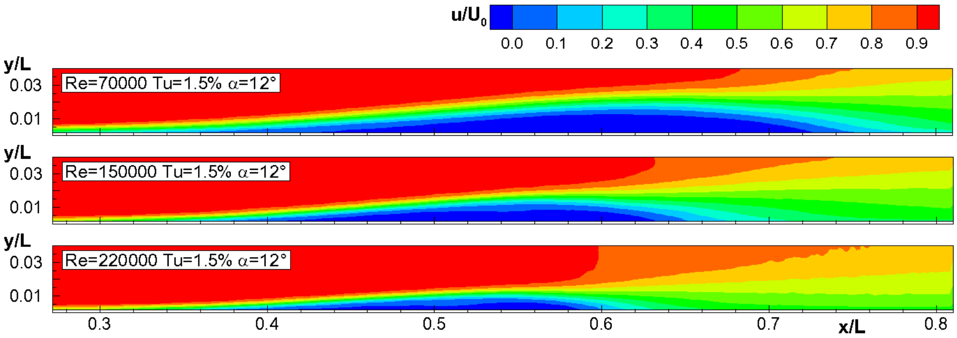

Fig. 5.49 Re effect on streamwise velocity distribution at Tu=1.5% and 12deg opening angle.

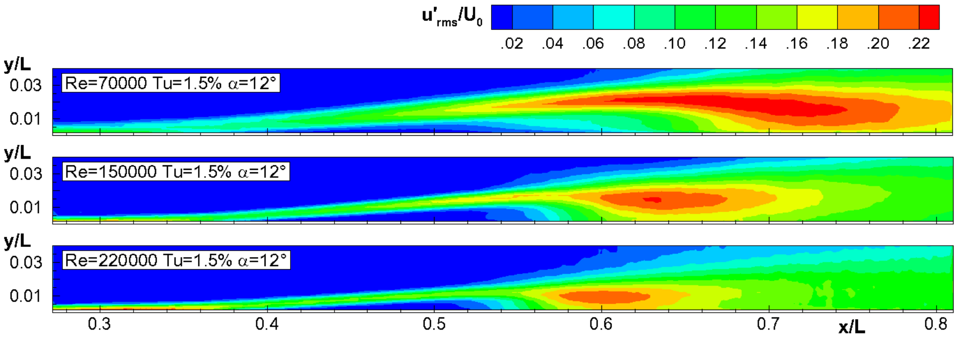

Fig. 5.50 Re effect on streamwise velocity fluctuations rms at Tu=1.5% and 12deg opening angle.

5.1 when discussing the effects of Re on the mean flow structure at separation. The typical dimensions of the K-H-vortices originating into the separated shear layer, driving the later stage of transition, also increase leading to a longer separated region (see Simoni et al. [107]). With a further reduction of the diffusion level (α = 5deg) the BL seems to separate just before the end of the measuring domain, while for the case $\alpha = 1$ the separation bubble is completely suppressed and for this low Re and Tu condition stays laminar up to the end of the measuring domain.

The effects due to the turbulence intensity variation (Tu = 1.5, 2, 2.87 and 5%), at fixed Reynolds number (Re = 70000) and diffusion level ($\alpha = 12$ deg) with respect to the reference condition, are illustrated in figure 5.47 and 5.48 in terms of streamwise velocity component and velocity fluctuation rms, respectively. The turbulence level increases from top to bottom in these plots. As expected, the higher the free-stream turbulence intensity level the shorter the separated flow region. Moreover, the laminar separation bubble appears evidently thinner, until separation is suppressed for the case Tu = 5%. The inspection of the fluctuating velocity distributions makes evident that this is mainly due to a larger penetration of free-stream disturbances into the attached boundary layer, as highlighted in section 5.1 and also confirmed by the LDV results on the AB line previously shown (see figure 5.43). Otherwise, the shear layer thickness at separation for the separated cases ($Tu < 5\%$) is substantially the same of the reference condition. This still confirms that the earlier transition in the separated shear layer is due to a larger penetration of disturbances that develop into a similar separating boundary layer, since no significant variation of the mean flow structures is observed upstream of the separation position. For the highest free-stream turbulence level, the transition process shifts from a separation type to a by-pass type. The peak in the velocity fluctuations rms (figure 5.48) is now more confined to the near wall region, as it typically occurs in the case of by-pass transition. The growing and consequent decrease of velocity fluctuation rms indicate that transition occurs before the end of the measuring domain, thus allowing a complete characterization of the by-pass transition process for this set of parameters.

In figures 5.49 and 5.50 the effects due to the variation of the flow Reynolds number (Re = 70000, 150000 and 220000) at the constant turbulence level Tu = 1.5% and high diffusion (12deg opening angle) are illustrated for both the time mean streamwise velocity and rms of velocity fluctuation. The separation position is only slightly affected by the Re number variation (the same is for the Tu variation). The Reynolds number variation induces similar effects on the bubble length to what was observed by the variation of the Tu level. Indeed, the higher the Reynolds number the shorter and thinner the separated flow region. However, in this case the separation bubble reduction is clearly due to a different mechanism. Namely, the higher the Reynolds number the thinner the separating boundary layer (see figure 5.49 at $x/L < 0.39$) and consequently the separated shear layer thickness that, as discussed in previous sections, directly affects the dimension of the large scale K-H vortices shed downstream of the bubble maximum displacement position. On the other hand, penetration of disturbances into the separating boundary layer is only marginally affected by the Re number variation, as highlighted by both the rms distributions of figure 5.50 and the LDV velocity data (figure 5.43). This confirms the results found in section 5.1. Note that for the case Re = 220000 a LSB still occurs as a consequence of the combined effects of the strong APG imposed to the flow ($\alpha = 12$deg) and the low Tu level. Increasing the Tu level for the same Reynolds number will progressively lead to the occurrence of a by-pass type transition. Indeed, for each Reynolds number and APG imposed to the flow, the highest Tu level (Tu = 5%) always induces the occurrence of an attached flow over the plate, allowing the characterization of the by-pass transition process for different Re and APG.

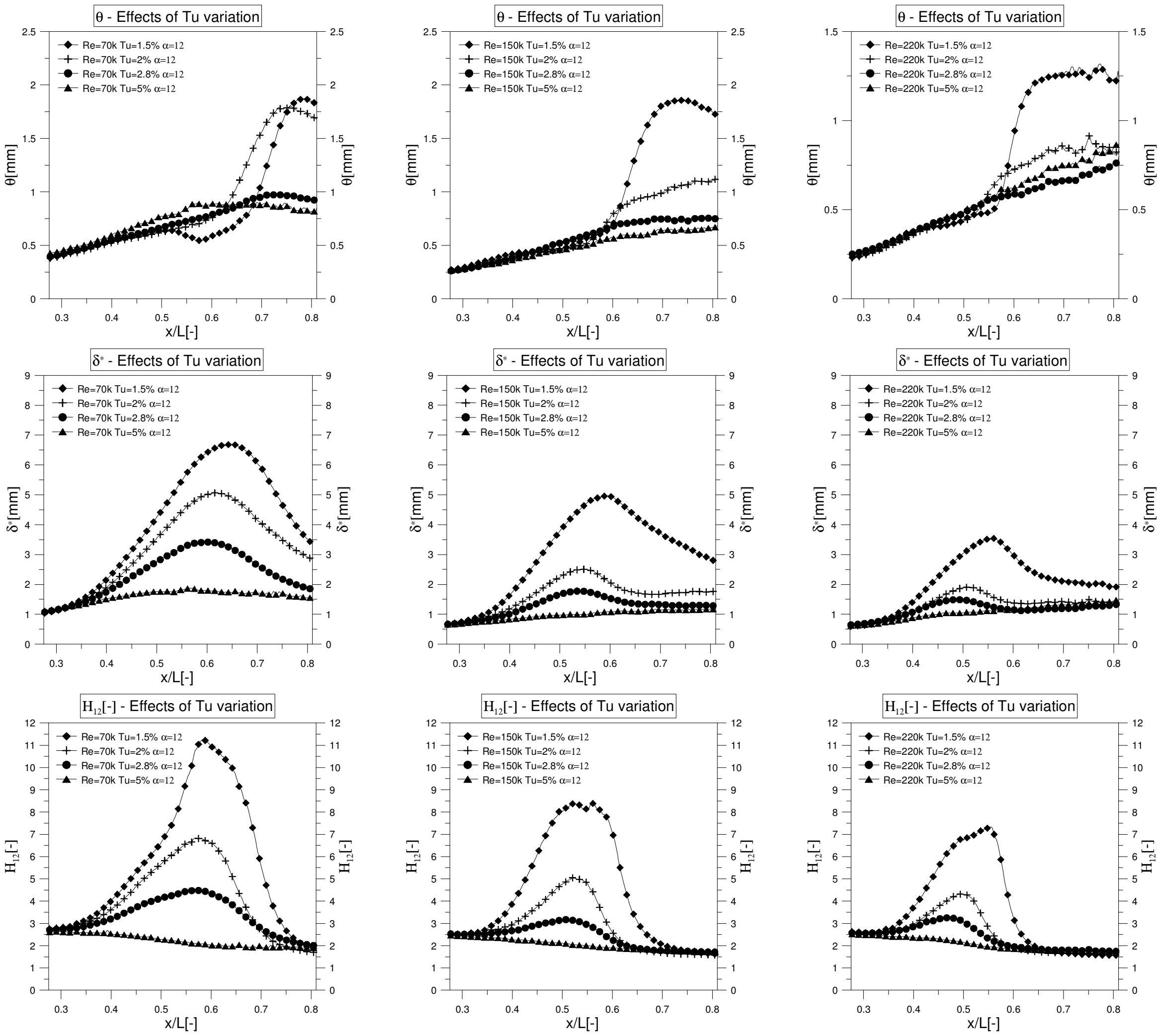

Fig. 5.51 BL integral parameters at $\alpha = 12$deg for varying Re and Tu level.

5.4.4 BL integral parameters: Time mean response of LSB

In this section the effects of the Re, Tu and APG variation will be discussed looking at the distributions of the main boundary layer integral parameters (δ^*, θ and H_{12}), which were computed for each condition tested. The boundary layer displacement thickness δ^*, the momentum thickness θ and the shape factor H_{12} have been computed and plotted with respect to the normalized streamwise coordinate in order to detect the characteristic positions of the laminar separation bubbles occurring for the higher pressure gradients ($\alpha \neq 1$). As previously highlighted in section 2.3, the peaks of δ^* and H_{12} provide information about the bubble maximum displacement and transition onset positions, respectively. Moreover, the distribution of the momentum thickness for the different cases allows the computation of the Reynolds number based on the momentum thickness at separation $Re_{\theta,s}$, which appears in

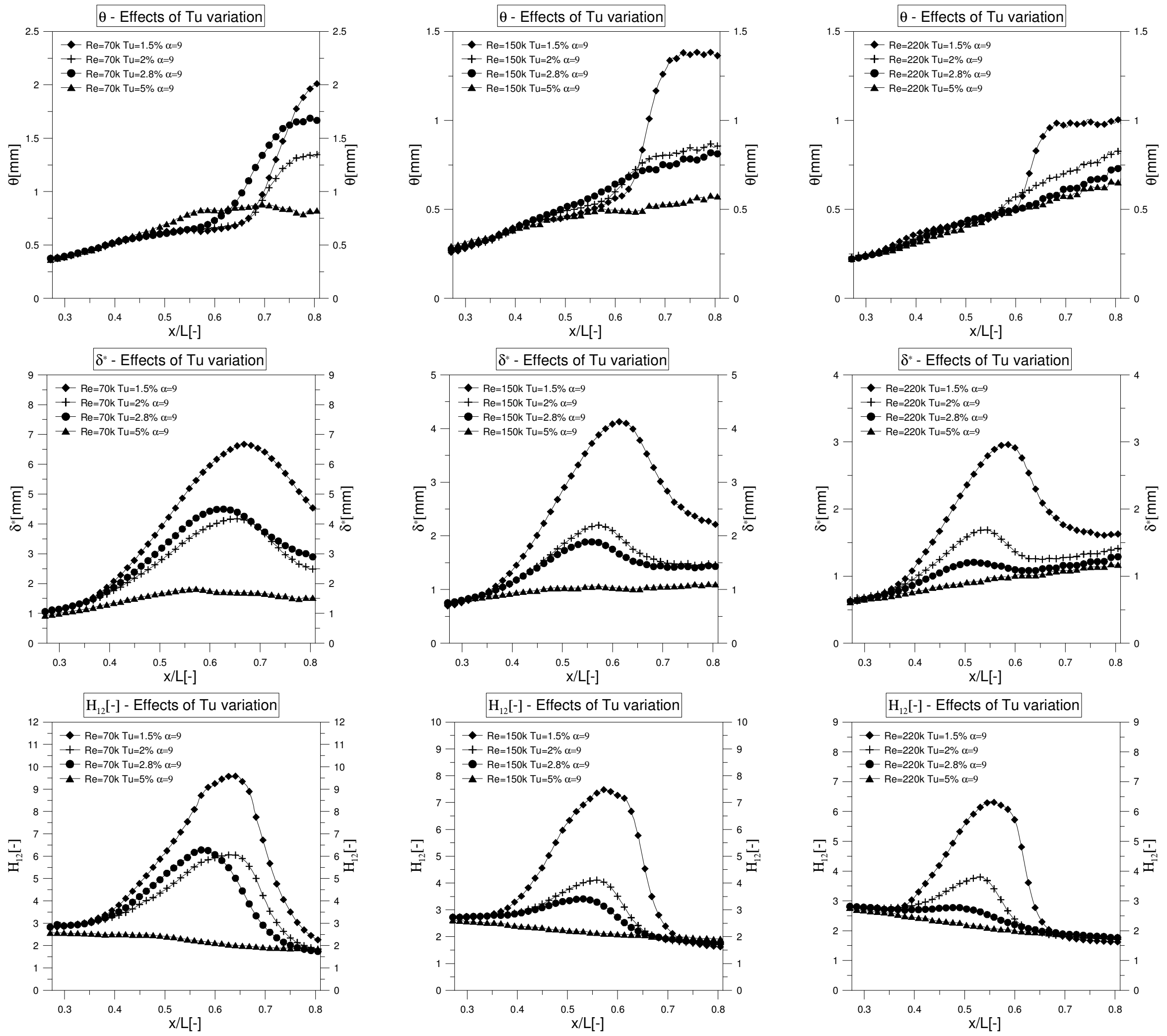

Fig. 5.52 BL integral parameters at $\alpha = 9$deg for varying Re and Tu level.

the experimental correlations available in literature for the characterization of the separated flows transition in turbomachinery applications (see e.g., Mayle [80]). The plots reported in figure 5.51, 5.52 and 5.53 show the distribution of the three integral parameters mentioned above for the opening angle 12, 9 and 5 deg, respectively. The condition $\alpha = 1$deg is not shown since due to the thin BL thickness obtained in this condition and the consequent reduction of spatial resolution, the BL integral parameters cannot be computed. In each figure, the cross effects of Re and Tu are presented. The distributions of δ^* highlight the reduction of the bubble length as a consequence of the increasing of the Tu level and Re for a fixed APG. More precisely, since the position of the maximum δ^* is known to correspond to the position of the bubble maximum displacement, what shown in figure 5.51, 5.52 and 5.53 confirms that the reduction of the bubble length is due to the anticipation of the bubble

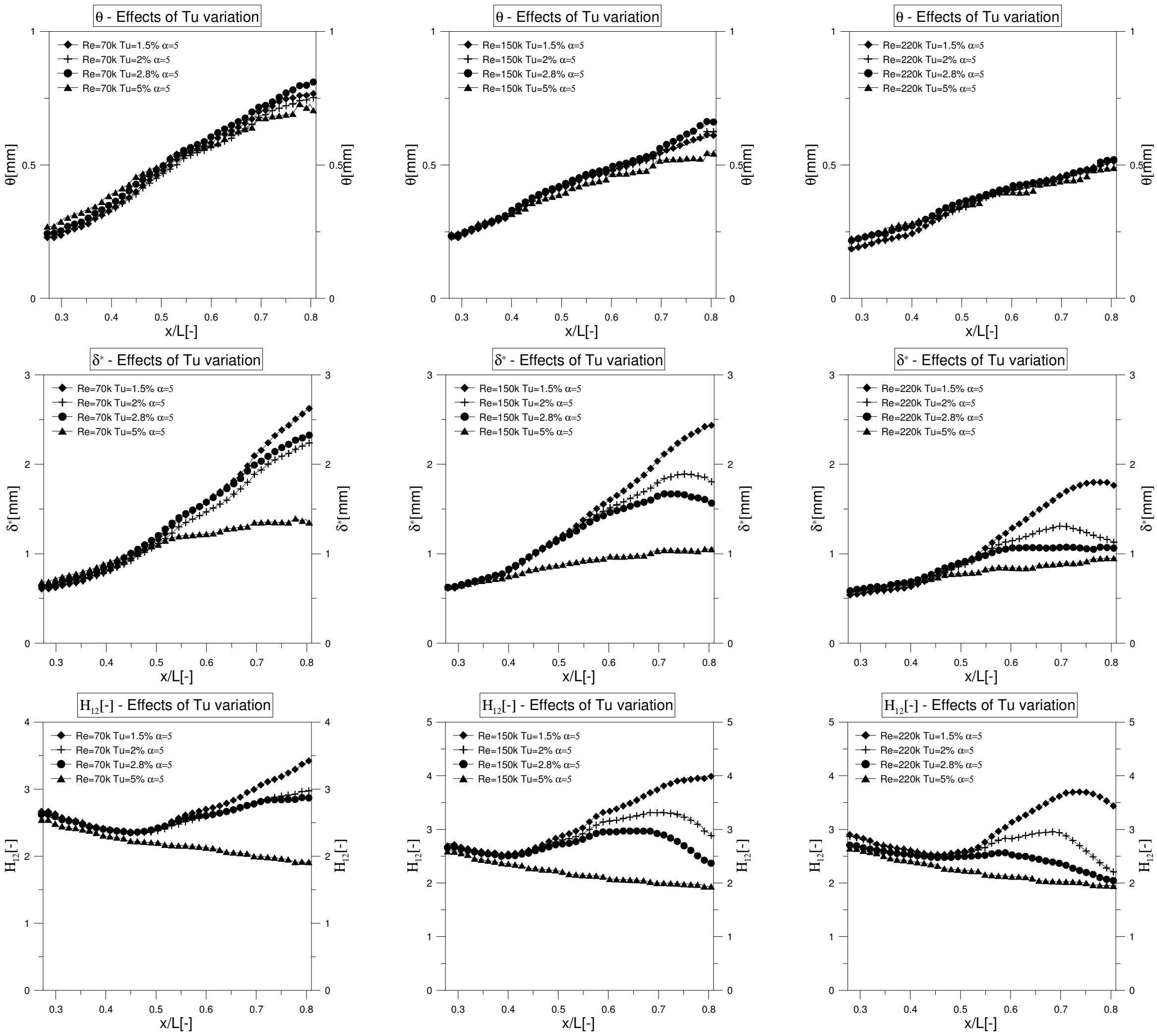

Fig. 5.53 BL integral parameters at $\alpha = 5$deg for varying Re and Tu level.

maximum displacement. Moreover, the peak of H_{12} is always located upstream of the bubble maximum displacement, indicating that the transition starts upstream of this position for all the condition tested.

The data presented here are suitable for a statistical characterization of the time mean structure of the LSB depending on the inflow conditions. More precisely, the length between the separation position and the transition onset with respect also to the bubble maximum displacement position can be characterized for the large variation of Re, Tu and APG considered. Additionally, once provided the reattachment position as the location where the maximum rms of velocity fluctuation occurs, one can obtained a simplified description of the mean structure of the LSB from the separation position up to the reattachment one. From this perspective, the reduction of all the data collected in this work could allow the prediction of

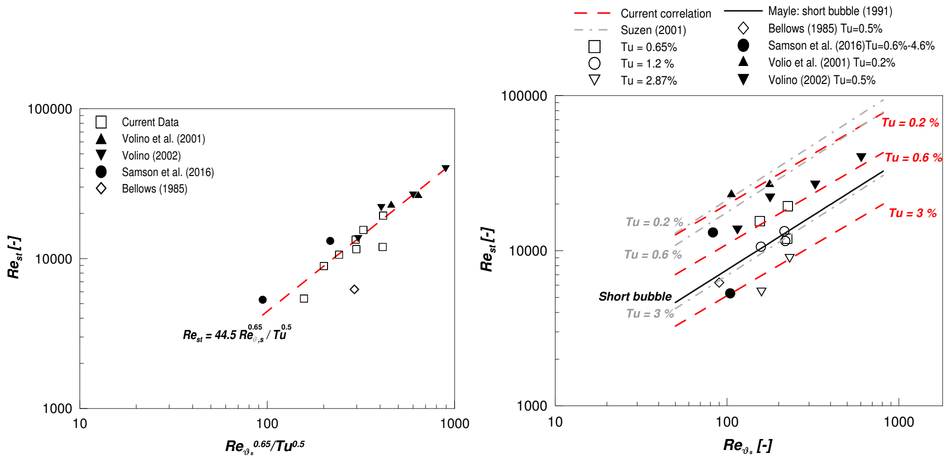

Fig. 5.54 (left) Dispersion of the transition onset Reynolds number Re_{st} as a function of the new defined variable $Re_{\theta_s}^{0.65}/Tu^{0.5}$. (right) Comparison between fitting curves obtained from the correlations of Mayle [80] (black line), Suzen at al. [113] (gray lines) and from eq. 5.3 (red lines).

the LSB structure starting from global parameters computed at the separation location (e.g. Re_θ at separation, K).

5.4.5 Correlations for the prediction of the transition process in case of seprated flows

Thanks to the extensive experimental database collected, the characteristic positions mentioned above have been measured for both short and long LSBs observed for different inflow conditions, together with the flow parameters providing the characterization of the pressure gradients imposed to the flow (i.e. K and λ_θ). Since few correlations for the prediction of the transition process in case of separated flows are available in literature, new empirical correlations for the prediction of the transition onset (expressed as the Reynolds number based on the length st between the separation and transition onset positions, Re_{st}) and the transition length L (expressed in terms of the corresponding Reynolds number Re_L) as a function of the Tu level and the momentum thickness Reynolds number Re_θ have been proposed and validated for different APGs.

For what concerns the transition onset location, it has been observed that the higher the Tu, the shorter the LSB due to the anticipation of the transition onset (i.e. the maximum peak of the shape factor H_{12} moves upstream). Moreover, the thicker the BL at separation (i.e. the higher θ) the longer the bubble. According to these observations highlighted by the results presented in the previous sections, the following guest function for the transition

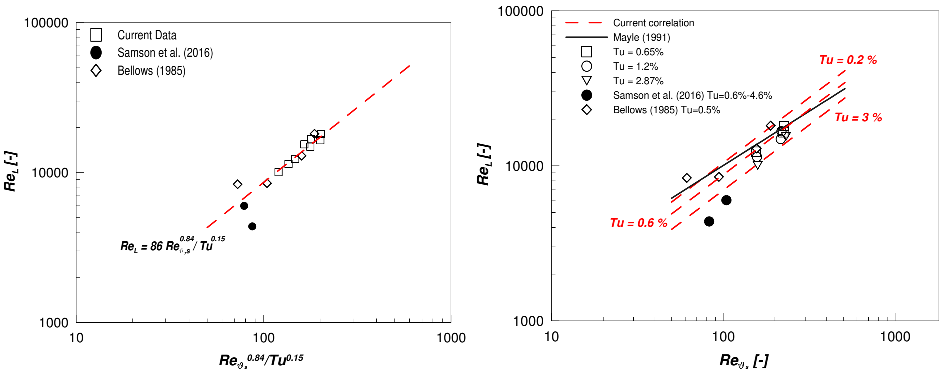

Fig. 5.55 (left) Dispersion of the transition length Reynolds number Re_L as a function of the new defined variable $Re_{\theta_s}^{0.84}/Tu^{0.15}$. (right) Comparison between fitting curves obtained from the correlation of Mayle [80] (black line) and from eq. 5.4 at different Tu levels (red lines).

onset is proposed here to fit the experimental data collected:

$$Re_{st} = C\frac{Re_{\theta_s}^n}{Tu^m} \tag{5.3}$$

where the best fitting has been obtained for $C = 44.5$, $n = 0.65$ and $m = 0.5$. The accuracy of the empirical correlation can be observed in figure 5.54 (left plot) , as made evident by the small dispersion of the experimental data around the straight line representing the dependency between Re_{st} and the proposed combined variable $Re_{\theta_s}^{0.65}/Tu^{0.5}$. The right plot of figure 5.54 highlights the importance to take into account for the Tu effects. Note that the exponent of the momentum thickness Reynolds number is close to that proposed by Mayle in his correlations for both short and long bubble types (Re_{st} proportional to $Re_{\theta_s}^{0.7}$).

The correlation predicting the transition length, evaluated as the distance between the transition onset and end positions, should account for the dependence of the amplification rate of velocity fluctuation on the flow Reynolds number (see section 5.1). The transition length has been directly obtained from the PIV measurements by means of a wavelet based procedure not discussed here (see [103] for further details). According to what described in the previous sections, the transition length reduces as the Reynolds number increases (acting reducing the BL thickness at separation) and it is only marginally affected by the Tu level. The fitting curve here proposed has the same structure of equation (5.3), viz:

$$Re_L = D\frac{Re_{\theta_s}^h}{Tu^k} \tag{5.4}$$

with $D = 86$, $h = 0.84$ and $k = 0.15$. The low value of the Tu exponent ($k = 0.15$) makes further evident the reduced weight of the turbulence intensity on the transition length as compared with the effects due to the Reynolds number variation. Also in this case the ability of the proposed correlation to correctly predict the transition length is confirmed by the narrow cloud of experimental data distributed very close to the straight line plotted in figure 5.55, excepted for one element of the ensemble taken from the Samson and Sarkar's experiments [95]. The introduction of the turbulence intensity provides an improved ability to reproduce the experimental trend if compared with the correlation proposed by Mayle for the transition length in separated flows (see the right plot of figure 5.22).

5.4.6 Main findings

In the present section an extensive data base describing attached and separated transitional boundary layers was presented. The overall test matrix spans 48 different combinations of Reynolds numbers, diffusion and Tu levels. For each condition, LDV data provide the velocity and turbulence profiles at the entrance of the investigated area. The PIV data provide the velocity and turbulence distributions describing the transitional boundary layers. Moreover, the correlations presented into the present section allow predicting the main parameters of the separated flow transition process: transition onset and end positions. These correlations account for the dominant mechanisms driving the separated flow transition process from the linear stage of transition up to the non linear part leading to the fully turbulent condition of the boundary layer.

Chapter 6

Conclusions

A large amount of experimental data concerning with attached and separated flows have been collected. The effects due to the variation of the Reynolds number, the Tu level and the adverse pressure gradient imposed to the flow have been characterized in details in terms of both the time-mean and the dynamic response of the transition process, by means of PIV, LDV and Hot-Wire instrumentation.

The time-mean results provided an overall view of the boundary layer response to a large variation of all the inflow parameters (Re, Tu, APG), for either short and long bubbles and attached flow. In case of laminar separation, the Tu level has been found to marginally affect the time-mean flow structure at separation. Similarly, the growth rate of the velocity fluctuations amplified inside the separated BL has been found to be only marginally affected by the Tu variation for each Reynolds number and pressure gradient tested. Thus, the bubble length and height reduction at high Tu levels at fixed Reynolds number and APG are due only to the higher amplitude of velocity fluctuations penetrating into the separating boundary layer. Conversely, Reynolds number significantly influences the time-mean boundary layer structure at separation. This translates into different disturbance growth rate and dynamic properties of the shedding phenomenon, even though the saturation level of velocity fluctuations has been found to be unaffected by the Tu level, Re and APG variations.

Even though the separation position has been found to be only marginally affected by Re and Tu level, a variation of the APG imposed to the flow results in a shift of the separation position. More precisely, the separation position moves downstream when the APG imposed to the flow is reduced and the bubble becomes longer. Indeed, due to the shift of the detachment position, the BL at separation becomes thicker and a lower amplification rate of the disturbances inside the separated shear layer is observed, thus a longer bubble occurs. However, even if the bubble is longer at lower APGs, the bubble thickness is reduced with respect to the higher APGs conditions, thus the viscous effects on the potential flow are reduced.

The analysis of the streamwise distributions of the BL integral parameters and the local maximum rms of velocity fluctuations in case of separated flows revealed that the peaks of the H_{12} and δ^* distributions occur in correspondence with the transition onset and maximum displacement position, respectively. Indeed, the peak of H_{12} has been found to occur at the same position where the rms of the normal to the wall velocity fluctuations starts to be exponentially amplified and a change in the amplification rate of the streamwise velocity fluctuations occurs. This means that the maximum of H_{12} occurs in correspondence with the K-H instabilities onset, which are known to drive the transition process in laminar separation bubbles. Moreover, the maximum value of H_{12} has been found to occur upstream of the maximum δ^* position for each condition, thus the transition of the separated shear layer always starts upstream of the maximum displacement position.

In case of attached flows, the integral parameters and the intermittency function computed by means of the PIV data revealed that the onset of transition can be identified also in this case in correspondence with the peak of H_{12}. Moreover, in case of adverse pressure gradient imposed to the flow, the transition is rapid and H_{12} reaches the equilibrium level sensibly after the transition end, differently from the zero pressure gradient case. The profiles of the mean streamwise velocity and velocity fluctuations rms obtained by the Hot-Wire data showed a self-similar behavior in the laminar part of the boundary layer. In this case, the momentum thickness resulted the best scaling quantity. Interesting, the high free-stream turbulence acts reducing the effects of the pressure gradient on the curvature of the mean velocity profile and shifting the maximum of the turbulence peak towards the wall with respect to a flat plate boundary layer perturbed by streaky structures.

The analysis of the PIV data collected in case of both separated and attached flows by means of the proposed Weighted-POD procedure highlighted similarities between separated and attached flow transition. Particularly, due to the possibility to capture structures characterized by different energy content (i.e. free-stream vortices, BL streaks and K-H vortices) within a single mode, the occurrence of counter rotating free-stream vortices has been observed near the edge of the BL in case of both attached and separated flows, showing similarities. Moreover, streaky like structures were observed in the fore part of laminar separation bubble in case of high Tu levels, suggesting that they can participate to the transition process promoting the K-H instability onset.

References

[1] Abu-Ghannam, B. and Shaw, R. (1980a). Natural transition of boundary layers—the effects of turbulence, pressure gradient, and flow history. *Journal of Mechanical Engineering Science*, 22(5):213–228.

[2] Abu-Ghannam, B. and Shaw, R. (1980b). Natural transition of boundary layers—the effects of turbulence, pressure gradient, and flow history. *Journal of Mechanical Engineering Science*, 22(5):213–228.

[3] Adrian, R. J. (2007). Hairpin vortex organization in wall turbulence. *Phys. Fluids*, 19:041301–1–041301–16.

[4] Alam, M. and Sandham, N. (2000). Direct numerical simulation of 'short' laminar separation bubbles with turbulent reattachment. *J. Fluid Mech.*, 410:1–28.

[5] Anderson, J. D. (2005). Ludwig prandtl's boundary layer. *Physics Today*, 58(12):42–48.

[6] Anderson Jr, J. D. (2010). *Fundamentals of aerodynamics*. Tata McGraw-Hill Education.

[7] Andersson, P., Berggren, M., and Henningson, D. S. (1999). Optimal disturbances and bypass transition in boundary layers. *Physics of Fluids*, 11(1):134–150.

[8] Andersson, P., Brandt, L., Bottaro, A., and Henningson, D. S. (2001). On the breakdown of boundary layers streaks. *J. Fluid Mech.*, 428:29–60.

[9] Arndt, R. E., Long, D., and Glauser, M. (1997). The proper orthogonal decomposition of pressure fluctuations surrounding a turbulent jet. *Journal of Fluid Mechanics*, 340:1–33.

[10] Blasius, H. (1908). The boundary layers in fluids with little friction. *Z. Math. Phys.*, 56(1).

[11] Borée, J. (2003). Extended proper orthogonal decomposition: a tool to analyse correlated events in turbulent flows. *Experiments in fluids*, 35(2):188–192.

[12] Boutilier, M. S. and Yarusevych, S. (2012). Parametric study of separation and transition characteristics over an airfoil at low reynolds numbers. *Experiments in fluids*, 52(6):1491–1506.

[13] Bradt, L., Schlatter, F., and Henningson, D. S. (2004). Transition in boundary layers subject to free-stream turbulence. *J. Fluid Mech.*, 517:167–198.

[14] Brandt, L. and Henningson, D. S. (2002). Transition of streamwise streaks in zero-pressure gradient boundary layers. *J. Fluid Mech.*, 472:229–261.

[15] Burgmann, S., Brücker, C., and Schröder, W. (2006). Scanning PIV measurements of a laminar separation bubble. *Exp. Fluids*, 41:319–326.

[16] Burgmann, S. and Schröder, W. (2008). Investigation of the vortex induced unsteadiness of a separation bubble via time-resolved and scanning piv measurements. *Experiments in fluids*, 45(4):675.

[17] Burgmann, S. and Schröder, W. (2008). Investigation of the vortex induced unsteadiness of a separation bubble via time-resolved and scanning PIV measurements. *Exp. Fluids*, 45:675–691.

[18] Butler, K. M. and Farrell, B. F. (1992). Three-dimensional optimal perturbations in viscous shear flow. *Physics of Fluids A: Fluid Dynamics*, 4(8):1637–1650.

[19] Butler, R. J., Byerley, A. R., VanTreuren, K., and Baughn, J. W. (2001). The effect of turbulence intensity and length scale on low-pressure turbine blade aerodynamics. *International journal of heat and fluid flow*, 22(2):123–133.

[20] Citriniti, J. and George, W. K. (2000). Reconstruction of the global velocity field in the axisymmetric mixing layer utilizing the proper orthogonal decomposition. *Journal of Fluid Mechanics*, 418:137–166.

[21] Corbett, P. and Bottaro, A. (2000). Optimal perturbations for boundary layers subject to stream-wise pressure gradient. *Physics of Fluids*, 12(1):120–130.

[22] Currie, I. (1974). Fundamental mechanics of fluids. *&*, 41:40.

[23] Curtis, E., Hodson, H., Banieghbal, M., Denton, J., Howell, R., and Harvey, N. (1997). Development of blade profiles for low-pressure turbine applications. *Journal of Turbomachinery*, 119(3):531–538.

[24] Dabiri, D. (2006). Cross-correlation digital particle image velocimetry—a review. *Turbul. ABCM Curitiba*, 155:199.

[25] Dhawan, S. and Narasimha, R. (1958). Some properties of boundary layer flow during the transition from laminar to turbulent motion. *Journal of Fluid Mechanics*, 3(4):418–436.

[26] Dick, E. and Kubacki, S. (2017). Transition models for turbomachinery boundary layer flows: A review. *International Journal of Turbomachinery, Propulsion and Power*, 2(2):4.

[27] Diwan, S. S. and Ramesh, O. (2009a). On the origin of the inflectional instability of a laminar separation bubble. *J. Fluid Mech*, 629:263–298.

[28] Diwan, S. S. and Ramesh, O. N. (2009b). On the origin of the inflectional instability of a laminar separation bubble. *Journal of Fluid Mechanics*, 629:263–298.

[29] Dovgal, A., Kozlov, V., and Michalke, A. (1994). Laminar boundary layer separation: Instability and associated phenomena. *Prog. Aerospace Sci.*, 30:61–94.

[30] Dunham, J. (1972). Prediction of boundary layer transition on turbomachinery blades. In *AGARD meeting on boundary layers in turbomachines, 1972*.

[31] Emmons, H. W. (2012). The laminar-turbulent transition in a boundary layer-part i. *Journal of the Aeronautical Sciences*.

[32] Fransson, J. H., Matsubara, M., and Alfredsson, P. H. (2005). Transition induced by free-stream turbulence. *Journal of Fluid Mechanics*, 527:1–25.

[33] Gaster, M. (1966). The structure and behaviour of laminar separation bubbles. *AGARD*, CP4 Part2:813–854.

[34] Glauser, M. and George, W. (1987). Orthogonal decomposition of the axisymmetric jet mixing layer including azimuthal dependence. In *Advances in turbulence*, pages 357–366. Springer.

[35] Glauser, M. N. and George, W. K. (1992). Application of multipoint measurements for flow characterization. *Experimental Thermal and Fluid Science*, 5(5):617–632.

[36] Gostelow, J., Blunden, A., and Walker, G. (1992). Effects of free-stream turbulence and adverse pressure gradients on boundary layer transition. In *ASME 1992 International Gas Turbine and Aeroengine Congress and Exposition*, pages V001T01A128–V001T01A128. American Society of Mechanical Engineers.

[37] Göttlich, E. (2011). Research on the aerodynamics of intermediate turbine diffusers. *Progress in Aerospace Sciences*, 47(4):249–279.

[38] Häggmark, C. P. (2000). Investigations of disturbances developing in a laminar separation bubble flow. *KTH Stockholm, Department of Mechanics, Diss.*

[39] Häggmark, C. P., Hildings, C., and Henningson, D. S. (2001). A numerical and experimental study of a transitional separation bubble. *Aerospace science and technology*, 5(5):317–328.

[40] Hain, R., Kähler, C. J., and Radespiel, R. (2009). Dynamics of laminar separation bubbles at low-Reynolds- number aerofoils. *J. Fluid Mech.*, 630:129–153.

[41] Hall, D. and Gibbings, J. (1972). Influence of stream turbulence and pressure gradient upon boundary layer transition. *Journal of Mechanical Engineering Science*, 14(2):134–146.

[42] Halstead, D. E., Wisler, D. C., Okiishi, T., Walker, G. J., Hodson, H. P., and Shin, H. W. (1997). Boundary layer development in axial compressors and turbines: Part 1 of 4-composite picture. *ASME J. of Turbomach.*, 119:114–127.

[43] Hatman, A. and Wang, T. (1999). A prediction model for separated-flow transition. *Journal of Turbomachinery*, 121(3):594–602.

[44] Högberg, M. and Henningson, D. S. (2002). Linear optimal control applied to instabilities in spatially developing boundary layers. *Journal of Fluid Mechanics*, 470:151–179.

[45] Istvan, M. S. and Yarusevych, S. (2018). Effects of free-stream turbulence intensity on transition in a laminar separation bubble formed over an airfoil. *Experiments in Fluids*, 59(3):52.

[46] Jacob, R. G. and Durbin, P. A. (2001). Simulations of bypass transition. *J. Fluid Mech.*, 428:185–212.

[47] Jones, L., Sandberg, R., and Sandham, N. (2008). Direct numerical simulations of forced and unforced separation bubbles on an airfoil at incidence. *Journal of Fluid Mechanics*, 602:175–207.

[48] Kähler, C. J., Scharnowski, S., and Cierpka, C. (2012). On the resolution limit of digital particle image velocimetry. *Experiments in fluids*, 52(6):1629–1639.

[49] Klebanoff, P. S. (1955). Characteristics of turbulence in boundary layer with zero pressure gradient. *NACA-REPORT*, 1247.

[50] Kubacki, S. and Dick, E. (2016). An algebraic intermittency model for bypass, separation-induced and wake-induced transition. *International Journal of Heat and Fluid Flow*, 62:344–361.

[51] Kurelek, J. W., Lambert, A. R., and Yarusevych, S. (2016). Coherent structures in the transition process of a laminar separation bubble. *AIAA Journal*, 54:2295–2309.

[52] Kurian, T. and Fransson, J. H. (2009). Grid-generated turbulence revisited. *Fluid dynamics research*, 41(2):021403.

[53] Lang, M., Marxen, O., Rist, U., and Wagner, S. (2004a). A combined numerical and experimental investigation of transition in a laminar separation bubble. In *Recent Results in Laminar-Turbulent Transition*, pages 149–164. Springer.

[54] Lang, M., Rist, U., and Wagner, S. (2004b). Investigations on controlled transition development in a laminar separation bubble by means of LDA and PIV. *Exp. Fluids*, 36:43–52.

[55] Langari, M. and Yang, Z. (2013). Numerical study of the primary instability in a separated boundary layer transition under elevated free-stream turbulence. *Phys. Fluids*, 25:074106–1–074106–12.

[56] Lardeau, S., Leschziner, M., and Zaki, T. (2012). Large eddy simulation of transitional separated flow over a flat plate and a compressor blade. *Flow Turbul. and Combust.*, 88:919–944.

[57] Legrand, M., Nogueira, J., and Lecuona, A. (2011a). Flow temporal reconstruction from non-time-resolved data part I: mathematic fundamentals. *Exp. Fluids*, 51(4):1047–1055.

[58] Legrand, M., Nogueira, J., Tachibana, S., Lecuona, A., and Nauri, S. (2011b). Flow temporal reconstruction from non-time-resolved data part II: practical implementation, methodology validation, and applications. *Exp. Fluids*, 51(4):861–870.

[59] Lengani, D. and Simoni, D. (2015a). Recognition of coherent structures in the boundary layer of a low-pressure-turbine blade for different free-stream turbulence intensity levels. *International Journal of Heat and Fluid Flow*, 54:1–13.

[60] Lengani, D. and Simoni, D. (2015b). Recognition of coherent structures in the boundary layer of a low-pressure-turbine blade for different free-stream turbulence intensity levels. *International Journal of Heat and Fluid Flow*, 54:1–13.

[61] Lengani, D., Simoni, D., Ubaldi, M., and Zunino, P. (2014a). Pod analysis of the unsteady behavior of a laminar separation bubble. *Experimental Thermal and Fluid Science*, 58:70–79.

[62] Lengani, D., Simoni, D., Ubaldi, M., and Zunino, P. (2014b). POD analysis of the unsteady behavior of a laminar separation bubble. *Exp. Therm. Fluid Sci*, 58:70–79.

[63] Lengani, D., Simoni, D., Ubaldi, M., Zunino, P., and Bertini, F. (2011). Turbulent boundary layer separation control and loss evaluation of low profile vortex generators. *Experimental Thermal and Fluid Science*, 35(8):1505–1513.

[64] Lengani, D., Simoni, D., Ubaldi, M., Zunino, P., and Bertini, F. (2017a). Experimental investigation on the time–space evolution of a laminar separation bubble by proper orthogonal decomposition and dynamic mode decomposition. *Journal of Turbomachinery*, 139(3):031006.

[65] Lengani, D., Simoni, D., Ubaldi, M., Zunino, P., and Bertini, F. (2017b). Experimental study of free-stream turbulence induced transition in an adverse pressure gradient. *Experimental Thermal and Fluid Science*, 84:18–27.

[66] Lengani, D., Simoni, D., Ubaldi, M., Zunino, P., and Bertini, F. (2017c). Experimental study of free-stream turbulence induced transition in an adverse pressure gradient. *Experimental Thermal and Fluid Science*, 84:18–27.

[67] Liu, Z., Adrian, R. J., and Hanratty, T. J. (2001). Large-scale modes of turbulent channel flow: transport and structure. *J. Fluid Mech.*, 448:53–80.

[68] Luchini, P. (2000). Reynolds-number independent instability of the boundary layer over a flat surface. *J. Fluid Mech.*, 404:289–309.

[69] Lumley, J. L. (1970). Stochastic tools in turbulence. *Applied Mathematics and Mechanics, vol. 12*.

[70] Mahallati, A., McAuliffe, B. R., Sjolander, S. A., and Praisner, T. J. (2013). Aerodynamics of a low-pressure turbine airfoil at low reynolds numbers-part I: Steady flow measurements. *ASME J. of Turbomach.*, 135:011010–1–011010–9.

[71] Mandal, A. C., Venkatakrishnan, L., and Dey, J. (2010). A study on boundary-layer transition induced by free-stream turbulence. *J. Fluid Mech.*, 660:114–146.

[72] Mans, J., Kadijk, E. C., de Lange, H. C., and van Steenhoven, A. A. (2005). Breakdown in a boundary layer exposed to free-stream turbulencel. *Exp Fluids*, 39:1071–1083.

[73] Marxen, O. and Henningson, D. S. (2011). The effect of small-amplitude convective disturbances on the size and bursting of a laminar separation bubble. *J. Fluid Mech.*, 671:1–33.

[74] Marxen, O., Lang, M., and Rist, U. (2013). Vortex formation and vortex breakup in a laminar separation bubble. *Journal of Fluid Mechanics*, 728:58–90.

[75] Marxen, O., Lang, M., Rist, U., and Wagner, S. (2003). A combined experimental/numerical study of unsteady phenomena in a laminar separation bubble. *Flow Turbul. and Combust.*, 71:133–146.

[76] Marxen, O. and Rist, U. (2010). Mean flow deformation in a laminar separation bubble: separation and stability characteristics. *Journal of Fluid Mechanics*, 660:37–54.

[77] Marxen, O., Rist, U., and Wagner, S. (2004). Effect of spanwise-modulated disturbances on transition in a separated boundary layer. *AIAA journal*, 42(5):937–944.

[78] Matsubara, M. and Alfredsson, P. H. (2001). Disturbance growth in boundary layers subjected to free-stream turbulence. *J. Fluid Mech.*, 430:149–168.

[79] Maucher, U., Rist, U., and Wagner, S. (2000). Refined interaction method for direct numerical simulation of transition in separation bubbles. *AIAA journal*, 38(8):1385–1393.

[80] Mayle, R. E. (1991). The role of laminar-turbulent transition in gas turbine engines. *ASME J. of Turbomach.*, 113:509–537.

[81] Menter, F. R., Smirnov, P. E., Liu, T., and Avancha, R. (2015). A one-equation local correlation-based transition model. *Flow, Turbulence and Combustion*, 95(4):583–619.

[82] MichÃĄlek, J., Monaldi, M., and Arts, T. (2012). Aerodynamic performance of a very high lift low pressure turbine airfoil (t106c) at low reynolds and high mach number with effect of free stream turbulence intensity. *Journal of Turbomachinery*, 134(6):061009.

[83] Michael, L. (2015). *Statistical turbulence modelling for fluid dynamics-demystified: an introductory text for graduate engineering students*. World Scientific.

[84] Michelassi, V., Wissink, J. G., and Rodi, W. (2002). Analysis of DNS and LES of flow in a low-pressure turbine cascade with incoming wakes and comparison with experiments. *Flow Turbul. and Combust.*, 69:295–329.

[85] Morkovin, M. V. (1969). On the many faces of transition. In *Viscous drag reduction*, pages 1–31. Springer.

[86] Narasimha, R., Devasia, K., Gururani, G., and Narayanan, M. B. (1984). Transitional intermittency in boundary layers subjected to pressure gradient. *Experiments in Fluids*, 2(4):171–176.

[87] Nolan, K. and Zaki, T. (2013). Conditional sampling of transitional boundary layers in pressure gradients. *J. Fluid Mech.*, 728:306–339.

[88] Nolan, K. P. and Walsh, E. J. (2012). Particle image velocimetry measurements of a transitional boundary layer under free stream turbulence. *J. Fluid Mech.*, 702:215–238.

[89] Ol, M. V., McAuliffe, B. R., Hanff, E. S., Scholz, U., and Kähler, C. (2005). Comparison of laminar separation bubble measurements on a low reynolds number airfoil in three facilities. *AIAA paper*, 5149(1):2005.

[90] Pacciani, R., Marconcini, M., Fadai-Ghotbi, A., Lardeau, S., and Leschziner, M. A. (2011). Calculation of high-lift cascades in low pressure turbine conditions using a three-equation model. *Journal of Turbomachinery*, 133(3):031016.

[91] Pauley, L. L., Moin, P., and Reynolds, W. C. (1990). The structure of two-dimensional separation. *Journal of Fluid Mechanics*, 220:397–411.

[92] Perrin, R., Cid, E., Cazin, S., Sevrain, A., Braza, M., Moradei, F., and Harran, G. (2007). Phase-averaged measurements of the turbulence properties in the near wake of a circular cylinder at high reynolds number by 2C-PIV and 3C-PIV. *Exp Fluids*, 42:93–109.

[93] Prandtl, L. (1904). Verhandlungen des dritten internationalen mathematiker-kongresses. *Heidelberg, Leipeizig*, pages 484–491.

[94] Roach, P. E. and Brierley, D. H. (1991). The influence of a turbulent free-stream on zero-pressure gradient transitional boundary layer development. *Numerical simulation of unsteady flows and Transition to Turbulence*, CUP:319–347.

[95] Samson, A. and Sarkar, S. (2016). Effects of free-stream turbulence on transition of a separated boundary layer over the leading-edge of a constant thickness airfoil. *Journal of Fluids Engineering*, 138(2):021202.

[96] Sarkar, S. (2008). Identification of flow structures on a LP turbine blade due to periodic passing wakes. *J. Fluid Eng - T ASME*, 130:061103 (10 pages).

[97] Sarmast, S., Dadfar, R., Mikkelsen, R. F., Schlatter, P., Ivanell, S., Sørensen, J. N., , and Henningson, D. S. (2014). Mutual inductance instability of the tip vortices behind a wind turbine. *J. Fluid Mech.*, 755:705–731.

[98] Schlichting, H. and Gersten, K. (2000). *Boundary Layer Theory*. Springer,.

[99] Schmid, P. J. and Henningson, D. S. (2001). *Stability and Transition in Shear Flows*. Springer, New York.

[100] Schreiber, H.-A., Steinert, W., and Küsters, B. (2000). Effects of reynolds number and free-stream turbulence on boundary layer transition in a compressor cascade. In *ASME Turbo Expo 2000: Power for Land, Sea, and Air*, pages V003T01A068–V003T01A068. American Society of Mechanical Engineers.

[101] Schubauer, G. (1947). Laminar boundary-layer oscillations and stability of laminar flow. *Journal of the Aeronautical Sciences*, 14(2):69–78.

[102] Sciacchitano, A., Neal, D. R., Smith, B. L., Warner, S. O., Vlachos, P. P., Wieneke, B., and Scarano, F. (2015). Collaborative framework for piv uncertainty quantification: comparative assessment of methods. *Measurement Science and Technology*, 26(7):074004.

[103] Simoni, D., Lengani, D., and Guida, R. (2016a). A wavelet-based intermittency detection technique from piv investigations in transitional boundary layers. *Experiments in Fluids*, 57(9):145.

[104] Simoni, D., Lengani, D., Ubaldi, M., Zunino, P., and Dellacasagrande, M. (2017). Inspection of the dynamic properties of laminar separation bubbles: free-stream turbulence intensity effects for different reynolds numbers. *Experiments in Fluids*, 58(6):66.

[105] Simoni, D., Ubaldi, M., and Zunino, P. (2012a). Loss production mechanisms in a laminar separation bubble. *Flow Turbul. and Combust.*, 89(4):547–562.

[106] Simoni, D., Ubaldi, M., and Zunino, P. (2014). Experimental investigation of flow instabilities in a laminar separation bubble. *Journal of Thermal Science*, 23(3):203–214.

[107] Simoni, D., Ubaldi, M., and Zunino, P. (2016b). A simplified model predicting the Kelvin-Helmholtz instability frequency for laminar separated flows. *Journal of Turbomachinery*, 138(4):044501.

[108] Simoni, D., Ubaldi, M., Zunino, P., and Ampellio, E. (2016c). Free-stream turbulence effects on the boundary layer of a high-lift low-pressure-turbine blade. *Journal of Thermal Science*, 25(3):195–206.

[109] Simoni, D., Ubaldi, M., Zunino, P., Lengani, D., and Bertini, F. (2012b). An experimental investigation of the separated-flow transition under high-lift turbine blade pressure gradients. *Flow Turbul. and Combust.*, 88:45–62.

[110] Sirovich, L. (1987). Turbulence and the dynamics of coherent structures. part I-III. *Q Appl Math*, 45:561–590.

[111] Smith, A. and Gamberoni, N. (1956). Transition, pressure gradient, and stability theory. report no. es. 26388, douglas aircraft co. *Inc., El Segundo, CA*.

[112] Spalart, P. and Strelets, M. (2000). Mechanisms of transition and heat transfer in a separation bubble. *J. Fluid Mech.*, 403:329–349.

[113] Suzen, Y., Huang, P., Ashpis, D., Volino, R., Corke, T., Thomas, F., Huang, J., Lake, J., and King, P. (2007). A computational fluid dynamics study of transitional flows in low-pressure turbines under a wide range of operating conditions. *Journal of turbomachinery*, 129(3):527–541.

[114] Suzen, Y. B., Huang, P., Hultgren, L. S., and Ashpis, D. E. (2003). Predictions of separated and transitional boundary layers under low-pressure turbine airfoil conditions using an intermittency transport equation. *Journal of Turbomachinery*, 125(3):455–464.

[115] Talan, M. and Hourmouziadis, J. (2002). Characteristic regimes of transitional separation bubbles in unsteady flow. *Flow, turbulence and combustion*, 69(3-4):207–227.

[116] Tardu, S. (1995). Characteristics of single and clusters of bursting events in the inner layer. *Experiments in fluids*, 20(2):112–124.

[117] Thwaites, B. (1949). Approximate calculation of the laminar boundary layer. *The Aeronautical Quarterly*, 1(3):245–280.

[118] Ukeiley, L., Glauser, M., and Wick, D. (1993). Downstream evolution of proper orthogonal decomposition eigenfunctions in a lobed mixer. *AIAA journal*, 31(8):1392–1397.

[119] Van Ingen, J. (1956). A suggested semi-empirical method for the calculation of the boundary layer transition region.

[120] Volino, R. J. (2002a). Separated flow transition under simulated low-pressure turbine airfoil conditions: Part 1—mean flow and turbulence statistics. In *ASME Turbo Expo 2002: Power for Land, Sea, and Air*, pages 691–702. American Society of Mechanical Engineers.

[121] Volino, R. J. (2002b). Separated flow transition under simulated low-pressure turbine airfoil conditions: Part 2—turbulence spectra. In *ASME Turbo Expo 2002: Power for Land, Sea, and Air*, pages 703–712. American Society of Mechanical Engineers.

[122] Von Karman, T. and Biot, M. A. (1940). *Mathematical methods in engineering*. McGraw Hill.

[123] Watmuff, J. H. (1999). Evolution of a wave packet into vortex loops in a laminar separation bubble. *J. Fluid Mech.*, 397:119–169.

[124] Wee, D., Yi, T., Annaswamy, A., and Ghoniem, A. F. (2004). Self-sustained oscillations and vortex shedding in backward-facing step flows: Simulation and linear instability analysis. *Phys. Fluids*, 16:3361–3373.

[125] Wen, X., Tang, H., and Duan, F. (2016). Interaction of in-line twin synthetic jets with a separated flow. *Physics of Fluids (1994-present)*, 28(4):043602.

[126] Westin, K. J. A., Boiko, A. V., Klingmann, B. G. B., Kozlov, V. V., and Alfredsson, P. H. (1994). Experiments in a boundary layer subjected to free stream turbulence. part 1. boundary layer structure and receptivity. *J. Fluid Mech.*, 281:193–218.

[127] Wieneke, B. (2015). PIV uncertainty quantification from correlation statistics. *Measurement Science and Technology*, 26(7):074002.

[128] Yang, Z. and Voke, P. R. (2001). Large-eddy simulation of boundary-layer separation and transition at a change of surface curvature. *J. Fluid Mech.*, 439:305–333.

[129] Yaras, M. (2002). Measurements of the effects of freestream turbulence on separation-bubble transition. In *ASME Turbo Expo 2002: Power for Land, Sea, and Air*, pages 647–660. American Society of Mechanical Engineers.

[130] Yarusevych, S., Kawall, J. G., and Sullivan, P. E. (2008). Separated-shear-layer development on an airfoil at low reynolds numbers. *AIAA journal*, 46(12):3060–3069.

[131] Yarusevych, S. and Kotsonis, M. (2016). Effect of local dbd plasma actuation on transition in a laminar separation bubble. *Flow, Turbulence and Combustion*, pages 1–22.

[132] Zaki, T. (2013). From streaks to spots and on to turbulence: Exploring the dynamics of boundary layer transition. *Flow Turbul. and Combust.*, 91:451–473.

[133] Zaki, T. A. and Durbin, P. A. (2006). Continuous mode transition and the effects of pressure gradient. *J. Fluid Mech.*, 563:357–388.

[134] Zaki, T. A. and Saha, S. (2009). On shear sheltering and the structure of vortical modes in single-and two-fluid boundary layers. *Journal of Fluid Mechanics*, 626:111–147.